

**STRUCTURAL AND ELECTRICAL STUDY OF
GLYCOLIPID THIN FILMS PREPARED BY SPIN-COATING
TECHNIQUE**

NG BOON KI

**FACULTY OF SCIENCE
UNIVERSITY OF MALAYA
KUALA LUMPUR**

2014

UNIVERSITI MALAYA

ORIGINAL LITERARY WORK DECLARATION

Name of Candidate: **Ng Boon Ki**

(I.C/Passport No: **850926-05-5429**)

Registration/Matric No: **SGR100033**

Name of Degree: **Master of Science (Dissertation)**

Title of Dissertation ("this Work"):

**STRUCTURAL AND ELECTRICAL STUDY OF GLYCOLIPID THIN FILMS
PREPARED BY SPIN-COATING TECHNIQUE**

Field of Study: Advanced materials

I do solemnly and sincerely declare that:

- (1) I am the sole author/writer of this Work;
- (2) This Work is original;
- (3) Any use of any work in which copyright exists was done by way of fair dealing and for permitted purposes and any excerpt or extract from, or reference to or reproduction of any copyright work has been disclosed expressly and sufficiently and the title of the Work and its authorship have been acknowledged in this Work;
- (4) I do not have any actual knowledge nor do I ought reasonably to know that the making of this work constitutes an infringement of any copyright work;
- (5) I hereby assign all and every rights in the copyright to this Work to the University of Malaya ("UM"), who henceforth shall be owner of the copyright in this Work and that any reproduction or use in any form or by any means whatsoever is prohibited without the written consent of UM having been first had and obtained;
- (6) I am fully aware that if in the course of making this Work I have infringed any copyright whether intentionally or otherwise, I may be subject to legal action or any other action as may be determined by UM.

Date: **13 March 2014**

Candidate's Signature

Subscribed and solemnly declared before,

Date: **13 March 2014**

Witness's Signature

Name: **Prof. Dr. Wan Haliza Abd Majid**

Designation: **Professor**

Name: **Dr. Vengadesh Periasamy**

Designation: **Senior Lecturer**

ABSTRACT

This research study is focused on the effect of the branched alkyl chain length to the structural and electrical properties of maltoside glycolipids. A theoretical model had been applied to the system to determine the bilayer molecular length of molecules from the hopping mechanism in the diffusion process.

The initial research is related to the device fabrication of glycolipids. The glycolipids thin films were prepared by spin-coating technique on aluminium deposited glass substrate. The aluminium electrode was deposited by thermal evaporation method as the top electrode. Therefore, the metal-insulator-metal (MIM) devices had been fabricated.

The subsequent research is on the study of the structural properties of glycolipids by experimental technique including optical polarizer microscopy, differential scanning calorimetry, thermogravimetry, Fourier transforms infrared spectroscopy, and x-ray diffraction. The optical polarizer microscopy and differential scanning calorimetry were used to identify the phase transition and the texture of the liquid crystalline. The thermogravimetry measurements were carried out to study the thermal stability of the glycolipid compounds. Subsequently, the Fourier transforms infrared spectroscopy was used to determine the functional groups which were present in the compounds at a specific wavenumber. Finally, the x-ray diffraction was used to infer the structural arrangement of the compounds based on the prominent peak which was observed in the x-ray diffraction pattern.

The study on the electrical properties of glycolipids which were described in dielectric, conductivity and pyroelectric is also conducted. The dielectric and conductivity properties of glycolipid compounds have been studied in a broad frequency range ($10^{-2} - 10^6$ Hz) with varying temperature during heating and cooling processes. The spectra of the complex dielectric and conductivity for the glycolipid compounds have been fitted using empirical functions to analyze the polarization behaviour and the activation energy which were used to depict the phase transition behaviour. In addition, the dielectric constant at 100 Hz of glycolipid compounds has been extracted to study the phase transition behaviour. The pyroelectric effect of glycolipid compounds were investigated in several temperature ranges. The different length of branched alkyl chain influences the net dipole moment which contributes to the pyroelectric coefficient. In addition, the arrangement of molecules affects the dielectric loss and the figure-of-merit of the glycolipids thin films.

Investigation on the diffusion process of glycolipid compounds was carried out at the final stage of this research. The charge carriers were diffused randomly around the polar sugar head group and were modeled by random walk scheme. From this model, the hydrogen bond lengths and bilayer molecular thickness of Malto-C12C8 were calculated as 2.45 Å and 3.61 nm respectively. Whereas, the hydrogen bond lengths and bilayer molecular thickness of Malto-C14C10 were calculated as 2.66 Å and 4.02 nm respectively.

ABSTRAK

Kajian ini bertumpu kepada kesan panjang rantai alkil bercabang kepada sifat-sifat struktur dan elektrik glikolipid maltoside. Tambahan pula, model teori telah digunakan ke atas sistem tersebut untuk menentukan panjang molekul dua lapisan daripada mekanisme melompat dalam proses penyebaran.

Kajian awal penyelidikan ini berkaitan fabrikasi peranti glikolipid. Filem-filem nipis glikolipid telah disediakan melalui teknik putaran-salutan pada substrat kaca yang berenapkan aluminium. Elektrod aluminium atas telah diendap dengan kaedah penyekatan haba menghasilkan fabrikasi peranti logam-penebat-logam (MIM).

Kajian seterusnya adalah mengenai sifat-sifat struktur glikolipid dengan menggunakan teknik eksperimen termasuk mikroskopi optik polarizer, pengimbasan kebezaan kalorimeter, termogravimetri, spektroskopi inframerah transforms Fourier, dan belauan sinar-x. Mikroskopi optik polarizer dan pengimbasan kebezaan kalorimeter digunakan untuk mengenal pasti fasa peralihan dan tekstur kristal cecair. Ukuran termogravimetri telah dijalankan untuk mengkaji kestabilan haba sebatian glikolipid. Selepas itu, spektroskopi inframerah transforms Fourier telah digunakan untuk menentukan kumpulan berfungsi yang hadir dalam sebatian dengan nombor gelombang tertentu. Akhirnya, belauan sinar-x telah digunakan untuk membuat kesimpulan susunan struktur asas sebatian melalui puncak tertinggi yang diperhatikan dalam corak pembelauan sinar-x.

Kajian sifat-sifat elektrik glikolipid dijelaskan melalui eksperimen dielektrik, konduktiviti dan piroelektrik. Dielektrik dan konduktiviti sifat sebatian glikolipid telah dikaji dalam julat frekuensi yang luas (10^{-2} - 10^6 Hz) dengan suhu yang berbeza semasa proses pemanasan dan penyejukan. Spektrum dielektrik yang kompleks dan kekonduksian untuk sebatian glikolipid telah dimuatkan melalui penggunaan fungsi empirikal untuk menganalisis tingkah laku polarisasi dan tenaga pengaktifan yang digunakan untuk menggambarkan tingkah laku fasa peralihan. Di samping itu, pemalar dielektrik pada 100 Hz daripada sebatian glikolipid telah dicatat untuk mengkaji tingkah laku fasa peralihan. Kesan piroelektrik daripada sebatian glikolipid telah disiasat dalam beberapa julat suhu. Panjang rantaian alkil bercabang yang berbeza akan mempengaruhi kutub bersih yang akan menyumbang kepada pekali piroelektrik. Di samping itu, susunan molekul akan memberi kesan kepada kehilangan dielektrik dan angka merit filem nipis glikolipid tersebut.

Kajian mengenai proses penyebaran sebatian glikolipid dibuat pada tahap akhir penyelidikan ini. Pembawa cas meresap secara rawak di seluruh kutub kumpulan kepala gula dan telah dimodel mengikut skema perjalanan secara rawak. Dari model ini, panjang ikatan hidrogen dan ketebalan molekul dua lapisan Malto-C12C8 telah dikira masing-masing, sebagai 2.45 Å dan 3.61 nm. Manakala, panjang ikatan hidrogen dan ketebalan molekul dua lapisan Malto-C14C10 telah dikira masing-masing, sebagai 2.66 Å dan 4.02 nm.

ACKNOWLEDGEMENTS

I like to express my sincere appreciation to my supervisor, Prof. Dr. Wan Haliza Abd Majid for her kind supervision and guidance throughout the entire progress of the study. My great thankfulness goes to my other supervisor, Dr. Vengadesh Periasamy, I gratefully appreciate for his patient and tolerance throughout the entire work. Without their guidance and valuable advice, the work would not be accomplished successfully.

I also would like to express my sincere gratefulness to my senior, Mr. Gan Wee Chen and Dr. Thamil Selvi Velayutham. The guidance provided by them in experimental and theoretical aspect is really appreciated.

Besides that, I would like to express my honest appreciation to our collaborators; Prof. Takeo Furukawa, his professional advice and assistance on the Low Frequency Dielectric Measurement system were helpful and important to the work; Prof. Rauzah Hashim, her professional advice and support on the glycolipids compounds were crucial for this work. Subsequently, my special thanks to Mr. Mohamad Aruf, Mr. Ismail Bin Jaafar and Mrs. Noor Idayu Mat Zahid, for their help and assistance in instruments such as XRD, FTIR, OPM, DSC and thermogravimetry.

I would like to acknowledge University of Malaya for offering the University of Malaya Fellowship Scheme to pursue my master degree. In addition, I would also like to acknowledge the financial support from Postgraduate Research Fund (PPP) of PS344/2010B and University Malaya Research Grant (UMRG) of RG079/09AFR.

Furthermore, I would like to express million thanks to the entire Low Dimensional Materials Research Centre (LDMRC) members especially Prof. Datin Dr. Saadah Abdul Raman and Mdm. Norlela Mohamed Shahardin for their support and advices. Many thank and gratitude to other LDMRC member especially Dr. Goh Boon Tong, Ms. Toong Way Yun, Mr. Lim Lih Wei, Mr. Mohd. Arif Mohd. Sarjidan, Ms. Nor Khairiah Za'aba, Mr. Chan Kee Wah, Mr. Tan Kah Sin, Mr. Chua Chong Lim and Mr. Yeoh Keat Hoe for their assistance, understanding and literature sharing during the course of this work. Same expression goes to my dear friends, Mr. Chew Wei Xiang and Mr. Lim Lian Kuang for their support and suggestions.

Last but not least, I wish to show my deep appreciation to my family as well as my girlfriend for their concerns, support and understanding that enabled me to carry on with my work. This work would not have been possible without their love and support.

List of Publications

1. Ng, B. K., Velayutham, T. S., Gan, W. C., Majid, W. H. A., Periasamy, V., Hashim, R., Zahid, N. I. M. (2013). Pyroelectricity in Synthetic Amphitropic Glycolipid for Potential Application of IR Sensor Device, *Ferroelectrics*, **445**(1), 67-73.
2. Velayutham, T. S., Majid, W. H. A., Ng, B. K., Gan, S. N. (2012). Effect of oleic acid content and chemical crosslinking on the properties of palm oil-based polyurethane coatings, *Journal of Applied Polymer Science*, **129**(1), 415-421.

Table of Contents

Original Literary Work Declaration	ii
Abstract	iii
Abstrak	iv
Acknowledgements	v
List of Publications	vi
Table of Contents	vii
List of Figures	x
List of Tables	xiii

Chapter 1

Introduction

1.0 Introduction	1
References	4

Chapter 2

Literature review

2.0 Introduction	5
2.1 Liquid crystals	7
2.1.1 States of matter	7
2.1.2 Liquid crystal nomenclature	8
2.1.3 Types of Liquid crystals	11
2.2 Glycolipid liquid crystals	14
2.2.1 Natural glycolipids	15
2.2.2 Synthetic glycolipids	16
2.3 Dielectric properties and conductivity	16
2.3.1 Dielectric	16
2.3.2 Conductivity	23
2.4 Pyroelectric effect	27
2.5 Diffusion process	30
2.5.1 Basic model of diffusion	31

2.6 Summary	34
References	36

Chapter 3

Experimental details

3.0 Introduction	40
3.1 Device fabrication	41
3.1.1 Substrate preparation	41
3.1.2 Substrate cleaning process	42
3.1.3 Electrode deposition	43
3.1.4 Thin films preparation	45
3.2 Structural properties of glycolipid	46
3.2.1 Optical Polarizer Microscopy (OPM)	46
3.2.2 Differential Scanning Calorimetry (DSC)	48
3.2.3 Thermogravimetry (TGA)	51
3.2.4 Fourier Transforms Infrared (FTIR) Spectroscopy	53
3.2.5 Profilometer	54
3.2.6 X-ray Diffraction (XRD)	56
3.3 Electrical properties of glycolipid	58
3.3.1 Dielectric constants and relaxation measurements	58
3.3.2 Conductivity measurements	60
3.3.3 Pyroelectric measurements	61
3.4 Summary	62
References	63

Chapter 4

Structural characterization of glycolipid thin films

4.0 Introduction	64
4.1 Optical Polarizer Microscopy (OPM)	65
4.2 Differential Scanning Calorimetry (DSC)	71
4.3 Thermogravimetry (TGA)	73
4.4 Fourier Transforms Infrared (FTIR) Spectroscopy	76
4.5 X-ray Diffraction (XRD)	77

4.6 Summary	79
References	81

Chapter 5

Electrical properties of glycolipid thin films

5.0 Introduction	82
5.1 Dielectric dispersion curves	83
5.1.1 Complex dielectric	83
5.1.2 Dielectric constant at 100 Hz	87
5.1.3 Complex dielectric fitting with an empirical function	88
5.2 Conductivity	90
5.2.1 Complex conductivity	90
5.2.2 Complex conductivity fitting with an empirical function	94
5.2.3 Activation energy	95
5.3 Pyroelectric effect	97
5.4 Diffusion process	102
5.4.1 Conductive strength, relaxation frequency, and dielectric strength	102
5.4.2 Diffusion coefficient	105
5.5 Summary	109
References	110

Chapter 6

Conclusions and suggestions for future works

6.0 Conclusions	111
6.0.1 Structural properties of maltoside glycolipids	111
6.0.2 Electrical properties of maltoside glycolipids	112
6.1 Future works	113

List of Figures

Figure	Caption	Page
Figure 2.1	Illustration of the reversible thermodynamic interaction among the thermal, mechanical and electrical properties.	29
Figure 3.1	Edward model A-360 vacuum system with Thermal evaporator.	43
Figure 3.2	Laurell WS-650MZ-23NPP spin coater.	45
Figure 3.3	Optical Polarizer Microscopy.	47
Figure 3.4	Differential Scanning Calorimetry.	48
Figure 3.5	Two specific positions in the sample chamber. S and R represent as sample and reference position respectively.	50
Figure 3.6	DSC plot of liquid crystal.	50
Figure 3.7	Thermogravimetry.	52
Figure 3.8	Fourier Transforms Infrared Spectroscopy.	53
Figure 3.9	KLA Tencor P-6 Surface Profilometer.	56
Figure 3.10	X-ray Diffraction.	57
Figure 3.11	Laboratory-made dielectric spectrometer.	58
Figure 3.12	Agilent with model 4294A Impedance Analyzer.	59
Figure 3.13	Experimental setup for pyroelectric measurement.	61
Figure 4.1	DSC curves of Malto-C8C4, Malto-C12C8 and Malto-C14C10 at 10 °C min ⁻¹ heating rate.	72
Figure 4.2	Weight % and derivative weight % curves versus temperature of Malto-C8C4.	74
Figure 4.3	Weight % and derivative weight % curves versus temperature of Malto-C12C8.	75
Figure 4.4	Weight % and derivative weight % curves versus temperature of Malto-C14C10.	75
Figure 4.5	FTIR spectra of glycolipid Malto-C8C4, Malto-C12C8 and Malto-C14C10.	77

Figure 4.6	XRD profiles of glycolipid Malto-C8C4, Malto-C12C8 and Malto-C14C10 at room temperature.	79
Figure 5.1	Dielectric constant ϵ' and dielectric loss ϵ'' spectra of Malto-C8C4 at heating-mode (a) & (b) and cooling-mode (c) & (d) from 30 °C – 150 °C with 10 °C temperature step.	84
Figure 5.2	Dielectric constant ϵ' and dielectric loss ϵ'' spectra of Malto-C12C8 at heating-mode (a) & (b) and cooling-mode (c) & (d) from 30 °C – 160 °C with 10 °C temperature step.	85
Figure 5.3	Dielectric constant ϵ' and dielectric loss ϵ'' spectra of Malto-C14C10 at heating-mode (a) & (b) and cooling mode (c) & (d) from 30 °C – 190 °C with 10 °C temperature step.	86
Figure 5.4	Temperature dependent of dielectric constant ϵ' of Malto-C8C4, Malto-C12C8, and Malto-C14C10 in heating-mode (a) and cooling-mode (b) at 100 Hz.	87
Figure 5.5	Observed and fitted of dielectric constant ϵ' and dielectric loss ϵ'' spectra of Malto-C12C8 at 100 °C during heating process.	90
Figure 5.6	Real conductivity σ' and imaginary conductivity σ'' spectra of Malto-C8C4 at heating-mode (a) & (b) and cooling-mode (c) & (d) from 30 °C – 150 °C with 10 °C temperature step.	91
Figure 5.7	Real conductivity σ' and imaginary conductivity σ'' spectra of Malto-C12C8 at heating-mode (a) & (b) and cooling-mode (c) & (d) from 30 °C – 160 °C with 10 °C temperature step.	92
Figure 5.8	Real conductivity σ' and imaginary conductivity σ'' spectra of Malto-C14C10 at heating-mode (a) & (b) and cooling-mode (c) & (d) from 30 °C – 190 °C with 10 °C temperature step.	93
Figure 5.9	Observed and fitted of real conductivity σ' and imaginary conductivity σ'' spectra of Malto-C12C8 at 100 °C during heating process.	95
Figure 5.10	The Arrhenius plot shows the corresponding activation energy of Malto-C8C4, Malto-C12C8, and Malto-C14C10 in heating- (a, b & c) and cooling-mode (d, e & f).	96
Figure 5.11	Pyroelectric current waveform at the rate of 0.03 °C s ⁻¹ with respect to temperature variation of (a) 25-26 °C and (b) 50-51 °C for Malto-C12C8.	98

Figure 5.12	(a) Pyroelectric coefficient and (b) figure-of-merit of three glycolipid compounds at various temperatures.	99
Figure 5.13	Proposed molecular arrangements of (a) Malto-C8C4, (b) Malto-C12C8, and (c) Malto-C14C10 in the formation of thin film between top and bottom electrode.	100
Figure 5.14	The cubic phase properties (conductive strength $\Delta\sigma_{dc}$, relaxation frequency f_m , and dielectric strength $\Delta\epsilon$) of Malto-C12C8 and Malto-C14C10 in interfacial-mode and dielectric-mode during heating (a, b & c) and cooling process (d, e & f).	104
Figure 5.15	The double logarithmic plot of diffusion coefficients D of Malto-C12C8 and Malto-C14C10 as a function of relaxation frequency in interfacial-mode and dielectric-mode during heating (a) and cooling process (b).	106
Figure 5.16	Schematic diagram of charge hopping process with their hopping length for glycolipids in (a) Malto-C12C8 and (b) Malto-C14C10 for both interfacial and dielectric modes in heating process (circle represent domain which contain disaccharide polar head group only).	108

List of Tables

Table	Caption	Page
Table 2.1	The phase transitions and their symbols.	11
Table 2.2	The phase sequence transform from low to high concentration.	13
Table 4.1	Optical texture of Malto-C8C4 observed with a polarizing microscope at 10 °C min ⁻¹ heating rate.	65
Table 4.2	Optical texture of Malto-C12C8 observed with a polarizing microscope at 10 °C min ⁻¹ heating rate.	67
Table 4.3	Optical texture of Malto-C14C10 observed with a polarizing microscope at 10 °C min ⁻¹ heating rate.	69
Table 4.4	The molecular structures of the maltosides and their phase transitions based on OPM measurement at 10 °C min ⁻¹ heating rate.	70
Table 4.5	The molecular structures of the maltosides and their phase transitions based on DSC measurement at 10 °C min ⁻¹ heating rate.	73
Table 4.6	The vibrational modes and wavenumber of glycolipids Malto-C8C4, Malto-C12C8 and Malto-C14C10.	76
Table 4.7	The 2θ and d spacing of glycolipids Malto-C8C4 according to the prominent peaks of the XRD pattern.	78
Table 5.1	Summary of the pyroelectric coefficient, p (with unit $\mu\text{C m}^{-2} \text{K}^{-1}$) for the glycolipid compounds.	99
Table 5.2	Summary of the figure-of-merit (with unit $\mu\text{C m}^{-2} \text{K}^{-1}$) for the glycolipid compounds.	100
Table 5.3	Summary of the dielectric loss, ε'' at 100 Hz for the glycolipid compounds.	100
Table 5.4	Hopping length of the <u>interfacial polarization</u> calculated from the theoretical model (dielectric measurement) for Malto-C12C8 and Malto-C14C10 in the heating and cooling process.	107
Table 5.5	Hopping length of the <u>dielectric polarization</u> calculated from the theoretical model (dielectric measurement) for Malto-C12C8 and Malto-C14C10 in the heating and cooling process.	109

CHAPTER 1: INTRODUCTION

1.0 Introduction

Glycolipid compounds are one kind of carbohydrate liquid crystal which is extraordinary liquid crystals because they have some different properties when compared to the usual liquid crystals such as monophilic liquid crystals. Many variety of carbohydrate mesogen compounds had been synthesized (Vill, 1989). Some of the interesting application had been reported by researchers (Jeffrey et al., 1992; Prade et al., 1995; Blunk, 1998). The glycolipids are also known as amphiphilic liquid crystals which comprising of hydrophilic (contain monosaccharide or disaccharide sugar head) and hydrophobic (single or branched hydrocarbon chain) parts. The mesophase of glycolipids have two behaviors known as liquid crystals phase and isotropic phase. The molecules in liquid crystals phase are packed in an ordered arrangement and provide the shape-driven mesophase transition, whereas the molecules in isotropic phase are arranged in a random way. In addition, the first reported glycolipid compounds which exhibited double melting points was Hexadecyl- β -D-glucopyranoside (Fischer et al., 1911; Hori, 1958). This compound consists of two molecular parts which are known as sugar residue (hydrophilic and polar) and paraffin chain (lipophilic and apolar). Moreover, they experience microscopic separation between hydrophilic and lipophilic layers. These formations of layer structure have the same geometry as the monophilic liquid crystals, i.e. Smectic A. Thus, the mesophase of glycolipids have similar physical properties but different chemical properties when compared to monophilic liquid crystals. Additionally, these carbohydrate liquid crystals have some remarkable behaviors and properties which are affected by the variety of functional sugar head groups (Hinz et al., 1985; Engels et al.,

1998; Nilsson et al., 1996). These are low melting points, non-toxicity, solubility in water and organic solvents, chirality, degradability, and accessibility. Besides, glycolipids can show the mesophases in melted state (thermotropic behavior) and in solution form (lyotropic behavior). Thus, researchers have used the term amphotropic liquid crystals to note the compounds which exhibited both behaviors (Baron, 2001).

In addition, it was discovered that the glycolipid layers have electrically polarized behaviour (Abeygunaratne et. al., 2004) in the mixed structures of glycolipid dodecyl- β -D-glucopyranoside and bent-core liquid crystals. It was due to the dodecyl- β -D-glucopyranoside molecules which had formed macroscopically nonpolar structures and exhibiting the tilted configuration (polar heads tilted with respect to each other) in the bent-core environment. Subsequently, the pyroelectricity in living cells had also been observed (Lang, 1966). Ferroelectricity in cell membrane was reported since the cell surface recognition was involved in some electrical behavior (Athenstaedt, 1986). This work is aimed to present a study on the effect of the branched alkyl chain length of the maltoside glycolipids in term of structural, dielectric and pyroelectric properties. Furthermore, a theoretical model was applied to the system to determine the bilayer molecular length of molecules from the hopping mechanism in the diffusion process.

Chapter 2 of this thesis describes the literature review of liquid crystals. The glycolipid liquid crystal which exhibits amphiphilic behavior has been described. Subsequently, the electrical properties of glycolipid such as dielectric, conductivity, and pyroelectricity will be discussed. This chapter also discusses the diffusion process of charge carriers in glycolipid.

Chapter 3 deals with the device fabrication and experimental set-up used to investigate the structural and electrical properties of glycolipids. The device fabrication includes the substrate preparation and cleaning process which are elaborated in this chapter. Then, the experimental technique used to study the structural properties of glycolipids were described in details, including Optical Polarizer Microscopy (OPM), Differential Scanning Calorimetry (DSC), Thermogravimetry (TGA), Fourier Transforms Infrared Spectroscopy (FTIR), and X-ray Diffraction (XRD). The electrical properties of glycolipids were discussed in the section relating to dielectric, conductivity, and pyroelectricity.

The next chapter, Chapter 4 describes the results and discussion in the structural properties of the glycolipids Malto-C8C4, Malto-C12C8 and Malto-C14C10. The structural studies include the OPM, DSC, TGA, FTIR and XRD.

Results and discussions on electrical properties of the glycolipids Malto-C8C4, Malto-C12C8 and Malto-C14C10 were addressed in Chapter 5. The spectra of the complex dielectric and conductivity are reproduced using the empirical function to determine several quantitative parameters. The pyroelectric effect of glycolipid compounds has been investigated in terms of branched alkyl chain length. Subsequently, the diffusion process in glycolipids was also explained in this chapter.

Finally, Chapter 6 concludes with a summary of the research findings. In addition, this chapter also includes possible future works on glycolipid liquid crystals.

References

- Abeygunaratne, S., Jakli, A., Milkereit, G., Sawade, H., Vill, V. (2004). Antiferroelectric ordering of amphiphilic glycolipids in bent-core liquid crystals. *Physical Review E*, **69**, 021703.
- Athenstaedt, H. (1986). Human tissues and systems as pyroelectric detectors and transducers, Proceeding of the Sixth IEEE International Symposium on Applications of Ferroelectrics, Bethlehem, U.S.A., June 8–11, 1986, pp. 532–537.
- Barón, M. (2001). Definitions of basic terms relating to low-molar-mass and polymer liquid crystals (IUPAC Recommendations 2001). *Pure and Applied Chemistry*, **73**, 845–855
- Blunk, D., Praefcke, P., Vill, V. (1998). Handbook of Liquid Crystals; 3, Chapter 6: 305–340.
- Engels, T., von Rybinski, W. J. (1998). Liquid crystalline surfactant phases in chemical applications, *Journal of Materials Chemistry*, **8**, 1313–1320.
- Fischer, E., Helferich, B. (1911). Über neue synthetische glycoside, *Liebigs Annalen der Chemie*, **383**, 68–91.
- Hinz, H. J., Six, L., Ruess, K. P., Lieflander, M. (1985). Head-group contributions to bilayer stability: monolayer and calorimetric studies on synthetic, stereochemically uniform glucolipids. *Biochemistry* **24**, 806–813.
- Hori, R. (1958). Alkyl derivatives of carbohydrates. II. Synthesis of alkyl-b-cellobiosides, *Yakugaku*, **78**, 999–1002.
- Jeffrey, G. A., Wingert, L. M. (1992). Carbohydrate liquid crystal, *Liquid Crystals*, **12**, 179–202.
- Lang, S. B. (1966). Pyroelectric effect in bone and tendon, *Nature*, **212**, 704–715.
- Nilsson, F., Soderman, I., Johansson, I., (1996). Physical–chemical properties of the n-octyl b-D-glucoside/water system. A phase diagram, self diffusion NMR and SAXS study, *Langmuir*, **12**, 902–908.
- Prade, H., Miethchen, R., Vill, V. (1995). Thermotropic liquid crystals based on amphiphilic carbohydrates, *Journal für Praktische Chemie*, **337**, 427–440.
- Vill, V., Böcker, T., Thiem, J., Fischer, F. (1989). Studies on liquid crystalline glycosides, *Liquid Crystals*, **6**(3), 349–356.

CHAPTER 2: LITERATURE REVIEW

2.0 Introduction

This chapter describes the literature review of liquid crystals. One of the liquid crystals which exhibits amphiphilic behavior, named glycolipid liquid crystal has also been under reviewed. Subsequently, the electrical properties of glycolipid such as dielectric activity, conductivity and pyroelectricity will be discussed in Sections 2.3 and 2.4. This chapter will also discuss the diffusion process of charge carriers in glycolipid.

The liquid crystal section (Section 2.1) consists of the states of matter, nomenclature of liquid crystals and types of liquid crystals. This section describes the history of liquid crystal and some basic structures of liquid crystals. The nomenclatures of liquid crystals have been discussed according to their phases. In addition, the type of liquid crystals that portray thermotropic and lyotropic behaviors were also described.

The glycolipid liquid crystals are a special class of liquid crystals. It is because glycolipids exhibit different principles compared to the usual liquid crystals. Most glycolipid materials have low melting points, non-toxic and degradable. They can be found in nature, such as in cell boundaries and membranes. Furthermore, they can be synthesized in such a way that the hydrophilic part can be connected to the hydrophobic part of the material.

Section 2.3 is related to the electrical properties, i.e. dielectric activity and conductivity of glycolipids. Dielectric spectroscopy is used to study the dielectric

behaviour of insulator materials as a function of frequency. Several polarizations will be observed from low to high frequency sequence such as electrode, interfacial, orientation, atomic and electronic. Dielectric spectroscopy can be described by several models such as Debye function, Cole and Davidson function, or Havriliak and Negami function. The electrical conductivity of glycolipids is determined by the direct current (dc) conductivity. Electrical conduction in materials may be due to the movement of electron or ions. Several models to describe the dc conduction mechanism have been discussed. The activation energy of Arrhenius relation is obtained by the dc conductivity.

The following section (Section 2.4) is related to the pyroelectricity of materials. Materials which have spontaneous polarization and generate current when there is a temperature changes is known as pyroelectricity. This pyroelectric behavior can exist in ceramics, polymers or bio-materials. The section also discusses the relation between the mechanical, thermal and electrical properties, which contribute to pyroelectricity.

The final section (Section 2.5) of this chapter describes the diffusion process as a transport method in the materials. Diffusion process can be described by Fick's law or random walk scheme. Several basic models of diffusion were introduced, such as Fick's law, Einstein-Smoluchowski relation and diffusion in porous media.

2.1 Liquid crystals

2.1.1 *States of matter*

Liquid crystals are a kind of soft matters. They are anisotropic fluids and partially crystalline, and located between ordered solid state and isotropic liquid. Discovery of liquid crystals goes back to the year 1888 when the Austrian botanist Friedrich Reinitzer reported that the compounds cholesteryl benzoate and cholesteryl acetate had apparently two melting points before it reached the liquid state (Reinitzer, 1888; Kawamoto, 2002). In his discovery, he observed that the compounds did not melt to a transparent or clear liquid but always formed a muddy fluid. Further increase in temperature of the muddy fluid caused the muddiness of the fluid to disappear and a transparent liquid was formed. This unusual phenomenon of the compounds did not only relate to the existence of two melting points, but also had some colour, which shows the typical light scattering with selective reflection. Even though Reinitzer understood that the compounds he was investigating had unusual states of matter, he had no strong evidence to prove or explain the new findings (Mettenheimer, 1857; Loebisch, 1872; Kawamoto, 2002). For further investigation, Reinitzer sent the samples to Otto Lehmann who was a specialist in polarizing microscopy and the successor of Heinrich Hertz in Karlsruhe. One year later, Lehmann introduced the term “flüssiger kristall” which meant liquid crystal for the compounds which at that time, show the special behavior (Lethmann, 1889; Kawamoto, 2002).

Liquid crystal materials are usually divided in two categories known as thermotropic liquid crystals and lyotropic liquid crystals. Each categories of liquid crystal shows typical mesophase between the solid and liquid states. In addition, the term

“mesophase” originates from the Greek word *meso*, meaning “in between”. The thermotropic liquid crystals experience phase transition when temperature is changing. Whereas the phase transition of lyotropic liquid crystals are governed by the concentration of the solvent (e.g. water). Therefore, the lyotropic mesophase occurs in a mixture. Meanwhile, thermotropic liquid crystals contain single type of molecules. Some reported mesogens can exhibit thermotropic and lyotropic behaviors, these liquid crystals are called amphotropic liquid crystals. Until now, there are about 80000 different materials as well as polymeric compounds which exhibit liquid crystal properties. Most of them are collected in the database named LiqCryst (Vill, LiqCryst database). This database provides listed phase behavior, physical properties and literature references of the liquid crystals.

The thermotropic liquid crystals can be differentiated by their molecular shape of the constituent molecules, such as rod-like (calamitic) and disk-like (discotic) molecules. A usual molecular structure of calamitic mesogen contains a relatively rigid core, which always relate to phenyl and biphenyl groups. This core is connected to two flexible endgroups, which are often alkyl or alkoxy chains. Whereas in the discotic mesogens, six flexible endgroups are connected to a rigid and disk-like core. The variation to these molecular structures can be changed by different methods of synthesis. Thus, there is a large variety of liquid crystal materials that are known today.

2.1.2 Liquid crystal nomenclature

The nomenclature of liquid crystals is important for researcher to describe the phase of compounds. Nevertheless, the terminologies of liquid crystal phases have

undergone continuous changes. In 1922, not many mesogenic materials were known; Friedel (Friedel, 1922; Demus et al., 1998) introduced the classification of liquid crystal phases into nematic, cholesteric and smectic;

- Nematic is known as crystal phase with long range orientational order,
- Cholesteric is the helical nematic phase for compounds derived from cholesterol,
- Smectic is the phase with additional order with a layered structure.

Polarizing microscopy technique can be used to distinguish the phase of a mesogen by observing their typical texture.

In the 1950s and 1960s, many different types of smectic phases were discovered. Most of them were found by the liquid crystal group at Halle University, which has many years of experience in liquid crystal research. It can be dated back to the days of Daniel Vorländer. At that time, the nomenclature of assigning letters to distinguish the phases was introduced (Arnold et al., 1959; Demus et al., 1998). The phases were named with alphabets in the order of their founder. However, this procedure caused some confusion when the names of the phases were compared with the names used by other liquid crystal groups. For example, some groups named same phases with different alphabets, or different phases with the same alphabets. Then, Sackmann and Demus proposed the rule of miscibility (Sackmann et al., 1966; Demus et al., 1998) to solve the identification problem of liquid crystal phases. They stated that the phases were equivalent if the unknown phase was miscible with the reference phase over the

whole concentration range. Otherwise, no conclusions can be made if unknown and reference phases were not miscible.

The discovery of novel chiral liquid crystals like twist grain boundary (TGB) and smectic C* subphases has also confused the nomenclature of phases at that time. For example, in early papers the TGBA* phase was called SmA*, where the asterisk (*) was denoted as the helical superstructure. This was misleading, because a distinction has been established between SmA (the phase composed of achiral molecules) and SmA* (the phase composed of chiral molecules) where both phases show non-helical superstructures. The reason for the distinction between the phases was due to their different properties. For example, the SmA* phase exhibits the molecular optical activity and the electroclinic effect (Garoff et al., 1977; Demus et al., 1998), but SmA does not show those effects. Thus, most people were using the recommendation suggested by Lagerwall (Lagerwall, 1988) and use the asterisk (*) to declare the phases which were composed of chiral molecules and also a non-helical superstructure. In addition, the isotropic phase of chiral molecules was denoted as Iso*. It was used to distinguish from the isotropic phase of achiral liquid crystals.

To summarize the nomenclature of liquid crystals, the following recommendation of the International Liquid Crystal Society (ILCS) and the International Union of Pure and Applied Chemistry (IUPAC) (Bar  n, 2001) were used in this dissertation;

Table 2.1: The phase transitions and their symbols.

Phases	Symbols
Crystalline	Cr
Smectic liquid crystals	SmA, SmB, SmC, SmI, SmF
Nematic	N
Blue Phase	BP
Cubic	Q
Columnar	Col
Isotropic	Iso

2.1.3 Types of Liquid crystals

Two type of liquid crystals are described in this section:

➤ Thermotropic liquid crystals

The thermotropic liquid crystals exhibit the mesophase in a certain temperature range. If the temperature is too high, the thermal motion of molecules will destroy the cooperative order of the liquid crystal phases. Thus, it will form conventional isotropic liquid crystals. Otherwise, if the temperature is too low, the liquid crystal compounds will form conventional crystals (Chandrasekhar, 1992; de Gennes et al., 1993). Most of the thermotropic liquid crystals exhibit variety of phases when temperature is changed. It means that, a compound can show more than two mesophases like smectic, nematic and finally isotropic phases when temperature increases. For example, para-azoxyanisole (Shao et al., 1998) is a compound which shows thermotropic liquid crystal character.

➤ Lyotropic liquid crystals

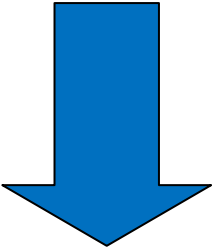
Lyotropic liquid crystals are materials containing more than two components, which exhibit liquid-crystalline behavior in certain range of concentrations. In the mesophase of lyotropic liquid crystals, the molecules of solvent will provide the fluidity to the system (Liang et al., 2005), which surrounds the compounds. Compared to the thermotropic liquid crystals, this lyotropic behavior provides more degree of freedom to enable them to form more variety of different mesophases. For example, soap is a lyotropic liquid crystal.

The compound consisting of hydrophilic and hydrophobic parts in the same molecule is named amphiphilic molecule. Many amphiphilic molecules exhibit lyotropic liquid-crystalline behavior and the behaviour is depends in the balances of the ratio between the hydrophilic and hydrophobic parts. In addition, the content of solvent molecules (such as water) can change the self-arrangement of the compound molecules. At very low concentrations of solution, the molecules will move randomly and without any ordered arrangement. But, at slightly higher concentration, the amphiphilic molecules will self-assemble into micelle structures. In the micelle structure, the hydrophobic part of amphiphilic molecules will self-arrange inside the micelle as a core and expose the hydrophilic part to the aqueous solution. These spherical structures will not exist in solution with low concentrations. At higher concentrations of solution, the spherical structures will assemble in an order arrangement. One typical mesophase is hexagonal columnar phase where the amphiphilic molecules form long cylinders in which they arrange themselves into hexagonal lattices. This is also known as the middle soap phase. At a higher concentration, a lamellar phase may form. It is also known as a neat soap phase. This extended sheet of amphiphilic molecules is

separated by a thin layer of solvent (e.g. water). For some other systems, like cubic phase (or viscous isotropic phase) the extended sheet may occur between the columnar and lamellar phases where spherical structures are formed, inducing a cubic lattice. These spherical objects are connected to each other to form a bicontinuous cubic phase.

The structure formed by amphiphilic molecules are usually in a spherical form (example micelle). Sometimes the amphiphilic molecules may form disc-like, rod-like or biaxial structures. These self-assemblies of nano-structures of lyotropic liquid crystal can arrange themselves to form a mesophase. The self-assembly of lyotropic liquid crystals is similar to thermotropic liquid crystals. They will form a large-scale version of structure. Furthermore, at higher concentrations, the inverse phase's phenomena may be observed. For example, an inverse micellar phase is formed when a bulk liquid crystal sample has insufficient water solvent. In addition, even in the same phases, the self-assembly of structures will be influenced by the concentration of the solvent. For example, the layer distance in lamellar phases will increase with the ratio of solvent. For the lyotropic liquid crystals, the usual progression of phase sequence, transform from low to high concentrations as listed in Table 2.2;

Table 2.2: The phase sequence transform from low to high concentrations.

Discontinuous cubic phase (micellar cubic phase)	<div style="text-align: center;"> <p>Low concentration</p>  <p>High concentration</p> </div>
Hexagonal phase (hexagonal columnar phase)	
(middle phase)	
Lamellar phase	
Bicontinuous cubic phase	
Reverse hexagonal columnar phase	
Inverse cubic phase (Inverse micellar phase)	

2.2 Glycolipid liquid crystals

Glycolipid materials are a special class of liquid crystals because they have several different roles when compared to the usual monophilic liquid crystals (the classical liquid crystals which are used for traditional display devices). The glycolipids liquid crystals have some interesting applications (Jeffrey et al., 1992; Prade et al., 1995; Blunk, 1998). The molecules of glycolipid liquid crystals contain hydrophilic and hydrophobic parts. It is also known as amphiphilic liquid crystals. The hydrophilic part usually contains monosaccharide or disaccharide sugar head which is the water-like part. Whereas the hydrophobic part is the hydrocarbon chain like regioisomers (2-alkyl, 3-alkyl, 4, 6-dialkyliden, etc). Therefore, hundreds of different compounds can be synthesized, which induces a variety of carbohydrate mesogens (Vill, 1989; Singh et al., 2009). The mesophase behavior can be divided into two basic concepts. One of the concept states that the molecules of mesogenic compounds can be packed in an ordered arrangement and provide the shape-driven mesophase transition. This is known as liquid crystal phase. Another concept states that the molecules of mesogenic compounds are arranged in random way, which is known as isotropic phase.

The compound named hexadecyl- β -D-glucopyranoside was the first reported glycolipid, which exhibited double melting points (Fischer et al., 1911; Hori, 1958; Vill et al, 2002, Singh et al., 2009). This compound consists of two molecular parts, that is sugar residue (hydrophilic and polar) and paraffin chain (lipophilic and apolar). Usually, glucose does not dissolve in hexadecane; but in the glycolipid molecule, the incompatible components cannot be separated macroscopically because they are connected by molecular bonds. Furthermore, they experience the microscopic separation between hydrophilic and lipophilic layers. These formations of layer

structures in Smectic A have the same geometry as the monophilic liquid crystals. Therefore, the mesophase of glycolipid has similar physical properties but the chemical properties are very different. In addition, the carbohydrate liquid crystals have some interesting behaviors and properties which are influenced by the variety of functional sugar head groups (Hinz et al., 1985; Engels et al., 1998; Nilsson et al., 1996; Vill et al, 2002) as listed below;

- ❖ Low melting point,
- ❖ Non-toxic,
- ❖ Solubility in water and organic solvents,
- ❖ Chirality,
- ❖ Degradation,
- ❖ Accessibility.

Glycolipids can exhibit mesophases in melted state (thermotropic behavior) and in solution form (lyotropic behavior). Thus, researchers have used the term amphotropic liquid crystals to note the compounds, which exhibited both behaviors (Baron, 2001).

2.2.1 Natural glycolipids

Glycolipid materials are the type of soft matter which are known as glycoconjugates (Allen et al., 1992). They were produced when carbohydrates interact with bio-molecules. For example, glycolipids were formed when carbohydrates are connected to lipids or glycoproteins were produced when carbohydrates are covalently bonded to proteins. Usually, glycolipid materials can be found in natural resources (Zhang et al., 1996). They are very important in membrane components. It is because they exist in the exterior of lipid layer of cell boundaries and are active in intercellular recognition

processes (Lochmit, 2001). The natural glycolipids can be classified as glycosphingolipids (GSLs), glycoglycerolipids and glycosyl phosphopolyprenols.

2.2.2 Synthetic glycolipids

Many synthetic glycolipid compounds have been synthesized by researchers where the sugar head group was covalently bonded to the lipid components through an ether linkage, ester linkage or amide linkage (Kawaguchi et al., 1983; Attard et al., 1994; Boullanger, 1997; Vill et al., 2000). These synthetic materials have some interesting applications in food industries, detergents, pharmacy and cosmetics. Furthermore, the two sugar head units named disaccharides were reported for carbohydrate liquid crystals and exhibited the cubic mesophase (Fischer et al., 1994). Some substituted disaccharide unit like α - and β -anomers have been synthesized from cellobiose octaalkanoate (A. Takada et al., 1995). The compounds maltotriose with the sugar head units more than two have also been synthesized (Vill et al., 1989, Singh et al., 2009).

2.3 Dielectric properties and conductivity

2.3.1 Dielectric properties

Dielectric spectroscopy is a technique used to investigate the dielectric properties of an insulator material. The dielectric properties of a sample are influenced by localized charge and type of polarizations which will determine their dielectric strength, dynamic of molecule and interaction. It will be depicted in complex dielectric permittivity with real component known as dielectric constant or real permittivity, ϵ'

and imaginary component represented by dielectric loss or imaginary permittivity, ε'' . Permittivity of a sample is caused by polarization phenomena when an electric field is applied. Polarization phenomena can occur due to asymmetric alignment of molecules itself or due to the application of an external electric field force which induces dipole moments. If an external electric field is applied by a sinusoidal mode, then the polarity of a sample will change according to the electric field.

The dielectric constant or real permittivity, ε' can be calculated from capacitance formulae as shown in Equation 2.1;

$$\varepsilon' = \frac{C t}{\varepsilon_o A} \quad \text{Equation 2.1}$$

where C and t are capacitance and thickness of thin film respectively. Meanwhile, ε_o is the absolute permittivity of free space ($8.8542 \times 10^{-12} \text{ F m}^{-1}$) and A is the area of electrode. In order to understand dielectric properties of materials, ε' will be measured as a function of frequency.

The movements of molecules will alternate by change due to the polarity of the external electric field. There is delay in the motions of molecules and can be determined by loss angle, δ or phase shift. This delay is due to the resistance of motions, which is influenced by the interaction between molecules. Dissipation factor, D or dielectric loss tangent, $\tan \delta$ is a quantitative parameter to determine lossy of a medium which is caused by an internal resistance. The dielectric loss or imaginary permittivity, ε'' is related to two components which are dielectric constant and dielectric loss tangent. The dielectric loss formulae is shown in Equation 2.2;

$$D = \tan \delta = \frac{\varepsilon''}{\varepsilon'} \quad \text{Equation 2.2}$$

In a medium between electrodes, when the alternating external electric field changes, the polarization simultaneously changes too. At a certain frequency, f if the polarization cannot stay in phase with the external electric field, dielectric relaxation occurs and induces greater power loss. Normally, interfacial and orientation polarization occur in low (low audio frequency range) and intermediate (radio frequency range) frequencies respectively. These polarizations are comparatively slow when compared with the atomic and electronic polarization, which occur beyond infrared frequency range. Furthermore, the relaxation time, τ can be observed from polarization processes where dielectric losses show a prominent peak with a maximum value. It can be calculated via Equation 2.3 where f_{max} is the frequency at a maximum dielectric loss.

$$\tau = \frac{1}{2\pi f_{max}} \quad \text{Equation 2.3}$$

At a low frequency with an alternating field, dipolar molecules have sufficient time to experience torque and exhibit maximum resultant polarization. It will give a dielectric constant, which is known as static dielectric constant, ε_s . Whereas in higher frequency, the alternating field changes very fast and thus the dipolar molecules do not have enough time to rotate or move. As a result, it shows the instantaneous dielectric constant, ε_∞ .

Several dielectric polarizations had been mentioned, which studies a medium with the presence of an alternating electric field. In general, the dielectric polarization can be

divided from low to high frequency as interfacial, orientation, atomic and electronic respectively;

➤ Interfacial polarization

Interfacial or space charge polarization occurs when more than one type of material is present between electrodes. The polarization occurs due to the accumulation of charge carriers at boundaries, which induces macroscopic distortion of the electric field. Then, the movement of charge carriers will be restricted and trapped in interfaces or boundaries, so that the charge carriers cannot be freely discharged. This distortion will influence the dielectric properties of materials to increase the value of the dielectric constant. The polarization can occur in several locations such as grain boundaries, interphase boundaries and surfaces.

➤ Orientation polarization

The materials have asymmetrical molecular structures. It can induce permanent dipole moment or dipolar to the molecules, such as water. With the absence of an external electric field, the dipolar molecules will randomly move and collide with other molecules. Meanwhile, dipole moment of the molecules will be freely orientated without a particular direction. When an external electric field is applied, each dipolar molecule has a torque and tend to align according to the field direction to give a resultant polarization. This phenomenon is known as orientation polarization or dipole polarization.

➤ Atomic polarization

Atomic polarization is observed when the applied electric field distorts atomic nuclei. Such that, the nucleus of the atom rearrange according to the applied field. This polarization is considered as a resonant process. Atomic polarization occurs at higher frequency compared to interfacial and orientation polarizations. However, when contrasted with electronic polarization, atomic polarization is comparatively slower due to response of heavy nuclei which is not as fast as electrons.

➤ Electronic polarization

When an electric field is applied, the electron cloud surrounding an atom is distorted along the direction of the field and produces a dipole moment. The polarization is known as electronic polarization. Furthermore, the distortion to the electron cloud is confined and relatively small due to the strong intra-atomic field from a nucleus. In addition, the ratio of the dipole moment to the electric field strength can determine the polarizability of a polarization.

This dielectric spectroscopy technique uses alternating current (ac) electrical signal which is applied to the sample. This technique observes complex response which indicate real and imaginary component as a function of frequency. Usually, for an insulator material, capacitance can be determined for quantitative measurement to illustrate the dielectric properties. In 1967, Daniel (Daniel, 1967; Tuncer et al., 2002) described the complex capacitance $C(\omega)$ as the following equation;

$$C(\omega) = C'(\omega) - iC''(\omega) \quad \text{Equation 2.4}$$

$$= \frac{\varepsilon_o A}{t} [\varepsilon'(\omega) - i\varepsilon''(\omega)] - \frac{i\sigma A}{\omega t} \quad \text{Equation 2.5}$$

where $\omega = 2\pi f$,

f = frequency,

ε_o = absolute permittivity of free space (8.8542×10^{-12} F m⁻¹),

A = area of electrode,

t = thickness between electrodes,

σ = direct current (DC) conductivity in S m⁻¹.

Normally, the complex dielectric permittivity, $\varepsilon^*(\omega)$ as a function of frequency is written as;

$$\varepsilon^*(\omega) = \varepsilon'(\omega) - i\varepsilon''(\omega) \quad \text{Equation 2.6}$$

The Debye model (Daniel, 1967; Tuncer et al., 2002) illustrates complex dielectric permittivity as below;

$$\varepsilon^* = \varepsilon_\infty + \frac{\varepsilon_s - \varepsilon_\infty}{1 + i\omega\tau} \quad \text{Equation 2.7}$$

with real component, $\varepsilon'(\omega) = \varepsilon_\infty + \frac{\varepsilon_s - \varepsilon_\infty}{1 + \omega^2\tau^2}$ Equation 2.8

and imaginary component, $\varepsilon''(\omega) = \varepsilon_\infty + \frac{(\varepsilon_s - \varepsilon_\infty)\omega\tau}{1 + \omega^2\tau^2}$ Equation 2.9

where ε_∞ = instantaneous dielectric constant at high frequency.

ε_s = static dielectric constant at low frequency.

τ = relaxation time.

This Debye model describes single relaxation process of dielectric behavior. In reality, the model was not sufficient to describe the dielectric behavior of insulator, such as polymers and liquid crystals. It was because the relaxation process of some insulators show broadened relaxation peak. In 1941, Cole and Cole (Cole and Cole, 1941; Tuncer et al., 2002) modified the Debye model by introducing an exponent parameter, α where the value of α is between 0 and 1. The Cole-Cole equation is expressed as below;

$$\varepsilon^* = \varepsilon_{\infty} + \frac{\varepsilon_s - \varepsilon_{\infty}}{1 + (i\omega\tau)^{\alpha}} \quad \text{Equation 2.10}$$

In 1950, Cole and Davidson further derived the Debye model and introduced Cole-Davidson equation. The Cole-Davidson equation is illustrated as below;

$$\varepsilon^* = \varepsilon_{\infty} + \frac{\varepsilon_s - \varepsilon_{\infty}}{(1 + i\omega\tau)^{\beta}} \quad \text{Equation 2.11}$$

In 1966, Havriliak and Negami (Havriliak and Negami, 1966; Tuncer et al., 2002) derived an empirical equation, which is a combination of Cole-Cole and Cole-Davidson equations. This Havriliak-Negami (HN) equation is used to describe the broadness and asymmetry of a dielectric spectra as a function of frequency. In 1967, the HN equation was used to depict dielectric relaxation process of some polymers (Havriliak and Negami, 1967). Furthermore, this equation was used to fit observed data for polymer solutions and amorphous polymers. The fitting results were satisfied over a wide range of frequency (Cole, 1980). The HN equation is expressed as below;

$$\varepsilon^* = \varepsilon_{\infty} + \frac{\varepsilon_s - \varepsilon_{\infty}}{(1 + (i\omega\tau)^{\alpha})^{\beta}} \quad \text{Equation 2.12}$$

Exponent parameters α and β are used to represent the broadness and asymmetry of a dielectric dispersion spectra. The parameter τ is the relaxation time of HN function.

2.3.2 Conductivity

Materials can conduct electric current when there are potential differences between electrodes, or an electric field is applied. If the electric field strength is low, the conduction process usually shows ohmic behavior. When the electric field strength increases, the conduction process becomes electric field dependent. Further increase in the electric field strength will cause breakdown or destruction in the medium.

Ohm's law equation exhibits the relation between current I and applied voltage V which can be written as;

$$V = IR \quad \text{Equation 2.13}$$

where R = resistance of the material.

Resistivity ρ is known as the resistance opposing the flow of electric current. The resistivity equation is as shown below;

$$\rho = \frac{RA}{l} \quad \text{Equation 2.14}$$

where l = distance between two electrodes,

A = cross section area which is perpendicular to the flow of current.

The electrical conductivity σ is used to measure the ability of the materials to conduct electric current. It is also known as reciprocal of the resistivity, which is shown below;

$$\sigma = \frac{1}{\rho} \quad \text{Equation 2.15}$$

Substituting Equation 2.15 with Equation 2.13 and 2.14, the Ohm's law can be presented as below;

$$J = \sigma E \quad \text{Equation 2.16}$$

where J = current density,

E = electric field strength.

The conductivity behavior in dielectric materials is contributed by electronic or ionic conduction. Somehow, both contributions can exist together in the materials. It is difficult to separate both components experimentally, especially in high electric field strength. But, the theoretical concept for both components is different. Usually, the fundamental equation for electrical conductivity is as shown in Equation 2.17;

$$\sigma = \sum_j n_j e_j \mu_j \quad \text{Equation 2.17}$$

where n_j = density of charge carrier,

e_j = charge of carriers,

μ = mobility.

The electrical conduction is known as the flow of current, which is induced by the movement of electrons in the opposite direction. This electrical conduction can appear

in conductor and semiconductor materials, or even in some insulator materials. In the conductor materials, the conduction process is contributed by movement of electrons. Whereas for semiconductor materials, the conduction process are contributed by electrons and holes. But, for the insulator materials, the conduction process is mostly carried-out by the ions. The number of charge carriers can directly affect the value of electrical conductivity.

There was some direct current (dc) conduction mechanisms identified as electrode polarization, interfacial polarization, tunneling of charge carriers and hopping of charge carriers. Several models have been proposed to describe the dc conduction mechanisms such as (Alagiriswamy et al., 2002);

➤ Ionic hopping

$$J = J_o(T) \exp\left(\frac{Eaq}{2k_B T}\right) \quad \text{Equation 2.18}$$

where E = applied electric field,

a = ionic hopping length,

q = electronic charge,

k_B = Boltzmann constant,

T = absolute temperature.

➤ Space charge limited current (SCLC)

$$J_{SCLC} = \frac{9\varepsilon_o\varepsilon\mu\theta V^2}{8x_t^3} \quad \text{Equation 2.19}$$

where ε_o = permittivity in vacuum,

ε = dielectric constant,

μ = mobility of charge carriers,

θ = fraction of free carriers to trap carriers in term of concentration,

V = applied voltage,

x_t = effective width of the space charge domain.

➤ Schottky effect

$$J_s = AT^2 \exp\left(\frac{q}{k_B T} \sqrt{\frac{qE}{4\pi\varepsilon_o\varepsilon}} - \frac{q\phi_s}{k_B T}\right) \quad \text{Equation 2.20}$$

where A = constant,

T = absolute temperature,

q = electronic charge,

k_B = Boltzmann constant,

E = electric field,

ε_o = permittivity in vacuum,

ε = dielectric constant,

ϕ_s = barrier height for the electron injection.

Furthermore, many materials have been studied for electrical conductivity σ and most of them obey the Arrhenius relation as follows;

$$\sigma = \sigma_o \exp\left(-\frac{E_a}{k_B T}\right) \quad \text{Equation 2.21}$$

where σ_o = electrical conductivity at absolute zero which can be observed by extrapolation,

E_a = activation energy,

k_B = Boltzmann constant,

T = absolute temperature.

2.4 Pyroelectric effect

Pyroelectricity is defined as the ability of materials having spontaneous polarization to generate a temporary current when the temperature changes (Lang, 1947; Lines et al., 1977; Lang, 2004). Each molecule in a pyroelectric compound has a dipole moment. When all the molecules are packed together, the dipole moment of molecules will add up and induce a net dipole moment. This net dipole moment per unit volume is known as spontaneous polarization in the absence of an applied electric field. When there is no change in temperature, the polarization of the molecules remain constant. Thus, there is no current flow. When the temperature is increased, it will cause the dipole moment or spontaneous polarization to decrease. As a result, a quantity of bounded charge decreases. Subsequently, the free charges will be redistributed to compensate the lack in the bounded charge. Therefore, it will induce a current flow in the circuit and this current is known as pyroelectric current. When the temperature of a sample is decreased, the sign of the current will be reversed. It is noted that the pyroelectric effect occur when temperature changes. This pyroelectricity is different from thermoelectricity. In pyroelectricity, the temperature

of a sample is heated or cooled periodically or alternatively, it will cause a change in dipole moment, as a result it induces a temporary current. In thermoelectricity, one side of a sample is at constant temperature and another side is at a different constant temperature producing a permanent current to flow.

There are many pyroelectric materials such as lead zirconate titanate (ceramic), polyvinylidene fluoride (polymer) and collagen (bio-material). Their pyroelectric effect is contributed by several properties such as thermal, mechanical and electrical properties (Lang, 2005). Figure 2.1 illustrates the reversible thermodynamic interaction among the thermal, mechanical and electrical properties of materials.

The pyroelectricity has a coupled effect when temperature changes. It induces the change in electrical displacement \mathbf{D} (with units of C m^{-2});

$$d\mathbf{D} = \mathbf{p} d\theta \quad \text{Equation 2.22}$$

where \mathbf{p} is pyroelectric coefficient (with unit of $\text{C m}^{-2} \text{K}^{-1}$). The pyroelectric coefficient \mathbf{p} can also be defined as:

$$\mathbf{p} = \left(\frac{\partial \mathbf{P}_s}{\partial \theta} \right)_{T,E} \quad \text{Equation 2.23}$$

where \mathbf{P}_s is the spontaneous polarization. The constraints in Equation 2.23 are known as constant elastic stress \mathbf{T} and constant electric field \mathbf{E} .

The colour lines in Figure 2.1 indicate the two parameters which contribute to pyroelectric effect. In the first contribution, the sample is clamped under the constant

strain S . It will prevent the expansion or contraction of the sample. The change in temperature will influence the electric displacement D (shown by the blue line). This effect is known as primary pyroelectric effect. In the second contribution, the thermal expansion of the sample causes a strain S that affect the electric displacement D through the piezoelectric process (shown by the dashed red line). This contribution is known as secondary pyroelectric effect.

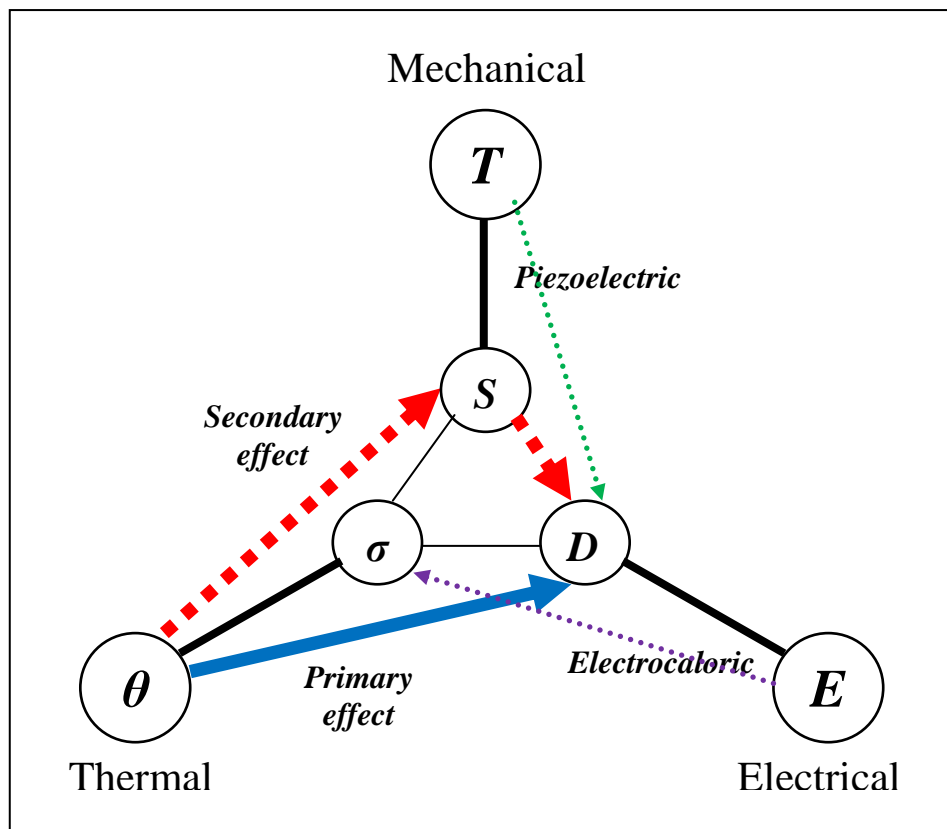


Figure 2.1: Illustration of the reversible thermodynamic interaction among the thermal, mechanical and electrical properties

In experiment, the measurement of pyroelectric effect is the total effect coming from both contributions. Actually, in order to measure the primary pyroelectric effect directly is difficult. However, the secondary pyroelectric effect can be calculated from three coefficients; thermal expansion, elastic stiffness and piezoelectric strain. When a non-uniform heat is applied on the sample, it will produce a non-uniform stress

through the piezoelectric effect. This is called tertiary pyroelectric effect. In addition, inverse pyroelectric effect occurs when the electric field is changed and influences the entropy and temperature. It is also called electrocaloric effect. In order for pyroelectric effect to exist in materials, the molecular structure of the materials have to contain these properties;

- ❖ Non-zero dipole moment,
- ❖ No center of symmetry,
- ❖ No axis of rotational symmetry.

2.5 Diffusion process

The diffusion process is one of the transport methods of individual particles that occur in nature. To distinguish the diffusion process from other transport phenomena, it occurs in mass transport and without bulk motion. Mass transport is defined as the net movement of mass (usually indicating phase, fraction or component) from one position to another. The bulk motion is defined as observable movement of component such as fluids. Two ways of diffusion process are introduced to identify the concept of diffusion. One is the phenomenological approach to Fick's law in diffusion process and their mathematical significant (Fick, 1855; Philibert, 2005). Another way is the diffusion of particles in random walk scheme (Philibert, 2005). According to the phenomenological approach which obeys the Fick's laws, the diffusion flux of the system is proportional to the (negative sign) gradient of concentration. It transfers from higher to lower concentration regions. In 1827, Robert Brown discovered the random walk phenomena of small particles in suspension fluid. After sometimes, the theory of the Brownian motion and diffusion process were

developed by Albert Einstein (Einstein, 1905; Philibert, 2005). The principle of diffusion is applied in many fields, such as particle diffusion in physics, diffusion of fluids in chemistry and biology, diffusion of people in sociology and several others.

2.5.1 Basic model of diffusion

The diffusion flux in models is used to express several quantities such as density, concentration, mass energy and their derivatives. The common symbol of flux is \mathbf{J} and it is a vector quantity. For a system containing diffusion quantity N (it can be electric charge, mass or number of particles) in a surface or volume, the density n of the system can be determined. For this density n , the general diffusion equation is;

$$\frac{\partial n}{\partial t} = -\nabla \cdot \mathbf{J} + W \quad \text{Equation 2.24}$$

where W is the intensity of local source.

➤ Fick's law and equations

Fick's first law states that the diffusion flux is proportional to the (negative sign) concentration. The equation is as shown below;

$$\mathbf{J} = -D \frac{\partial \phi}{\partial x} \quad \text{Equation 2.25}$$

where \mathbf{J} = diffusion flux [(amount of substance) / (area X time)],

D = diffusion coefficient or diffusivity [length² / time],

ϕ = concentration [(amount of substance) / volume],

x = position [length].

Whereas, Fick's second law predicts the influence of diffusion process which affect the change in concentration with respect to time;

$$\frac{\partial \phi}{\partial t} = D \frac{\partial^2 \phi}{\partial x^2} \quad \text{Equation 2.26}$$

where ϕ = concentration [(amount of substance) / volume],

t = time [time],

D = diffusion coefficient or diffusivity [$\text{length}^2 / \text{time}$],

x = position [length].

➤ Einstein-Smoluchowski relation

The Einstein-Smoluchowski relation (or also known as Einstein relation) relates the concept of Brownian motion proposed by Albert Einstein with that of Marian Smoluchowski (Einstein, 1905; Smoluchowski, 1906; Islam, 2004). This Einstein-Smoluchowski relation relates the diffusion coefficient with mobility (Bromberg et al., 2002) as shown below;

$$D = \mu k_B T \quad \text{Equation 2.27}$$

where D = diffusion coefficient,

μ = mobility or the ratio of drift velocity to applied force,

k_B = Boltzmann's constant,

T = absolute temperature.

Some equations frequently used for special cases are;

- ❖ Electrical mobility equation (for diffusion process of charged particles):

$$D = \frac{\mu_q k_B T}{q} \quad \text{Equation 2.28}$$

- ❖ Stokes-Einstein equation (for diffusion process of spherical particles through liquid):

$$D = \frac{k_B T}{6\pi\eta r} \quad \text{Equation 2.29}$$

where q = electrical charge of a particle,

μ_q = electrical mobility of charged particle,

η = viscosity,

r = radius of spherical particle.

- Diffusion in porous media

The diffusion in porous media is a process through the pore space in the media (Grathwohl, 1998). In nature, this diffusion process is in macroscopic feature because it has to consider the entire pore space. The effective diffusion, D_e for the transportation through the pore in media is shown as below;

$$D_e = \frac{D \epsilon_t \delta}{\tau} \quad \text{Equation 2.30}$$

where D = diffusion coefficient in gas or liquid filling the pore,

ε_t = porosity for the transport,

δ = constrictivity,

τ = tortuosity.

.

Among these models, Einstein-Smoluchowski relation is more relevant to glycolipid compounds. It was used to analyze the diffusion process of glycolipid thin film.

2.6 Summary

Liquid crystal is a soft matter which is partially crystalline and located between ordered solid state and isotropic liquid. The first liquid crystal was reported by Friedrich Reinitzer in 1888. With the help from Otto Lehmann, the compounds which show the special behaviour were identified as “flüssiger kristall” which means liquid crystal. Nomenclature of liquid crystals follows the recommendation of ILCS and the IUPAC to avoid confusion. The types of liquid crystals can be differentiated as thermotropic and lyotropic liquid crystals. In addition, the glycolipid liquid crystals can be found in natural source or can be synthesized. Dielectric spectroscopy can be used to study the dielectric properties of an insulator. Several dielectric polarizations such as interfacial, orientation, atomic and electronic polarization can be observed when applying an alternating electric field from low to high frequency. Electrical conductivity was used to investigate the ability of materials to conduct electrical current. Several models can be proposed to depict the dc conduction mechanism such as ionic hopping, space charge limited current or Schottky effect. Pyroelectricity is identified as the ability of materials, which has spontaneous polarization to generate a temporary current when the temperature changes periodically or alternatively. The

pyroelectric effect can be contributed by several properties such as thermal, mechanical and electrical properties. Diffusion process meanwhile is a transport method of individual particles that occur in nature. This process can be identified in two systems, which are known as phenomenological approach to the Fick's law or random walk scheme. Several modes can be proposed to describe the diffusion process such as Fick's law, Einstein-Smoluchowski relation or diffusion in porous media.

References

- Alagiriswamy, A. A., Narayan, K. S., Govinda Raju (2002). Relaxation processes in aromatic polyimide. *Journal of Physics D: Applied Physics*, **35**, 2850-2856.
- Allen, H. J., Kisailus E. C. (1992). Glycoconjugates: composition, structure and function, Marcel Dekker Inc, USA.
- Arnold, H., Sackmann, H. (1959). *Z. Elektro-chem. Angew. Phys. Chem.*, **63**, 1171.
- Attard, G. S., Blackaby, W. P., Leach, A. R., (1994). Aggregation behavior of two structurally isomeric glycolipids, *Chemical and Physics of Lipids*, **74**, 83–91.
- Baron, M. (2001). Definition of basics terms relating to low molar mass and polymer liquid crystals, IUPAC recommendation 2001. *International Union of Pure and Applied Chemistry*, **73**, 845-895.
- Barón, M. (2001). Definitions of basic terms relating to low-molar-mass and polymer liquid crystals (IUPAC Recommendations 2001). *Pure and Applied Chemistry*, **73**, 845-850
- Blunk, D., Praefcke, P., Vill, V. (1998). Handbook of Liquid Crystals; 3, Chapter 6: 305–340.
- Boullanger, P. (1997). Amphiphilic carbohydrates as a tool for molecular recognition in organized systems, *Topics in Current Chemistry*, **187**, 275–312.
- Bromberg, S., Dill, K. A. (2002), Molecular Driving Forces: Statistical Thermodynamics in Chemistry and Biology, Garland Science.
- Chandrasekhar, S. (1992). *Liquid Crystals* (2nd ed.). Cambridge: Cambridge University Press.
- Cole K. S., Cole, R. H. (1941). Dispersion and Absorption in Dielectrics - I Alternating Current Characteristics. *Journal of Chemistry Physics.*, **9**, 341–352.
- Cole, R. H. (1980). Molecular correlation function approaches to dielectric relaxation. Institute of Physics Conference series No. 58, Invited paper presented at Physics of Dielectric Solid, Canterbury.
- Daniel, V. (1967). Dielectric relaxation. New York: Academic.
- de Gennes, P.G., Prost, J. (1993). The Physics of Liquid Crystals. Oxford: Clarendon Press.
- Demus, D., Goodby. J., Gray, G.W., Spiess, H. -W., Vill, V. (1998). Handbook of Liquid Crystals, vol. 3, Wiley-Vch, Verlag GmbH, pp. 17-25.

- Einstein, A. (1905). Über die von der molekularkinetischen Theorie der Wärme geforderte Bewegung von in ruhenden Flüssigkeiten suspendierten Teilchen. *Annalen der Physik*, **322**(8), 549-560.
- Engels, T., von Rybinski, W. J. (1998). Liquid crystalline surfactant phases in chemical applications, *Journal of Materials Chemistry*, **8**, 1313–1320.
- Fick, A. (1855). Ueber Diffusion. *Annalen der Physik*, **170**(1), 59-86.
- Fischer, E., Helferich, B. (1911). Über neue synthetische glycoside, *Liebigs Annalen der Chemie*, **383**, 68–91.
- Fischer, S., Fischer, H., Diele, S., Pelzl, G., Jankowski, K., Schmidt, R. R., Vill, V. (1994). On the structure of the thermotropic cubic mesophases, *Liquid Crystals*, **17**(6), 855–61.
- Friedel, G. (1922). Les états mésomorphes de la matière. *Ann. Phys. (Fr.)*, **18**, 273–474.
- Garoff, S., Meyer, R. B. (1977). Electroclinic Effect at the A-C Phase Change in a Chiral Smectic Liquid Crystal. *Physical Review Letter*, **38**, 848-852.
- Grathwohl, P. (1998). Diffusion in natural porous media: Contaminant transport, sorption / desorption and dissolution kinetics. Kluwer Academic.
- Havriliak, S., Negami, S. (1966). A complex plane analysis of α -dispersions in some polymer systems. *Journal of Polymer Science Part C: Polymer Symposia*, **14**, 99-101.
- Havriliak, S., Negami, S. (1967). A complex plane representation of dielectric and mechanical relaxation processes in some polymers. *Polymer*, **8**, 161–210.
- Hinz, H. J., Six, L., Ruess, K. P., Lieflander, M. (1985). Head-group contributions to bilayer stability: monolayer and calorimetric studies on synthetic, stereochemically uniform glucolipids. *Biochemistry* **24**, 806–813.
- Hori, R. (1958). Alkyl derivatives of carbohydrates. II. Synthesis of alkyl-b-cellobiosides, *Yakugaku*, **78**, 999–1002.
- Islam, M. A. (2004). Einstein–Smoluchowski Diffusion Equation: A Discussion. *Physica Scripta*, **70**, 120-128
- Jeffrey, G. A., Wingert, L. M. (1992). Carbohydrate liquid crystal, *Liquid Crystals*, **12**, 179–202.
- Kawaguchi, T., Hamanaka, T., Mitsui, T. (1983). X-ray structural studies of some nonionic detergents micelles, *Journal of Colloid and Interface Science*, **96**(2), 437–55.
- Kawamoto, H. (2002). The History of Liquid-Crystal Displays. *Proceeding of the IEEE*, **90**(4), 460-500.

Lagerwall, S. T. (1988). Comments on liquid crystal terminology, nomenclature and conventions. *Ferroelectric*, **85**, 497-501.

Lang, S. B. (1974). Sourcebook of Pyroelectricity, Gordon & Breach Science, London.

Lang, S. B. (2004). A 2400 year history of pyroelectricity: from Ancient Greece to exploration of the solar system. *British Ceramic Transactions*, **103**, 65-70.

Lang, S. B. (2005). Pyroelectricity: From Ancient Curiosity to Modern Imaging Tool, *Physics Today*, **58**(8), 31-39.

Lethmann, O. (1889). *Z. Phys. Chem.*, **4**, 462-468.

Liang, Q., Liu, P., Liu, C., Jian, X., Hong, D., Li., Y. (2005). Synthesis and Properties of Lyotropic Liquid Crystalline Copolyamides Containing Phthalazinone Moieties and Ether Linkages. *Polymer*, **46**(16), 6258–6265.

Lines, M. E., Glass, A. M. (1977). Principles and Applications of Ferroelectrics and Related Materials, Clarendon Press, Oxford.

Lochmit, G., Geyer, R., Heinz, E., Rietschel, E. T., Zähringer, U., Mühling, J. (2001). Glycolipids and glycosphingolipids: chemical biology and biomedicine, plant glycolipids, in: B Fraser-Reid, K Tatsuta, J Thiem (Eds.), Glycoscience: chemistry and chemical biology, vol. III, Springer, Berlin, pp. 2183–252.

Loebisch, W. (1872). *Ber. Deutsch. Chem. Ges.*, **5**, 510.

Mettenheimer, C. (1857). *Corresp. Ver. Gem. Arb. Förd. Wiss. Heilkd.*, **24**, 331.

Nilsson, F., Soderman, I., Johansson, I., (1996). Physical–chemical properties of the n-octyl b-D-glucoside/water system. A phase diagram, self diffusion NMR and SAXS study, *Langmuir*, **12**, 902–8.

Philibert, J. (2005). One and a half century of diffusion: Fick, Einstein, before and beyond. *Diffusion Fundamentals*, **2**, 1.1-1.10.

Prade, H., Miethchen, R., Vill, V. (1995). Thermotropic liquid crystals based on amphiphilic carbohydrates, *Journal für Praktische Chemie*, **337**, 427–440.

Reinitzer, F. (1888). Beiträge zur Kenntniss des Cholesterins, *Monatshefte für Chemie*, **9**, 421-441.

Sackmann, H., Demus, D. (1966). *Molecular Crystals and Liquid Crystals*, **2**, 81-85.

Shao, Y., Zerda, T. W. (1998). Phase Transitions of Liquid Crystal PAA in Confined Geometries. *Journal of Physical Chemistry B*, **102**(18), 3387–3394.

Singh, M. K., Jayaraman, N. (2009). Carbohydrate-based liquid crystals. *Journal of the Indian Institute of Science*, **89**(2), 113-135.

Smoluchowski, M. von (1906). Zur kinetischen Theorie der Brownschen Molekularbewegung und der Suspensionen. *Annalen der Physik*, **326**(14), 756–780.

Takada, A., Ide, N., Fukuda, T., Miyamoto, T., Yamagata, K., Watanabe, J. (1995). Discotic columnar liquid crystals in oligosaccharide derivatives, III. Anomeric effects on thermo-mesomorphic properties of cellobiose octa-alkanoates, *Liquid Crystals* **19**(4), 441–448.

Tuncer, E., Serdyuk, Y. V., Gubanski, S. M. (2002). Dielectric Mixtures: Electrical Properties and Modeling. *IEEE Transactions on Dielectrics and Electrical Insulation*, **9**(5), 809-828.

Vill, V., Böcker, T., Thiem, J., Fischer, F. (1989). Studies on liquid crystalline glycosides, *Liquid Crystals*, **6**(3), 349–356.

Vill, V., Hashim, R. (2002). Carbohydrate liquid crystals: structure-property relationship of thermotropic and lyotropic glycolipids. *Current Opinion in Colloid and Interface Science*, **7**, 395-409.

Vill, V., LiqCryst database: www.lci-publisher.com/liqcryst.html.

Vill, V., Minden, H. M., Koch, M. H. J., Seydel, U., Brandenburg, K. (2000). Thermotropic and lyotropic properties of long chain alkyl glycopyranosides. Part 1: monosaccharides headgroups, *Chemistry and Physics of Lipids*, **104**, 75–91.

Zhang, Z., Fukunaga, K., Sugimura, Y., Nkao, K., Shimizu, T. (1996). Synthesis of glycolipids: dialkyl-N-wN-(4-lactonamidobutyl) succinamoylx-L-glutamates, *Carbohydrate Research*, **290**, 225–232.

CHAPTER 3: EXPERIMENTAL DETAILS

3.0 Introduction

This chapter describes the device fabrication and experimental techniques used to study the structural and electrical properties of glycolipids. The device fabrications consist of substrate preparation and cleaning process. The experimental techniques used to study the structural properties of glycolipids were OPM, DSC, TGA, FTIR and XRD. Electrical properties of glycolipids were described in dielectric relaxation, conductivity and pyroelectricity studies.

Devices fabrication includes substrate preparation and proper cleaning processes. Subsequently, aluminium (Al) was deposited by thermal evaporation method as bottom and top electrodes. Solution and thin films preparation processes to fabricate metal-insulator-metal (MIM) devices are also described.

Structural properties of glycolipids have been investigated by several measurements such as OPM, DSC, TGA, FTIR and XRD. OPM has been used as a tool to investigate texture of glycolipids. Whereas DSC technique is used to investigate phase transition of glycolipids when they are heated or cooled. Subsequently, TGA measurement was conducted to study the thermal stability of glycolipids and FTIR technique has been used to investigate the functional groups present in glycolipids. Finally, XRD is employed to infer the crystal structure of the glycolipids.

Electrical properties of glycolipids have been studied in dielectric relaxation,

conductivity and pyroelectric measurements. The dielectric relaxation and conductivity properties were used to analyze polarization of glycolipids which can be induced by interfacial polarization or orientation of molecules. The pyroelectric property of glycolipids was used to describe potential application in infra-red sensor by its figure-of-merit. Dielectric spectroscopy or often called as impedance spectroscopy technique is used to measure the dielectric properties of a material as a function of frequency. The frequency range is from 10^{-2} to 10^7 Hz and the measurements were performed at several temperatures. Conductivity of glycolipids can be obtained after converting dielectric to conductivity via an equation, which is described in this chapter. Pyroelectricity of glycolipids has been investigated by the quasi-static method. In quasi-static method, the triangular waveform temperature is applied to the glycolipids thin film to produce the square waveform of short-circuited pyroelectric current. Several rates of change of temperature are set. The peak-to-peak pyroelectric current are recorded with respect to the changing rate of temperature. The short-circuited pyroelectric current of the glycolipid can be related to the rate of change of polarization.

3.1 Device fabrication

3.1.1 Substrate preparation

A device requires a substrate as a base for thin film deposition. Microscope glass slides were chosen as substrates because of good heat transfer. Furthermore, this characteristic of glass slides was important for pyroelectric investigation when a triangular waveform temperature were applied to the thin film.

Glass substrates were cut into 2 cm x 2 cm dimensions. The size of the glass substrate is chosen such that a shadow mask can be applied for aluminium thermal evaporation to fabricate the top and bottom electrodes. In preparing the glass substrate, goggles and gloves were used for safety purpose and to avoid any injury cause while cutting the glass. A diamond glass cutter was used to cut glass substrates to a specific size. A deep scratch line on the glass substrate was obtained. Subsequently, a homogeneous pressure is applied on the scratched glass substrates to split and remove the unwanted glass parts. Finally, the glass substrates were washed in a beaker containing soap.

3.1.2 Substrate cleaning process

During preparation, the glass substrates may have been contaminated. These contaminants could be dust particles, glass shreds or finger prints which occur along during the cutting process. These contaminants could result in errors during experimental data acquisition affecting the electrical properties of materials. Furthermore, inhomogeneous surface morphology could happen due to the existence of contaminants. Therefore, proper substrates cleaning process is necessary at the initial stage to avoid any unnecessary errors.

Initially, the glass substrates were soaked in a beaker which contained diluted Decon 90 cleaning detergent (ratio Decon detergent: deionized (DI) water = 1: 20) for 30 min to solute or remove some organic substances. Subsequently, the beaker was placed in an ultrasonic bath sonicator for 20 min to remove dust particles or any residues from the glass substrates. Subsequently, the glass substrates were agitated in DI water for three times to ensure all traces of contamination and cleaning solution have been removed. Then, the glass substrates were immersed in acetone and followed by

ethanol to ensure all organic substances have been fully doffed. Finally, the glass substrates were dried under nitrogen gas flow. The cleaned glass substrates were later kept in a container and stored in a dry cabinet.

3.1.3 Electrode deposition

Devices were fabricated using MIM structures. Al was used as top and bottom electrodes for conductive purpose to study electrical properties of materials. The Al wires of 99.999 % purity were purchased from Kurt J. Lesker Company. For the electrode deposition, Edward model A-360 Thermal Evaporator was used to evaporate Al in a 10K clean room environment. The thermal evaporator system is shown in Figure 3.1.



Figure3.1: Edward model A-360 Vacuum system with Thermal evaporator.

At the initial stage, Al wires were cut into length of 1 cm for thermal evaporation process. For the bottom electrode, 4 pieces of Al wires were used during the thermal deposition. Whereas for the top electrode, 3 pieces of Al wires were used in the deposition process. These Al wires (1 cm) were gripped on helical tungsten wire by

pliers and place at the evaporation source in the thermal evaporator. Then, the glass substrates were placed on the shadow mask inside the thermal evaporator.

A stage of about 12 cm height was required to increase the distance between the evaporation source and the shadow mask. It is because, if the shadow mask was too close to the evaporation source, it would melt the glass substrates or even burn the thin films during the thermal evaporation process. In addition, the stage also helps to reduce the penetration effect of Al particles into the thin films which can cause short-circuit. The shutter between the shadow mask and the evaporator source was shut prior to the evaporation process.

For the thermal evaporation process, high vacuum was required for the Al deposition. It would allow Al particles to travel and reach the substrate. Furthermore, high vacuum can also prevent oxidation process from occurring on the deposited-Al layer. In order to reach high vacuum, vacuum chamber was pumped for about 2 hours using a diffusion pump. When the pressure of the vacuum chamber has approached the value below 3.0×10^{-5} mbar, the evaporation process was started.

In order to melt the Al wires which were gripped on the helical tungsten wire, a current of 10 Ampere (A) was applied consistently onto the tungsten wires. When the Al wires melt, the current was abruptly increased to 24 A. At this stage, molten Al start to evaporate and vaporizes. Then, the shutter was opened for 1 min to allow Al particle to diffuse to the substrate and aggregates to yield a conductive electrode. After 1 min, the shutter was closed immediately, while the helical tungsten wire was kept heated for another 30 seconds to remove the Al residue. When all the processes

were completed, the current was reduced to zero. The vacuum chamber was allowed to cooled down for 30 min before the substrates were taken out from the chamber.

3.1.4 Thin films preparation

The glycolipid materials were prepared in a solution form. In order to prepare the glycolipid solutions, the glycolipid powders were weighted by an analytical balance (model GR-200 from AND). Subsequently, the weighted glycolipid powders were placed in sample containers and dissolved with ethanol to form solutions with 0.5 g/ml concentration. These sample containers were stirred in an ultrasonic bath sonicator at 60 °C for 40 min to ensure a homogeneous mixture.



Figure 3.2 : Laurell WS-650MZ-23NPP spin coater.

A spin coater from Laurell WS-650MZ-23NPP was then used to deposit thin films on the substrates as shown in Figure 3.2. This process was carried out in 10K clean room environment. Initially, the Al-deposited substrates were placed on the rotation platform of the spin coater. Subsequently, the dry pump was turned on to suck and hold the substrates. Then, the substrates were spinned one time to remove dust

particles. Subsequently, a micro-syringe from Hamilton was used to transfer the glycolipid solution of 250 μl on the Al-deposited substrate. After transferring the solution, the high speed rotation of 8000 rotations per min for 10 s was applied. This solution was spreaded by a centrifugal force on the Al-deposited substrate to produce glycolipid thin film. The glycolipid thin films were then kept in an oven at 80 $^{\circ}\text{C}$ for 2 hours to fully remove the residual solvent.

The top layer of the glycolipid thin films were deposited with Al electrode by the thermal evaporation technique as described in *Section 3.1.3*. It would yield MIM structure devices with four 2 mm x 2 mm active electrode area. Subsequently, silver conductive paint from Electrolube was used as electrical contacts with Al foil wires.

3.2 Structural properties of glycolipid

3.2.1 Optical Polarizer Microscopy (OPM)

An OPM is a technique used to polarize light in order to study the optical properties of samples. In this research, OPM was a transmitted light type and it was used to investigate the phase transformation of liquid crystals. Compared to a usual microscope, an OPM has additive units such as polarizer and analyzer. The polarizer is used to change natural light to linearly polarized light. Whereas the analyzer was adjusted, so that the direction of analyzer is orthogonal to the direction of the transmitted polarized light from the polarizer. Thus, the image formation was totally dark since no light can pass through the analyzer. Then, the sample was placed between polarizer and analyzer. The transmitted polarized light from the polarizer can

pass through the sample and reach the analyzer to perform a particular texture of liquid crystals. The OPM used is shown in Figure 3.3.



Figure 3.3: Optical Polarizer Microscopy.

The sample was placed on a microscope glass slide with a glass cover. The glass slide was set into hot-stage and placed on the stage of OPM. The hot-stage was controlled by Mettler Toledo FP90 Central Processor. The temperature was started from room temperature to a clearing point of the sample (before decomposition process) at temperature rate of 5 °C/min. Subsequently, the sample was cooled down from the clearing point to room temperature at temperature rate of -5 °C/min. It would form a temperature loop. The temperature loop was performed in 3 cycles to get a better texture of the liquid crystals. Each texture of the liquid crystals at various temperatures were captured by ColorView XS Soft Imaging System which was

connected to a computer.

3.2.2 Differential Scanning Calorimetry (DSC)

DSC is a technique used to investigate phase transitions of liquid crystals when they are heated or cooled. In a controlled environment, DSC is used to measure the heat flow in liquid crystals which is due to phase transition. The heat flow of liquid crystals is observed as a function of time and temperature. This technique includes endothermic process, exothermic process or change in heat capacity which can characterize some changes in the physical or chemical properties of liquid crystals. A picture of DSC is shown in Figure 3.4.



Figure 3.4: Differential Scanning Calorimetry.

The pan used for the DSC measurement was a standard pan since the material was a solid sample. Before the measurement, the material was weighted by an analytical balance between 5 to 10 mg. After the sample was weighted, the sample and holder were placed together into a press kit which was sealed by a hermetic pan by a gentle

press. Another empty standard pan was also sealed with the hermetic pan as a reference pan.

In DSC instrument, there are two specific positions in the sample chamber which allow the pans to be placed as shown in Figure 3.5. In the sample position, the sample pan is placed on it. Meanwhile, in the reference position the empty pan was placed on it. The sample chamber is enclosed by a lid. The nitrogen gas is turned on and controlled between 0.1 to 0.2 bar. The cooling system is turned on. The DSC instrument is connected and controlled by a computer. The temperature is initially set at -50 °C. It will increase the crystallinity of the material. The temperature is ended up at 250 °C before the material decomposes. The heat rate is set at a moderate rate, 10 °C per minute to avoid noise and error which exist during the experiment. The heat rate is supplied consistently to both pans. One of the pans which consist of the material will gain more heat compared to the other reference pan. Meanwhile, the heater will detect and measure the amount of heat supplied to the material. Thus, this amount of heat at a certain temperature is known as heat capacity, C_p .

In DSC measurement, the melting and clearing point of liquid crystals can be obtained. If the liquid crystal has broad mesophases, it will exhibit enantiotropic phase transition between the two liquid crystal phases. For example, smectic A phase change to columnar phase during heating. However, not all phase transition can be detected by DSC measurement (e.g. cubic phase). Figure 3.6 illustrates the DSC plot of a liquid crystal.



Figure 3.5: Two specific positions in the sample chamber. S and R represent as sample and reference position respectively.

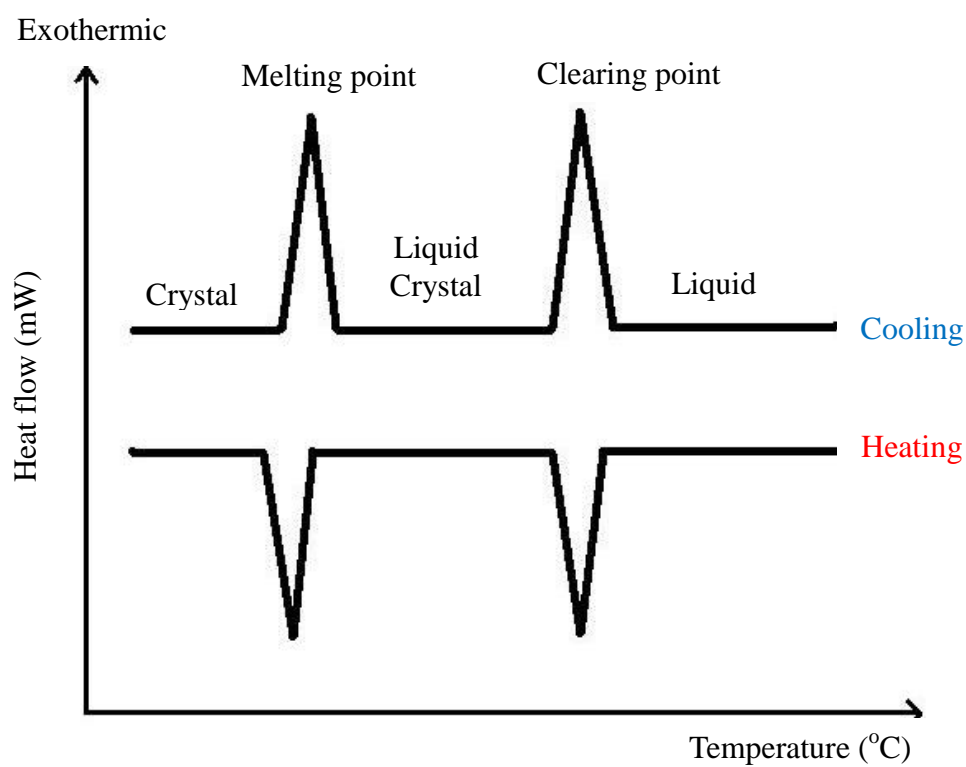


Figure 3.6: DSC plot of liquid crystal.

During the heating process, the peaks of melting, clearing point and enantiotropic phase transition that are showing downstream, are known as the endothermic peak. It is due to more energy is required for the molecules to increase the flexibility and even the structural alignment of the molecules during the phase transition process. Meanwhile, for the cooling process, the peaks of melting, clearing point and enantiotropic phase transitions are showing upstream as the exothermic peak. Thus, heat is being released from clearing point until melting point and becoming crystal. This liquid crystal transition is reversible.

3.2.3 Thermogravimetry (TGA)

TGA is an instrument used to study thermal stability of a material where the weighted substance is heated at a certain heating rate and measured as a function of temperature. In fact, TGA contains three basic devices which include furnace, precision balance and detector. The furnace has been programmed, so that the temperature is linearly increased with time. Then, the precision balance will measure the weight of substance and record by a detector (Cyril, 1969). The TGA is shown in Figure 3.7.

In initial stage, the sample is weighted by an analytical balance before being placed on the pan. The weight of the material is controlled in 5 to 10 mg, so that the decomposition time of the sample is shortened. The pan is flamed by a gas burner to remove any residue compounds before placing the weighted substance. The heating rate was set at 50 °C per min. Meanwhile, the temperature range starts from room temperature to 600 °C. During the heating process, the precision balance records the remainder of the mass. The percentage by mass can be calculated by dividing the remainder mass with the initial mass. The results obtained by the TGA are plotted in

two curves. One of the curves shows the plot of weight substance versus temperature. Meanwhile, the other curve illustrates the rate of weight loss as a function of temperature which is known as derivative thermogravimetry (DTG) curve.

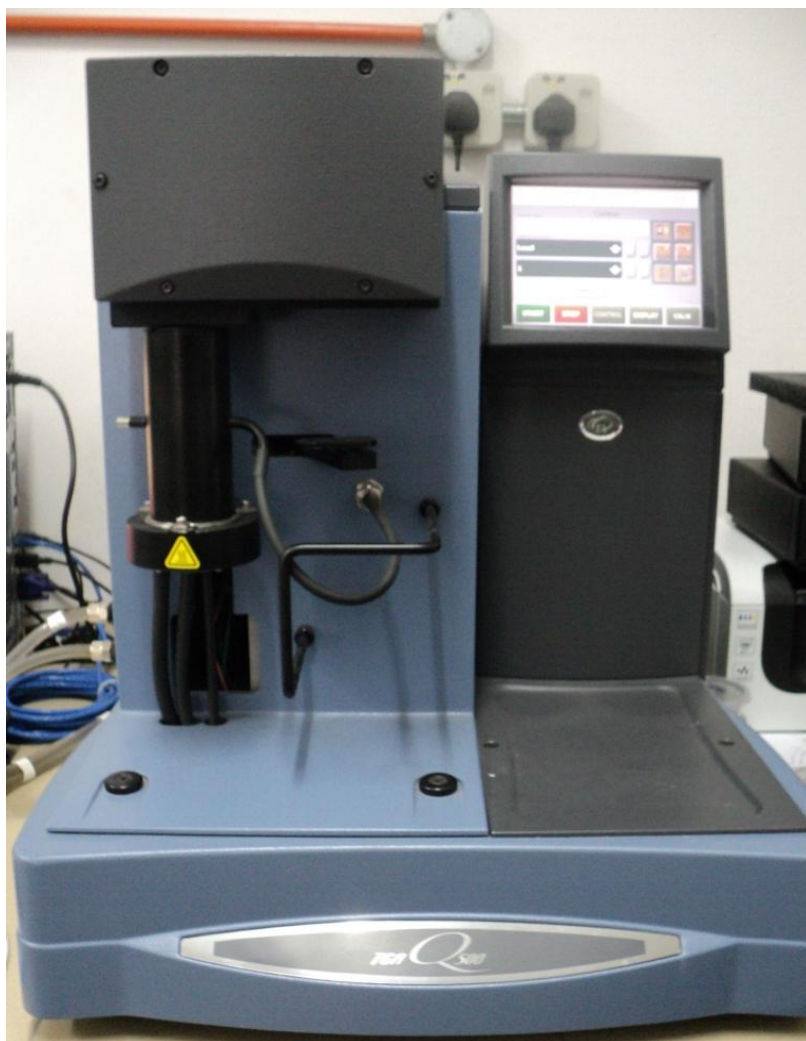


Figure 3.7: Thermogravimetry.

For those low molecular weight organic molecules, usually they will become stable at temperature below 100 to 200 °C. When the temperature is continuously increased to a certain high temperature, the organic molecules gain adequate energy to break the covalent bond between the linked atoms. Thus, the organic molecules are vaporized or even decomposed into small segments. At higher temperature (400 to 600 °C), thermal

cracking usually occurs in organic molecules. Therefore, significant degradation is expected. Some of the dissociation energy of single bonds characterized by Szycher (Szycher, 1999) are C-H (320-420 kJ/mol), C-C (260-400 kJ/mol), C-O (330 kJ/mol) and O-O (147 kJ/mol).

3.2.4 Fourier Transforms Infrared (FTIR) Spectroscopy

FTIR spectroscopy is a technique used to analyze the molecular vibration when a molecule is exposed to infrared (IR) radiation and absorb specific frequencies of IR. The functional group and symmetry of the molecule are common factors to determine the specific frequencies of IR which absorb by molecule. These specific frequencies can be verified as resonant frequencies. IR radiation frequencies are equivalent to the frequency of the molecular bond or functional group which vibrates. The FTIR spectroscopy instrument used is shown in Figure 3.8.



Figure 3.8: Fourier Transforms Infrared Spectroscopy.

The IR of the electromagnetic radiation can be partitioned into three regions, i.e. far-IR ($400\text{-}10\text{ cm}^{-1}$), middle-IR ($4000\text{-}400\text{ cm}^{-1}$) and near-IR ($14000\text{-}4000\text{ cm}^{-1}$) where the cm^{-1} is a unit known as wavenumber ($1/\text{wavelength}$). But, the infrared

spectroscopy is related to the electromagnetic spectrum in the frequency range from 4000-400 cm^{-1} to study the fundamental vibration and rotational-vibrational structure. In order to produce the FTIR spectrum, the sample is exposed to IR laser. If the IR sensor discovers that the detected signal is decreased compared to the initial IR signal, then some of the signal has been absorbed by the molecule. This change in the detected signal can be illustrated as a percentage of absorbed IR radiation as a function of wavenumber.


The FTIR spectroscopy is very valuable for analyzing organic compounds. Every organic compound has a unique FTIR spectrum which corresponds to their molecular structure. Therefore, every functional group vibrates at a specific frequency by absorbing the IR radiation. For example, hydroxyl group (O-H) of alcohols absorb IR radiation at wavenumber 3610-3670 cm^{-1} . It will induce the hydroxyl bond to stretch and contract between atoms at a range of bond length. If the intensity of the IR radiation increases at the same wavenumber, the amplitude of the oscillation between the atoms will also increase.

3.2.5 Profilometer

Surface profilometer is a technique to measure physical surface height with varies position of the platform. It also has a wide range of application such as measurement in an etched trench depth, surface roughness and 3 dimensional imaging of surfaces. That information is obtained by KLA Tencor P-6 Surface Profilometer which is shown in Figure 3.9. Inside the profilometer, the diamond stylus is controlled by a PC running Windows, move and contact over the thin films surface to measure the accurate height value. This instrument has high sensitivity in which the step height

can be measured down to a few nanometers. The profilometer measures the active area and thickness of the thin films to be used for further electrical analysis for dielectric and pyroelectric properties.

Table 1: Scanning parameters of Surface Profilometer.

Scan type	Two dimensional (2D)
X Scan size	2000 μm
Scan speed	200 $\mu\text{m/s}$
Sampling rate	200 Hz
Multi scan average	1
Applied forced	0.50 mg
Range/resolution	327 $\mu\text{m}/0.1953\text{\AA}$
Profile type	

Initially, the sample (a thin film on glass substrate) is placed at the centre of platform inside profilometer. Then, the stylus is lowered to the surface of thin film. The scanning parameters of the profilometer which is tabulated in Table 1 are set. The software program is then run to control the stylus trace with 0.5 mg scanning force on the sample. Finally, the variation height value of the stylus is collected and illustrated in a graph. From the graph, thickness of the thin film is calculated by further analysis. The active area can be determined by the scan length of stylus. All the measurements were done under atmospheric condition.



Figure 3.9: KLA Tencor P-6 Surface Profilometer.

3.2.6 X-ray Diffraction (XRD)

XRD measurement is a technique to reveal formation about the crystal structure such as average spacing between layers of atom, the orientation of single crystal or shape of small crystalline regions. This technique moves the sample and detector in a circular direction to measure the diffracted intensity of x-ray beam as a function of incident and diffracted angle. XRD measurement usually is an indirect method. Thus, an inference is required to analyze the XRD spectra in order to acquire useful information.

The x-ray diffractometer basic setup includes detector, radiation source and samples. Usually, the radiation source uses copper as a target material. Other than that, molybdenum, chromium and iron can also be used as a target material to provide the specific wavelength. In order to generate x-ray beam, an electron is accelerated with

high energy to bombard the target material and releases the inner orbital electron from the target material. The vacancy of an inner orbital will be replaced by an electron from an outer orbital. Thus, x-ray is emitted from the target material. This x-ray beam is used as a tool to analyze the structural of substance because the magnitude of an atomic distance is almost equal to the wavelength of x-ray. Thus, x-ray will be diffracted after radiates on a sample at an angle. The diffraction of x-ray is collected by a detector and is plotted as a function of 2θ angle. Then, the diffracted x-ray is analyzed according to Bragg's Law

$$n\lambda = 2d \sin \theta \quad \text{Equation 3.1}$$

where λ is the wavelength of radiation, θ is the diffraction angle and d is the lattice spacing of sample.



Figure 3.10: X-ray diffraction.

The XRD instrument used for this investigation was Siemens D5000 X-Ray Diffractometer. This XRD equipment used a monochromatic x-ray radiation to measure lattice spacing in crystals by scanning sample in orbital with 2θ angle. The radiation source of this XRD is from copper k-alpha with a wavelength of 1.5418 Å. The D5000 XRD is shown in Figure 3.10.

3.3 Electrical properties of glycolipid

3.3.1 Dielectric constant and relaxation measurements

The dielectric measurements were carried out in a wide frequency range from 10^{-2} Hz to 10^7 Hz by using two different dielectric spectroscopy instruments. One of the instruments is a laboratory-made dielectric spectrometer (Furukawa et al, 1985) which covers the lower frequency range from 10^{-2} Hz – 10^4 Hz. Another instrument was purchased from Agilent. The model 4294A Impedance Analyzer together with 16047E test fixture can cover higher frequency range from 10^2 Hz – 10^7 Hz. The laboratory-made dielectric spectrometer and 4294A Impedance Analyzer are shown in Figures 3.11 and 3.12 respectively.

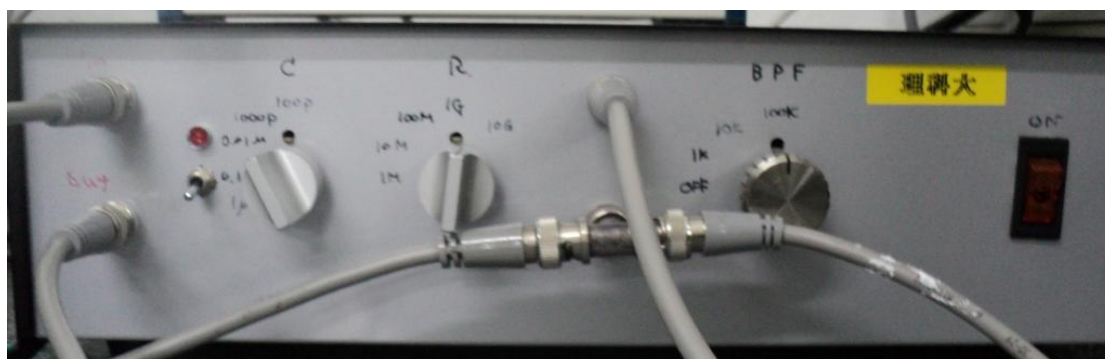


Figure 3.11: Laboratory-made dielectric spectrometer.



Figure 3.12: Agilent with model 4294A Impedance Analyzer.

The dielectric measurements were also carried out by varying the temperature between 30 °C – 190 °C on a hot chuck which was controlled by STC200 temperature controller. This temperature controller was used to heat and cool the samples to make a loop on the temperature measurement. The measurements were performed in two different conditions, which were in ambient and controlled environments. For ambient environment, sample was exposed to air without any protection shield. Whereas, for the controlled environment, the sample is placed in a chamber and the nitrogen gas is filled in to remove any air and moisture.

From the dielectric measurements, the parallel mode of capacitance, C_p and loss tangent, D were determined. This parallel mode capacitance was selected to fit in the small capacitors. In order to differentiate the extent of capacitors, usually large capacitors used were more than 100 μF , whereas small capacitors were considered as 10 μF and below. These results can be used to calculate the dielectric constant, ϵ' and dielectric loss, ϵ'' as a function of frequency by using Equations 2.1 and 2.2.

3.3.2 Conductivity measurements

The conductivity of the sample was carried out in a broad frequency range from 10^{-2} Hz until 10^7 Hz by using a laboratory-made dielectric spectrometer and HP4294A Impedance Analyzer. The sample was applied a loop temperature between 30 °C to 190 °C which were below the clearing point. Each step temperatures, either heating or cooling cycle were hold for 30 min until the temperature became steady. The cooling process below 100 °C would take longer time to reach a stable step temperature. Conductivity in two different conditions was then determined; those were ambient and controlled environments.

The conductivity of sample was determined from dielectric measurement. The complex conductivity was calculated by converting complex permittivity using equation as shown below:

$$\sigma^* = i\omega\epsilon_o\epsilon^* \quad \text{Equation 3.2}$$

with real component, $\sigma' = \omega\epsilon_o\epsilon''$ Equation 3.3

and imaginary component, $\sigma'' = i\omega\epsilon_o\epsilon'$ Equation 3.4

where f = frequency

σ^* = complex conductivity

σ' = real component of conductivity

σ'' = imaginary component of conductivity

ϵ^* = complex permittivity

ϵ_o = absolute permittivity of free space ($8.8542 \times 10^{-12} \text{ Fm}^{-1}$)

ω = angular frequency = $2\pi f$

3.3.3 Pyroelectric measurements

Quasi-static pyroelectric measurement was used in this research to study the pyroelectric properties of the glycolipid thin films. This technique was demonstrated by C. Dias, et.al. which can acquire accurate study of the pyroelectric coefficient (Dias et.al., 1993). The short-circuited pyroelectric current of the glycolipid thin films, can be exhibited by the rate of change of polarization as shown in the equation below:

$$I_p = pA \frac{dT}{dt} \quad \text{Equation 3.5}$$

where I_p is the peak-to-peak pyroelectric current, p is the pyroelectric coefficient, A is the effective area of the sample and dT/dt is the rate of temperature change.

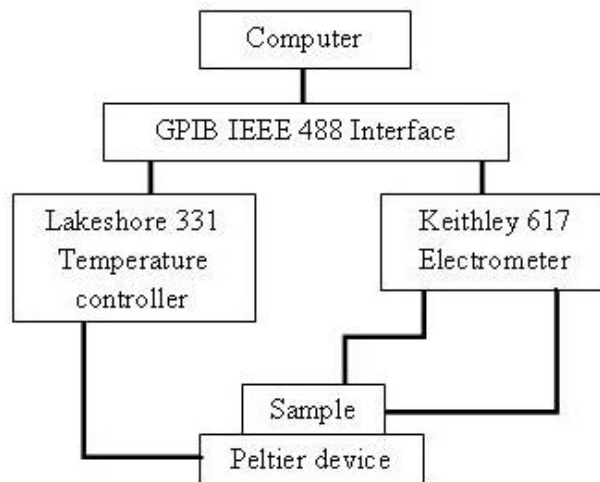


Figure 3.13: Experimental setup for pyroelectric measurement.

A peltier device was used to heat the sample. Meanwhile, this device is managed by a Lakeshore 331 temperature controller. This temperature controller generates a triangular waveform of temperature modulation with temperature range from 30 °C to 31 °C with several changing rate. These rates of change were 0.01 °C s⁻¹, 0.02 °C s⁻¹, 0.03 °C s⁻¹, 0.04 °C s⁻¹ and 0.05 °C s⁻¹. The peak-to-peak pyroelectric current was determined by using a Keithley 617 electrometer. Furthermore, to record the data,

both electrometer and temperature controller were connected to a computer by the GPIB IEEE 488 Interface. The schematic diagram of the experimental setup for the pyroelectric measurement is shown in Figure 3.13.

3.4 Summary

This chapter depicts the device fabrication and experimental methods used to investigate the structural and electrical properties of glycolipids. The device had MIM structure where the spin-coated thin film was sandwiched between Al electrodes. The OPM was used to study the phase transformation and texture of liquid crystals. The DSC was used to investigate the phase transition temperature of liquid crystals. Subsequently, the TGA in this research was used to study the thermal stability of glycolipid compounds as a function of temperature. The FTIR spectroscopy was used to analyze the molecular vibration when a molecule absorbs specific frequencies after explosion of infrared. The surface profilometer was used to measure the thickness of the spin-coated thin film and the active area of the device. Then, the XRD was used to analyze the ordered structure such as spacing between layers of atom. Furthermore, the dielectric measurements were carried out by a laboratory-made dielectric spectrometer (10^{-2} Hz – 10^4 Hz) and 4294A Impedance Analyzer (10^2 Hz – 10^7 Hz) by varying the temperature between 30 °C – 190 °C on a hot chuck which was controlled by STC200 temperature controller. The conductivity of the sample was determined from dielectric measurement via Equation 3.2 ($\sigma^* = i\omega\epsilon_0\epsilon^*$). In addition, the quasi-static pyroelectric measurement was used to study the pyroelectric properties of the glycolipids by applying triangular waveform of temperature with several ramping rate.

References

Cyril, K., (1969). An introduction to thermogravimetry. Heyden & Son Ltd, Great Britain, pg 1-23.

Dias, C., Simon, M., Quad, R., Das-Gupta, D. K. (1993). Measurement of the pyroelectric coefficient in composites using a temperature-modulated excitation. *Journal of Physics D: Applied Physics*, **26**, 106-113.

Furukawa, T., Date, M., Ishida, K., Ikeda, Y. (1985). Computer-controlled apparatus for measuring complex elastic, dielectric, and piezoelectric constants of polymer films. *Review of Scientific Instruments*, **57**(2), 285-292.

Szycher, M., (1999). Szycher's Handbook of Polyurethane. CRC Press LLC. Chapter 2, pg 1-17.

CHAPTER 4: STRUCTURAL CHARACTERIZATION OF GLYCOLIPID THIN FILMS

4.0 Introduction

This chapter describes the structural study of the glycolipids Malto-C8C4, Malto-C12C8 and Malto-C14C10. The structural study includes the optical OPM, DSC, TGA, FTIR spectroscopy and XRD.

Sections 4.1 and 4.2 describe the OPM and DSC of the glycolipid compounds, respectively. The OPM study was used to identify the phase transition and the texture of the liquid crystalline state of the thin film. The DSC measurement was utilized to identify the melting point, phase transition temperature and clearing point of the glycolipid compounds.

The next section describes the TGA of the glycolipid compounds. The TGA measurements were carried out to study the thermal stability of the glycolipid compounds. The derivative weight percentage was used to determine the temperature of the decomposition.

Section 4.4 illustrates the FTIR spectroscopy of the glycolipid compounds. This FTIR spectroscopy was used to determine the functional groups that are present in the compounds by the specific wavenumber.

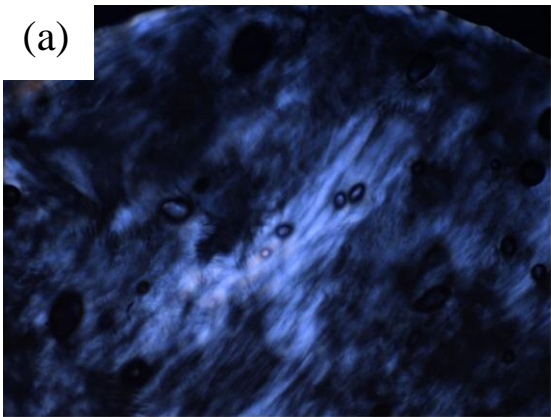
The final section illustrates the XRD pattern of the glycolipid compounds. The XRD

was used to infer the structural arrangement of the compounds based on the prominent peaks which can be observed in the XRD pattern.

4.1 Optical Polarizer Microscopy (OPM)

Table 4.1 shows the optical observation of phase morphologies of Malto-C8C4 upon heating with a polarizing microscope. The texture observed at 27.2 °C exhibits a liquid crystalline phase which indicated as smectic A (Liao et. al., 2006; Gerbera et. al., 2009). The same texture of phase morphology can be observed when the temperature is increased to 100.0 °C. At 190 °C, the texture of the sample as shown by the optical microscope shows dark field indicating fluid behaviour. Thus the phase is identified as isotropic. The OPM observations show that, there exists only one phase in Malto-C8C4 which is smectic A.

Table 4.1: Optical texture of Malto-C8C4 as observed with a polarizing microscope at 10 °C min⁻¹ heating rate.

Texture of liquid crystal	Temperature, °C	Phase of liquid crystal
(a) 	27.2	Smectic A

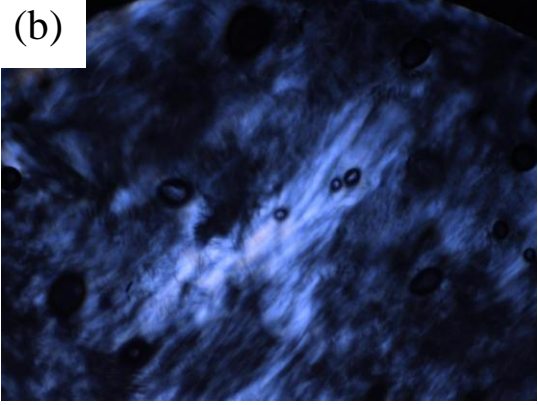
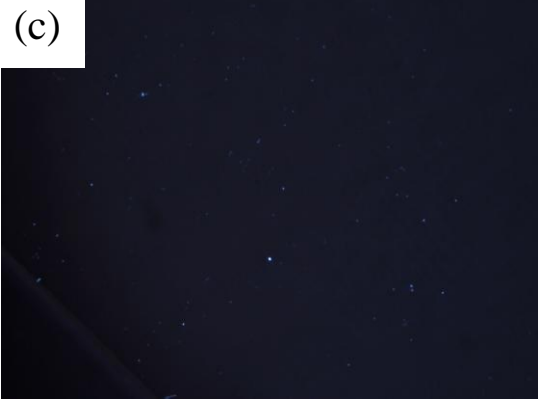
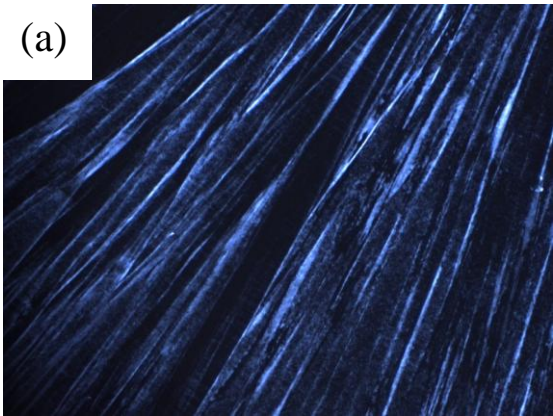
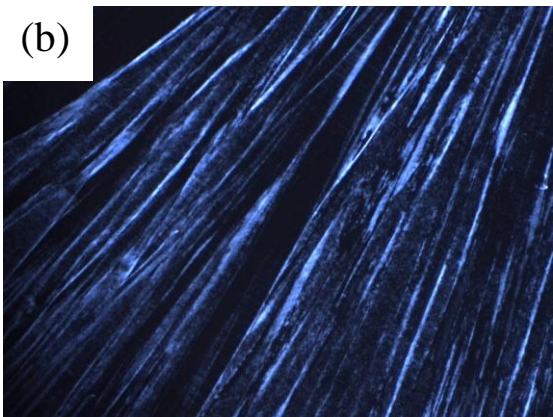

<p>(b)</p> 	<p>100.0</p>	<p>Smectic A</p>
<p>(c)</p> 	<p>190.0</p>	<p>Isotropic</p>

Table 4.2 illustrates the optical observation of phase morphologies of Malto-C12C8 upon heating as obtained from a polarizing microscope. The texture observed at 26.6 °C shows a liquid crystalline phase which indicates the phase as smectic A (Liao et. al., 2006; Gerbera et. al., 2009). Similar texture of phase morphology can be observed when the temperature is increased to 90.0 °C. Subsequently, the optical microscope shows a dark field when the temperature is raised to 120 °C. This dark field is stiff and non-fluid behaviour and is identified as cubic phase (Hashim et. al., 2006). At 198 °C, the optical microscope also exhibits a dark field and shows fluid behaviour. This is known as isotropic phase. The OPM observations show that, there exist two liquid crystalline phases in Malto-C12C8 that is smectic A and cubic phase.

Table 4.2: Optical texture of Malto-C12C8 as observed with a polarizing microscope at 10 °C min⁻¹ heating rate.

Texture of liquid crystal	Temperature, °C	Phase of liquid crystal
<p>(a)</p> 	26.6	Smectic A
<p>(b)</p> 	90.0	Smectic A
<p>(c)</p> 	120.0	Cubic

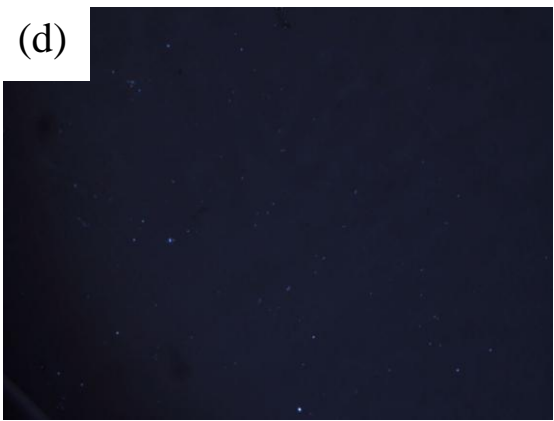
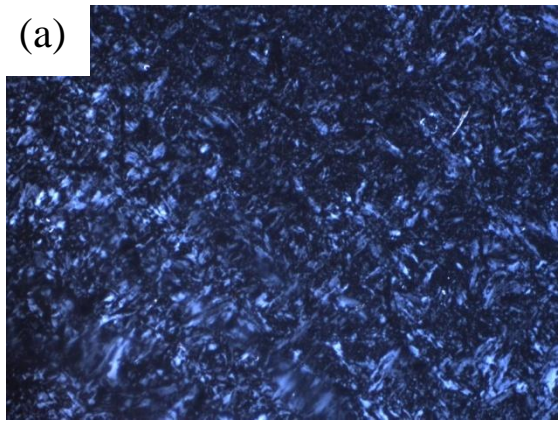
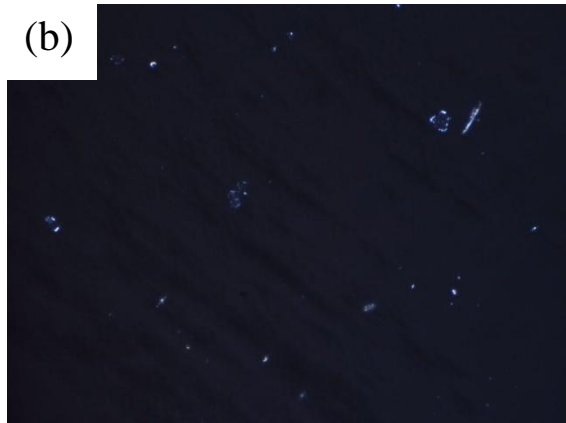
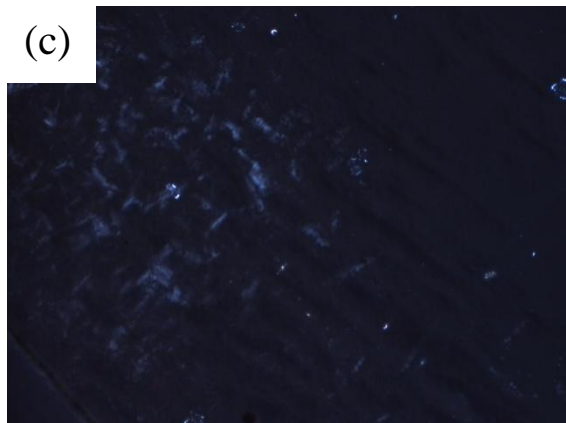
<div data-bbox="244 197 799 616"> <div data-bbox="244 197 331 280">(d)</div>  </div>	198.0	Isotropic
---	-------	-----------

Table 4.3 shows the optical observation with a polarizing microscope of phase morphologies of Malto-C14C10 upon heating. The texture observed at 30.0 °C shows a liquid crystalline phase identified as smectic A (Liao et. al., 2006; Gerbera et. al., 2009). Subsequently, the optical microscope shows a dark field which is rigid and exhibit non-fluid behaviour when the temperature is raised to 78.0 °C. The phase is identified as cubic phase (Hashim et. al., 2006). At 135.0 °C, the optical microscope exhibits another liquid crystalline texture which is known as columnar phase (Hashim et. al., 2006). At 218.0 °C, the columnar texture is observed and shown in Table 4.3 (c). Further increase in temperature to 237 °C cause the optical microscope to exhibit dark field which indicate fluid behaviour. The phase is known as isotropic phase. The OPM observations show that, there exist three liquid crystalline phases in Malto-C14C10 which is smectic A, cubic and columnar phase. Table 4.4 shows the molecular structure of the maltosides glycolipid and their transitions based on the OPM observations.

Table 4.3: Optical texture of Malto-C14C10 as observed with a polarizing microscope at 10 °C min⁻¹ heating rate.

Texture of liquid crystal	Temperature, °C	Phase of liquid crystal
<p>(a)</p> 	30.0	Smectic A
<p>(b)</p> 	78.0	Cubic
<p>(c)</p> 	135.0	Columnar (start appear)

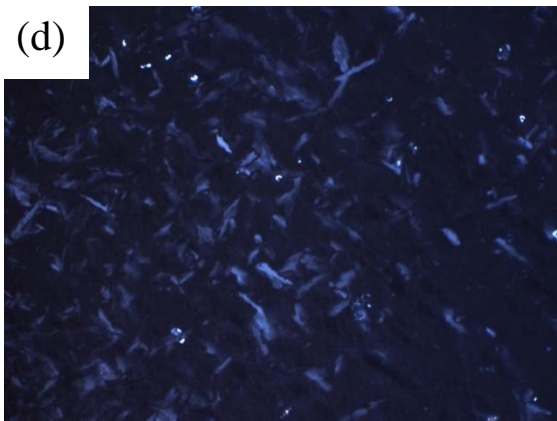
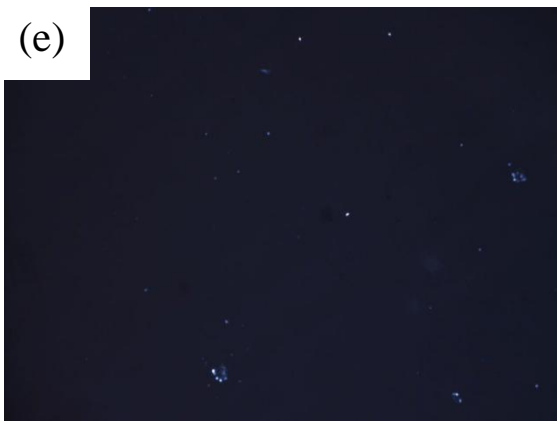
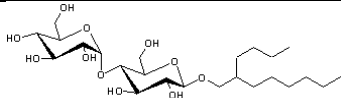
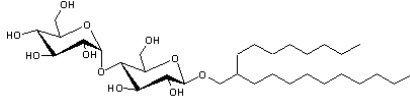
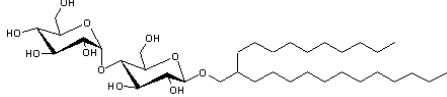
(d)		218.0	Columnar
(e)		237.0	Isotropic

Table 4.4: The molecular structures of the maltosides and their phase transitions based on OPM observation at $10\text{ }^{\circ}\text{C min}^{-1}$ heating rate.

Compound	Molecular structure	Phase transition ($^{\circ}\text{C}$)				
Malto-C8C4		Cr	<23	SmA	190	I
Malto-C12C8		Cr	<23	SmA	120	Q 198 I
Malto-C14C10		Cr	<23	SmA	78	Q 135 Col 237 I

(Cr = crystalline, SmA = smectic A, Q = cubic, Col = columnar and I = isotropic)

4.2 Differential Scanning Calorimetry (DSC)

Figure 4.1 exhibits the DSC curves of Malto-C8C4, Malto-C12C8 and Malto-C14C10 at $10\text{ }^{\circ}\text{C min}^{-1}$ heating rate. For Malto-C8C4 (black line), it can be observed that there exist two endothermic peaks in the heating run. The first peak is attributed to the melting point at $25\text{ }^{\circ}\text{C}$, so that molecules are self-assembled into lamellar liquid crystalline which is known as smectic A phase. The second peak is due to the clearing point at $183\text{ }^{\circ}\text{C}$ (Hashim et. al., 2012). This temperature, $183\text{ }^{\circ}\text{C}$, the arrangement of molecules is in non-ordered structure and move randomly like a liquid. This is known as isotropic phase.

For Malto-C12C8 (red line), it can be observed that two endothermic peaks exist in the heating run. The first peak is due to the melting point at $25\text{ }^{\circ}\text{C}$ where the molecules are self-arranged into smectic A phase. The second peak is known as clearing point at $209\text{ }^{\circ}\text{C}$ and the arrangement of molecules from cubic phase turns to isotropic phase. From the DSC measurements, the formations of cubic phase from smectic A phase cannot be detected probably due to a very small change in enthalpy. The change in enthalpy indicating the existence of the cubic phase is also undetected, even though the derivative of heat flow has been calculated.

For the Malto-C14C10 (blue line), it can be observed that there are three endothermic peaks in the heating run. The first peak is due to the melting point at $25\text{ }^{\circ}\text{C}$ where the molecules are self-organized into the smectic A phase. The second peak is due to the formation of columnar phase from cubic phase at $145\text{ }^{\circ}\text{C}$. The third peak is known as clearing point at $232\text{ }^{\circ}\text{C}$ where the arrangement of molecules from cubic phase changes to isotropic phase. In addition, the change of enthalpy is small in DSC

measurement, thus formation of cubic phase from smectic A phase cannot be detected, even through used the derivative of heat flow. Among these maltoside glycolipids, the length of the branched alkyl chain will cause more liquid crystalline phase to exist and thus produce interdigitated effect. Furthermore, the clearing point of maltoside glycolipids is shifted to higher temperature when longer length of the branched alkyl chain was used. In addition, the endothermic peaks of the DSC observations are in accordance to the texture observation in the OPM measurement except for the existence of cubic phase. The Table 4.5 shows the molecular structure of the maltosides glycolipid and their transitions based on the DSC measurement.

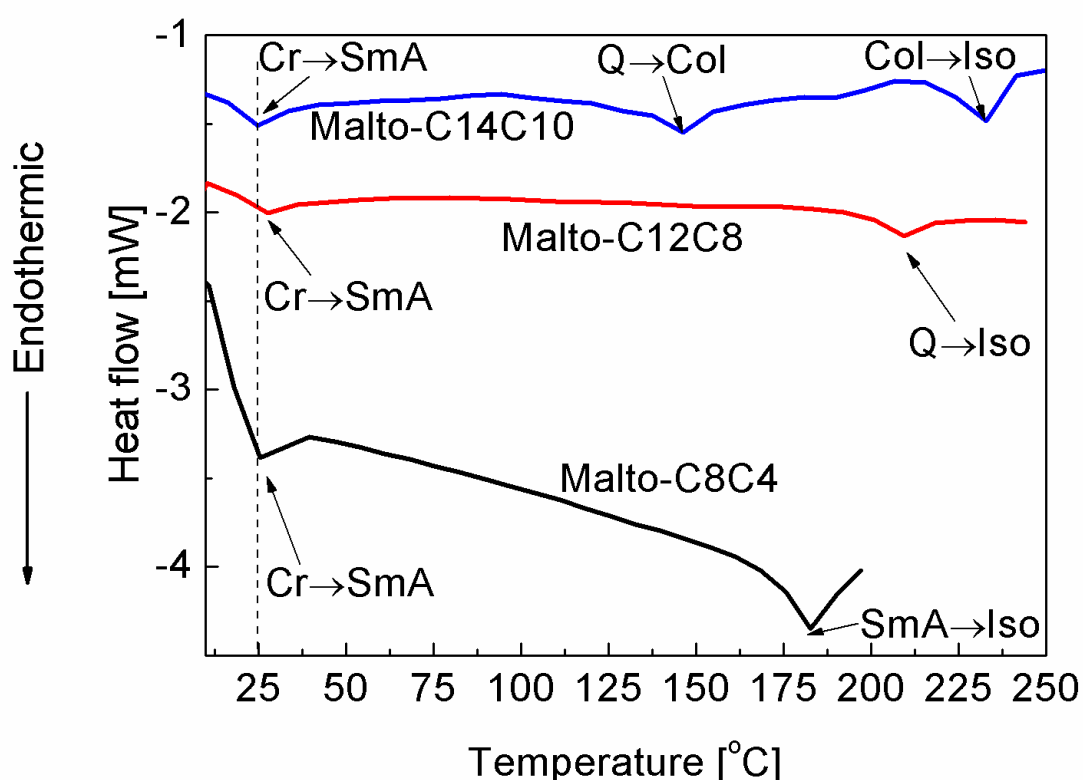
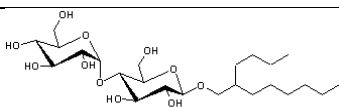
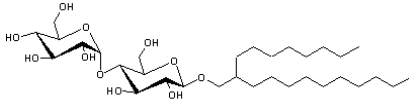
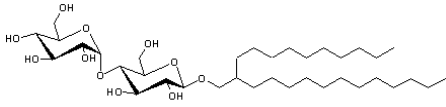


Figure 4.1: DSC curves of Malto-C8C4, Malto-C12C8 and Malto-C14C10 at 10 °C min⁻¹ heating rate.

Table 4.5: The molecular structures of the maltosides and their phase transitions based on DSC measurement at 10 °C min⁻¹ heating rate.

Compound	Molecular structure	Phase transition (°C)
Malto-C8C4		Cr <25 SmA 183 I
Malto-C12C8		Cr <25 SmA ? Q 209 I
Malto-C14C10		Cr <25 SmA? Q 145 Col 232 I

(Cr = crystalline, SmA = smectic A, Q = cubic, Col = columnar and I = isotropic)

4.3 Thermogravimetry (TGA)

The maltoside glycolipids (about 3 mg) were tested in a TGA at a heating rate of 50 °C min⁻¹ from room temperature to 650 °C under nitrogen gas flow. TGA can provide the temperature at which thermal stability of the glycolipid compounds can be achieved. Several steps of degradation stages were observed in the TGA measurement for these three glycolipid compounds. Figure 4.2 exhibits the TGA measurement of Malto-C8C4. Malto-C8C4 was stable up to 200 °C and experienced rapid weight loss at ~200 °C to 400 °C. An initial stage of weight loss starts at 200 °C to 250 °C. This is due to the dehydration of Malto-C8C4. Subsequently, the rapid weight loss starts at about 250 °C until 400 °C. This is due to the decomposition of Malto-C8C4 within the polar sugar head group and apolar branched alkyl chain group.

Figure 4.3 shows the TGA measurement of Malto-C12C8. The Malto-C12C8 was stable up to ~300 °C and rapid weight loss starts at ~300 °C until 400 °C. The dehydration process is not observed in Malto-C12C8. The result is an unexpected

since the polar sugar head group is supposed to attract water molecules from moisture easily. It can be explained due to the structure of Malto-C12C8 where the ratio between polar group and apolar group is almost the same. Thus, less water molecules can be attracted to Malto-C12C8. Subsequently, the rapid weight loss starts at about 300 °C until 400 °C. At this temperature, the decomposition of Malto-C12C8 is due to the decomposition of the polar sugar head group and apolar branched alkyl chain group upon the heating run.

Figure 4.4 illustrates the TGA measurement of Malto-C14C10. Malto-C14C10 was stable up to ~200 °C and experience a rapid weight loss at ~200 °C to 400 °C. The initial stage of weight loss occurs at 200 °C until 300 °C. This is due to the dehydration of Malto-C14C10. Consequently, the rapid weight loss starts at about 300 °C to 400 °C. This is due to the decomposition of Malto-C14C10 where the polar sugar head group and apolar branched alkyl chain groups were decomposed.

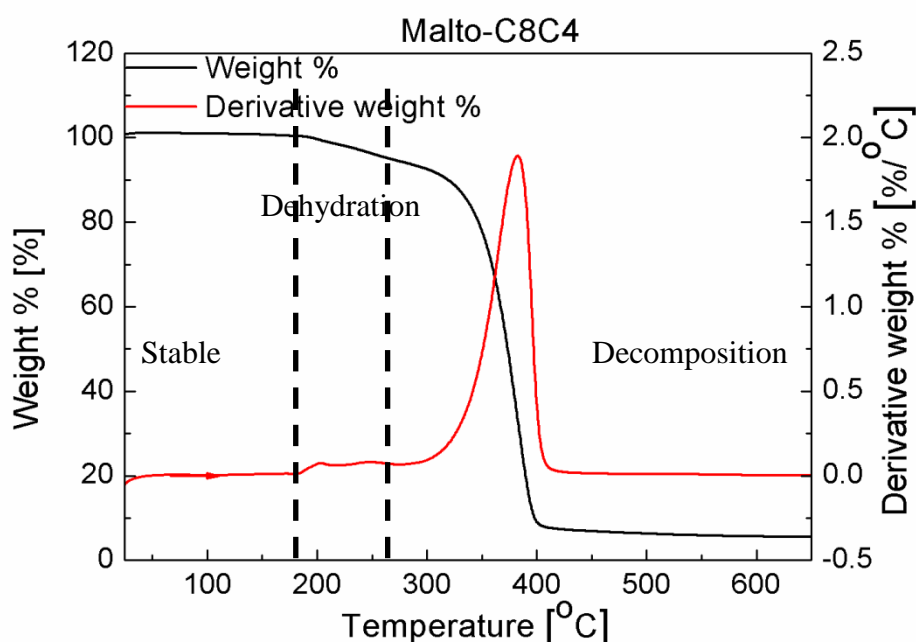


Figure 4.2: Weight % and derivative weight % curves versus temperature of Malto-C8C4.

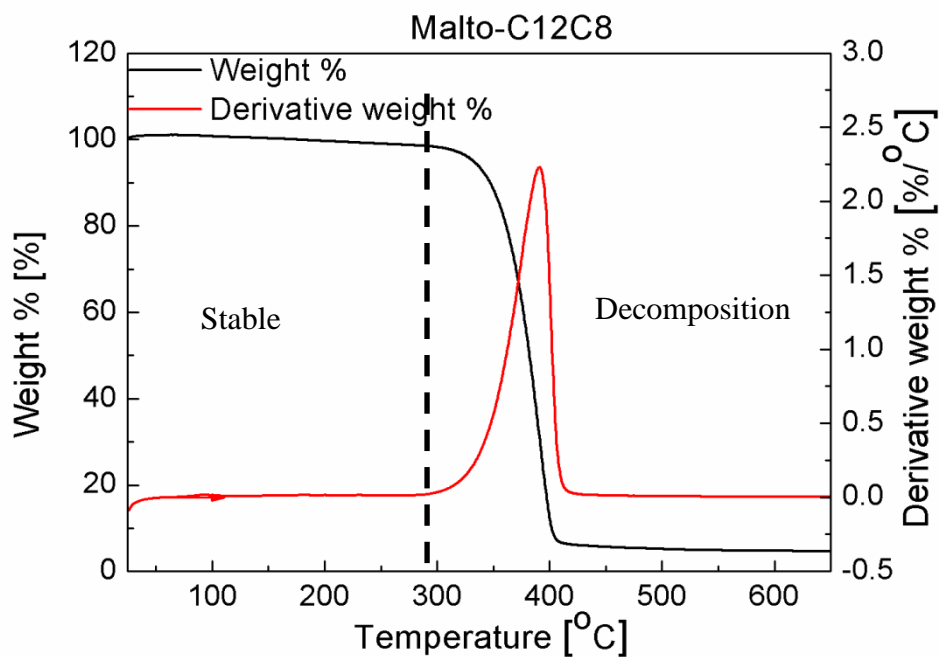


Figure 4.3 Weight % and derivative weight % curves versus temperature of Malto-C12C8.

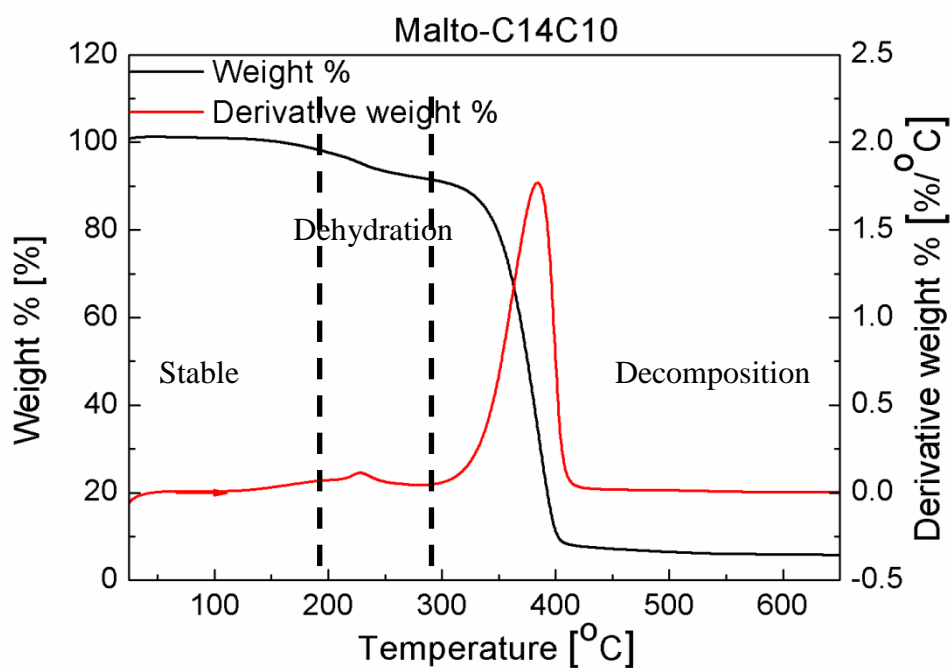


Figure 4.4: Weight % and derivative weight % curves versus temperature of Malto-C14C10.

4.4 Fourier Transforms Infrared (FTIR) Spectroscopy

Figure 4.5 exhibits the spectra of glycolipid Malto-C8C4, Malto-C12C8 and Malto-C14C10. The infrared measurements were observed at wavenumber from 4000 cm^{-1} to 400 cm^{-1} at a resolution of 4 cm^{-1} . From the spectra of the glycolipid compounds, the broad peak of medium intensity occur at around $3400 - 3200\text{ cm}^{-1}$, indicating the presence of the O-H bond in the glycolipid compounds (Howe et. al., 2007). The peak observed at 2920 cm^{-1} and 2850 cm^{-1} is due to the $-\text{CH}-$ stretching. Then, the peak observed at 1710 cm^{-1} is due to the $\text{C}=\text{O}$ stretching. The $-\text{CH}_2-$ and $-\text{CH}_3$ bending peaks were observed at 1460 cm^{-1} and 1380 cm^{-1} , respectively (Garidel, 2002; Garidel et. al., 2008). The C-O stretching was located at around $1300\text{-}1000\text{ cm}^{-1}$. The peaks at 1270 cm^{-1} and 1150 cm^{-1} were related to the tertiary structure of the C-O. Subsequently, the peaks at 1070 cm^{-1} and 1030 cm^{-1} were identified to be originating from the primary structure of the C-O. The peaks observed in Figure 4.5 are in good agreement with that reported for general glycolipid by Kwong (Kwong et. al., 2010). Table 4.6 summaries the vibrational modes and its wavenumber for the three glycolipids.

Table 4.6: The vibrational modes and wavenumber of glycolipids Malto-C8C4, Malto-C12C8 and Malto-C14C10.

Modes of vibration	Wavenumber (cm^{-1})
O-H	3376
$-\text{CH}-$	2920, 2850
$\text{C}=\text{O}$	1710
$-\text{CH}_2-$	1460
$-\text{CH}_3$	1380
C-O	1270, 1150 (tertiary) 1070, 1030 (primary)

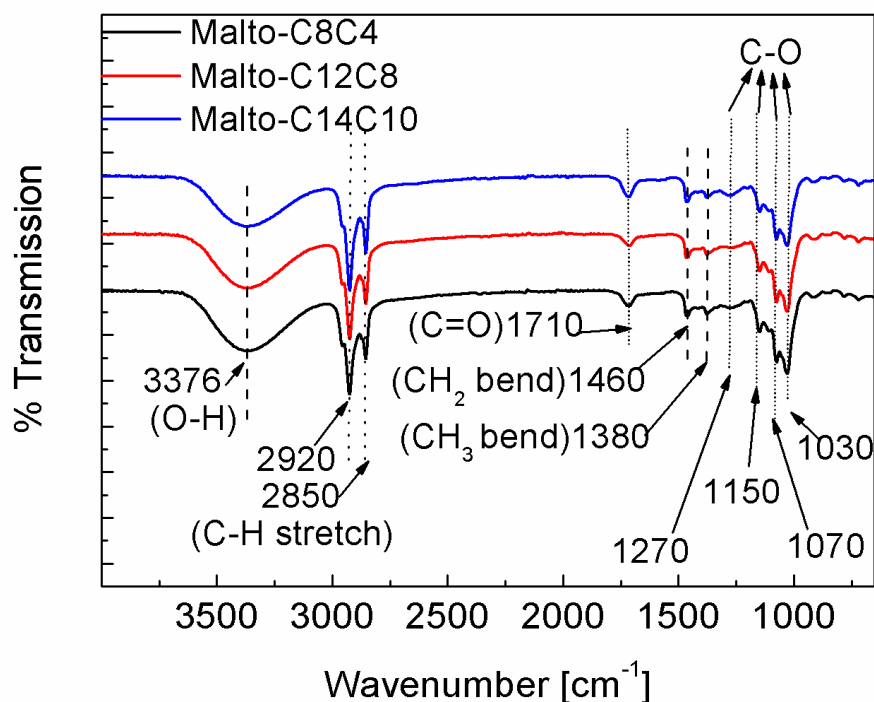


Figure 4.5: FTIR spectra of glycolipid Malto-C8C4, Malto-C12C8 and Malto-C14C10.

4.5 X-ray Diffraction (XRD)

Figure 4.6 illustrates the XRD profiles of glycolipid Malto-C8C4, Malto-C12C8 and Malto-C14C10 at room temperature. The glycolipid compounds were spin-casted onto a glass substrate for the XRD measurement. The scattering halos between 5° and 60° were observed. The diffraction pattern in Figure 4.6 shows broad peaks at approximately $2\theta = 20.06^\circ$ for all the glycolipid compounds. The broad peaks observed in XRD patterns were due to the amorphous structure of the glass substrate at room temperature. For the Malto-C12C8 and Malto-C14C10, no prominent peaks can be observed in their XRD pattern. It is due to the limitation of the XRD instrument which cannot be used to scan below $2\theta = 5^\circ$. For the Malto-C8C4, three prominent peaks at approximately 10.52° , 7.88° and 5.42° were observed in the XRD pattern. By using the Bragg's equation shown in Equation 4.1:

$$2d \sin\theta = n\lambda \quad \text{Equation 4.1}$$

where d = layer spacing,

θ = diffraction angle,

n = integer.

λ = wavelength of the x-ray source = 1.54 Å,

the layer spacing, d can be calculated according to each prominent peaks. A fully sketch Malto-C8C4 length is ~2.02 nm. The calculated d spacing is related to the layer of molecules which tilt at certain angle with respect to the normal line. Taking $n = 1$, the d spacing of the prominent peaks at 10.52°, 7.88° and 5.42° are 0.84 nm, 1.12 nm and 1.63 nm respectively as tabulated in Table 4.7. This is due to the molecules of Malto-C8C4 having formed three self-arranged ordered structures in liquid crystalline phase known as smectic A phase at room temperature. Usually, self-assembled molecules of glycolipid compounds are declined at a slight angle with respect to the normal line. But, Malto-C8C4 has the shortest branched alkyl chain length and thus the support coming from the branched alkyl chain will be the smallest. Thus, the molecules can lie down or declined at a large angle with respect to the normal direction and can be bonded with the glass substrate due to the hydrophilic nature of the glass substrate.

Table 4.7: The 2θ and d spacing of glycolipids Malto-C8C4 according to the prominent peaks of the XRD pattern.

$2\theta \pm 0.02 (^{\circ})$	$d \text{ spacing } \pm 0.02 \text{ (nm)}$
10.52	0.84
7.88	1.12
5.42	1.63

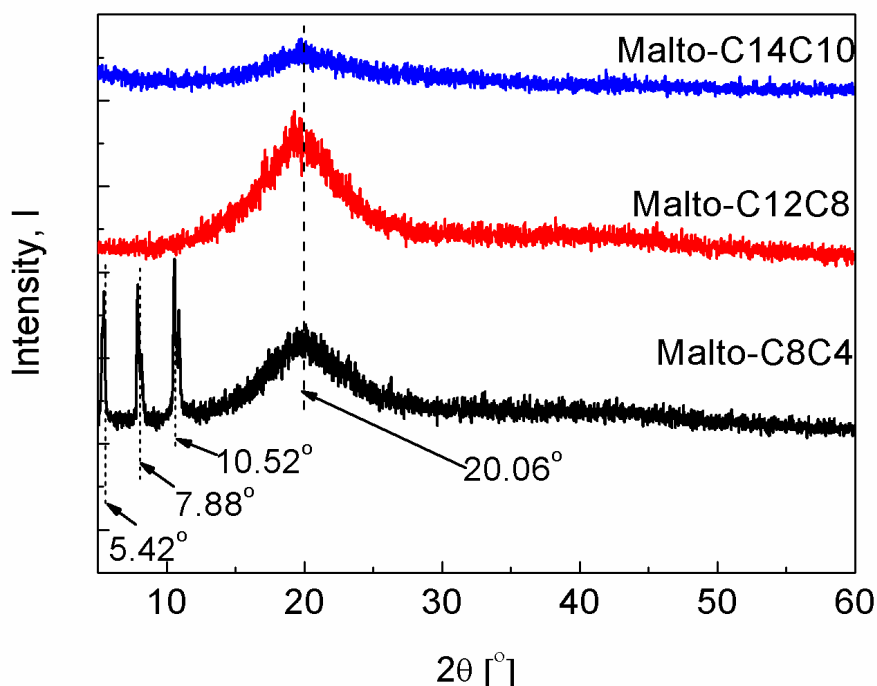


Figure 4.6: XRD profiles of glycolipid Malto-C8C4, Malto-C12C8 and Malto-C14C10 at room temperature.

4.6 Summary

The phase transition temperature obtained by the OPM and DSC measurements, the endothermic peaks of the DSC study agrees well with the observation in the OPM texture except for cubic phase of the Malto-C12C8 and Malto-C14C10. From the TGA measurement, the glycolipids compounds are stable upon heating up to temperature of 275 – 300 °C. The dehydration phenomena can be observed at ~ 200 °C (nearly clearing point) due to evaporation of water molecules contain inside the samples. This is because the sugar head group of glycolipid is strongly attracted to the water molecule and thus cause the water molecules not to evaporate easily at temperature below ~200 °C. When the temperature exceeds 300 °C, the glycolipid compounds start to decompose until 400 °C. The FTIR spectra verify that the

molecule structure of the glycolipid compounds contain functional groups of O–H, C–H, –CH₂–, –CH₃, C=O and C–O as determined by the specific wavenumber. From the XRD pattern, among the glycolipid compounds, the prominent peaks can be observed in the Malto-C8C4 only. It is probably due to the limitation of the XRD instrument which is insensitive at 2θ below 5°. These peaks determined three different *d* spacings of the Malto-C8C4. It means that Malto-C8C4 contains three self-assembled molecular structures. Malto-C8C4 has the shortest branched alkyl chain length and the support from the branched alkyl chain will be the smallest. As a result, the molecules can lie down or declined at a large angle with respect to the normal direction. The hydrophilic nature of the glass substrates also ensures that the Malto-C8C4 molecules are bonded to the glass.

References

- Garidel, P. (2002). Calorimetric and spectroscopic investigations of phytosphingosine ceramide membrane organisation. *Physical Chemistry Chemical Physics*, **4**, 1934–1942.
- Garidel, P., Howe, J., Milkereit, G., Rössle, M., Linser, S., Gerber, S., Willumeit, R., Gutschmann, T., Vill, V., Brandenburg, K. (2008). Structural polymorphism of hydrated ether-linked dimyristyl maltoside and melibioside. *Chemistry and Physics of Lipids*, **151**, 18-29.
- Gerbera, S., Wulfa, M., Milkereit, G. Vill, V., Howeb, J., Roesslec, M., Garideld, P., Gutschmannb, T., Brandenburgb, K. (2009). Phase diagrams of monoacylated amide-linked disaccharide glycolipids. *Chemistry and Physics of Lipids*, **158**, 118-130.
- Hashim, R., Hashim, H. H. A., Rodzi, N. Z. M., Hussen, R. S. D., Heidelberg, T. (2006). Branched chain glycosides: Enhanced diversity for phase behavior of easily accessible synthetic glycolipids. *Thin Solid Films*, **509**, 27-35.
- Hashim, R., Sugimura, A., Minamikawa, H., Heidelberg, T., (2012). Nature-like synthetic alkyl branched-chain glycolipids: a review on chemical structure and self-assembly properties. *Liquid Crystals*, **39** (1), 1-17.
- Howe, J., Minden, M., Gutschmann, T., Koch, M. H. J., Wulf, M., Gerber, S., Milkereit, G., Vill, V., Brandenburg, K. (2007). Structural preferences of dioleoyl glycolipids with mono- and disaccharide head groups. *Chemistry and Physics of Lipids*, **149**, 52-58.
- Kwong, W. L., Gan, W. C., Majid, W. H. A., Hashim, R., Heidelberg, T. (2010). Pyroelectric detection in glycolipid thin film. *Thin Solid Films*, **518**, 4412-4416.
- Liao, G., Zewe, S. K., Hagerty, J., Hashim, R., Abeygunaratne, S., Vill, V., Jákli, A., (2006). Thermotropic liquid crystalline properties of amphiphilic branched chain glycolipids. *Liquid Crystals*, **33**, 361-366.

CHAPTER 5: ELECTRICAL PROPERTIES OF GLYCOLIPID THIN FILMS

5.0 Introduction

This chapter describes the result of complex dielectric and conductivity of glycolipids. The spectra of the complex dielectric and conductivity were reproduced by the empirical function where several quantitative parameters have been determined. The pyroelectric effect of glycolipid compounds have been studied with respect to branched alkyl chain length. Furthermore, the diffusion process in glycolipids has also been described in this chapter.

The complex dielectric of glycolipid compounds (Malto-C8C4, Malto-C12C8 and Malto-C14C10) has been studied in a broad frequency range ($10^{-2} - 10^6$ Hz) by varying the temperatures throughout the heating and cooling processes. The spectra of the complex dielectric for the glycolipid compounds have been fitted by an empirical function. Those fitted quantitative parameters are used to analyze the dielectric polarization of the glycolipid compound. In addition, the dielectric constant at 100 Hz of glycolipid compounds has been extracted in order to study the phase transition behavior of these materials.

The complex conductivity of glycolipid compounds were investigated in the broaden frequency range ($10^{-2} - 10^6$ Hz). Each spectrum of glycolipid compound was obtained by varying the temperatures by heating and cooling process. The spectra of the complex conductivity for the glycolipid compounds were fitted and reproduced using

an empirical function. These fitted parameters were used to analyze the interfacial polarization and electrode polarization. The activation energy of each glycolipid compounds was also studied. The activation energy is used to depict the phase transition behaviour such as smectic A, cubic and columnar phase.

The pyroelectric effect of glycolipid compounds were investigated with several temperature ranges. The different length of branched alkyl chain will affect the order of the arrangement of molecules. The partial disorder arrangement of molecules will increases the net dipole moment in the thin films and contributes to higher pyroelectric coefficient. It is due to less cancellation of the dipole moment among the layers of molecules. In addition, the arrangement of molecules will affect the dielectric loss and the figure-of-merit of the device formed by the glycolipid thin films.

The diffusion process in cubic phase of Malto-C12C8 and Malto-C14C10 were also investigated. The formation of the cubic structure has enabled the trapping of charge carriers in the domain which contain the polar sugar head group. The charge carriers were diffused randomly around the polar sugar head group and can be modeled by the random walk scheme. From this model, the hydrogen bond lengths between the molecules were estimated. Furthermore, the charge carriers can also hop from one domain to another domain when a sufficient time is given. As a result, the hopping length is calculated which represents the bilayer molecular length.

5.1 Dielectric dispersion curves

5.1.1 Complex dielectric

Figure 5.1 shows the dielectric constant ε' and dielectric loss ε'' spectra for Malto-C8C4 at heating process (a) & (b) and cooling process (c) & (d) from 30 °C to 150 °C with 10 °C temperature step respectively. Both heating and cooling processes exhibit similar spectra pattern. The real component ε' exhibits two step increases with decreasing frequency. The first increase of ε' is at the high-frequency region (10^3 to 10^5 Hz) which is related to the dielectric relaxation. The second huge increase of ε' at the low-frequency region (below 10 Hz) is related to the dc conduction and electrode polarizations where the charges were accumulated near the electrode. Electrode polarizations were identified by the linear increase of the imaginary component ε'' with a gradient of -1 at the lower frequency (below 10 Hz), consequently induces the dc conduction.

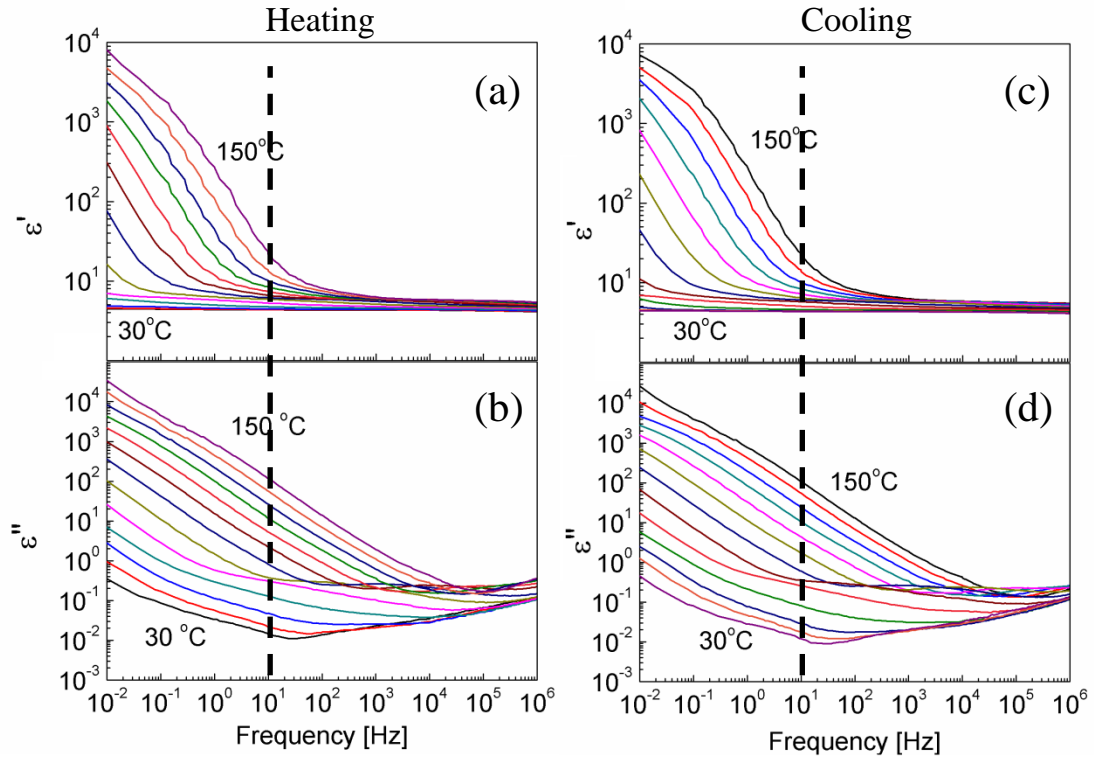


Figure 5.1: Dielectric constant ε' and dielectric loss ε'' spectra of Malto-C8C4 at heating-mode (a) & (b) and cooling-mode (c) & (d) from 30 °C – 150 °C with 10 °C temperature step.

Figure 5.2 exhibits the dielectric constant ϵ' and dielectric loss ϵ'' spectra for Malto-C12C8 at heating process (a) & (b) and cooling process (c) & (d) from 30 °C to 160 °C with 10 °C temperature step respectively. Both heating and cooling processes show approximately similar spectra pattern. The real component ϵ' exhibits three step increases with decreasing frequency. First increase of ϵ' is at the high-frequency region (10^4 Hz – 10^6 Hz) which is related to the dielectric relaxation. The second large increase of ϵ' at the intermediate-frequency range (10 Hz – 10^3 Hz), is due to the formation of heterogeneous structure where the charges were trapped at the domains. Whereas, the third huge increase of ϵ' is at the low-frequency region (below 10 Hz), is due to the accumulation of charges near the electrode. Furthermore, the imaginary component ϵ'' shows a linear increase with a gradient of -1 at the low-frequency region which is related to electrode polarization. Electrode polarization will induce dc conduction inside the thin films.

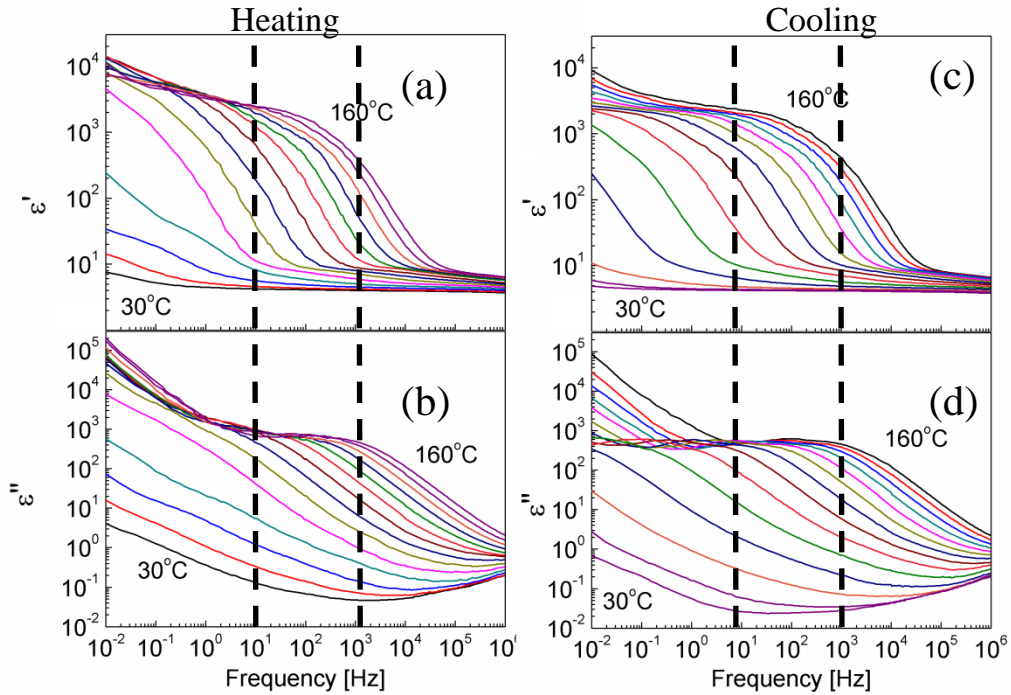


Figure 5.2: Dielectric constant ϵ' and dielectric loss ϵ'' spectra of Malto-C12C8 at heating-mode (a) & (b) and cooling-mode (c) & (d) from 30 °C – 160 °C with 10 °C temperature step.

Figure 5.3 illustrates the dielectric constant ϵ' and dielectric loss ϵ'' spectra for Malto-C14C10 at heating process (a) & (b) and cooling process (c) & (d) from 30 °C to 190 °C with 10 °C step temperature respectively. Both heating and cooling processes exhibit almost similar spectra pattern. The real component ϵ' shows three step increases when frequency is decreased. The first increase of ϵ' is at the high-frequency region (10^4 Hz – 10^6 Hz) which is due to the dielectric relaxation. The second large increase of ϵ' is at the intermediate-frequency region (10 Hz – 10^3 Hz) which can be related to the formation of heterogeneous structure where the charges were trapped at the domains. The third huge increase of ϵ' at the low-frequency region (below 10 Hz) is due to the charges accumulation near the electrode. In addition, the imaginary component ϵ'' shows a linear increase with a gradient of -1 at the low-frequency region which again configure the occurrence of the electrode polarization which will induce the dc conduction in the thin films.

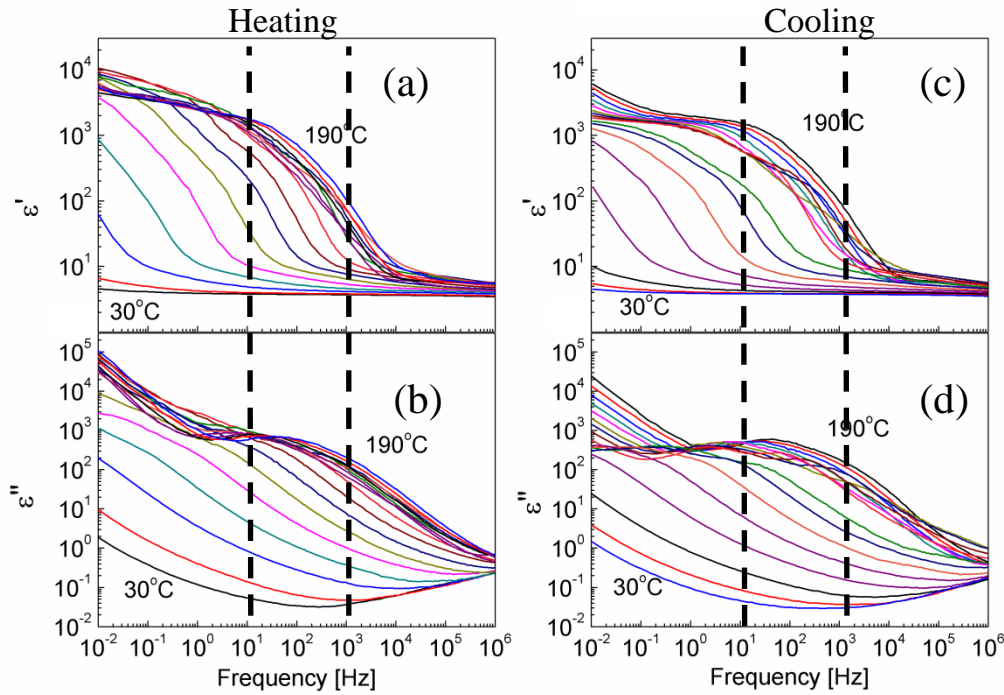


Figure 5.3: Dielectric constant ϵ' and dielectric loss ϵ'' spectra of Malto-C14C10 at heating-mode (a) & (b) and cooling mode (c) & (d) from 30 °C – 190 °C with 10 °C temperature step.

5.1.2 Dielectric constant at 100 Hz

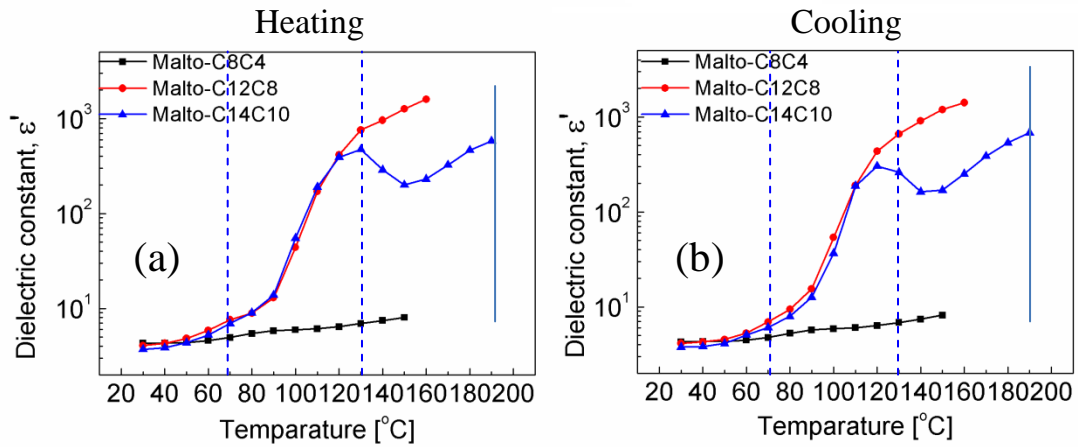


Figure 5.4: Temperature dependent of dielectric constant ϵ' of Malto-C8C4, Malto-C12C8 and Malto-C14C10 in heating-mode (a) and cooling-mode (b) at 100 Hz

Figure 5.4 shows the temperature dependent of ϵ' at 100 Hz for the three glycolipid compounds (Malto-C8C4, Malto-C12C8 and Malto-C14C10). Dielectric constant ϵ' at 100 Hz is selected to analyze the phase transitions due to the formation of heterogeneous structures which occurs at the intermediate-frequency region (10 Hz – 10^3 Hz). Both heating and cooling modes of temperature dependent of dielectric spectra exhibit approximately similar patterns. For Malto-C8C4, the values ϵ' is significantly lower compared to the other glycolipid compounds. The Malto-C8C4 has the shortest branched alkyl chain and only exhibits a single phase which is smectic A (SmA) phase until it becomes isotropic at 190 °C. The temperature dependent dielectric properties in smectic A phase for Malto-C8C4 were significantly different from Malto-C12C8 and Malto-C14C10 which have longer alkyl chains. For Malto-C8C4, we observed a much lower value of ϵ' increasing gradually with temperature until 160 °C which is the upper limit of the device temperature. It is due to Malto-C8C4 thin film accumulated when temperature beyond than 160 °C. Thus, the MIM structure device is destroyed. Within this temperature range, Malto-C8C4 is

in the smectic A phase. In contrast, both Malto-C12C8 and Malto-C14C10 exhibit more temperature dependent dielectric behaviors indicate the presence of several different phases (smectic A, cubic and columnar). For both Malto-C12C8 and Malto-C14C10, ϵ' increases gradually following the same behavior as that of Malto-C8C4, indicating these are in the same smectic phase (smectic A). At about 70 °C, the ϵ' for Malto-C12C8 and Malto-C14C10 increase rapidly with the increasing temperature. It exhibit a change in the organization of the self-assembly of molecules into a bicontinuous cubic phase (Q). For Malto-C14C10 at ~130 °C, the decrease in ϵ' represents another phase change known as the columnar phase (Col). While, the phase transition temperatures for Malto-C14C10 is almost similar to that which is observed by OPM, whereas the transition temperature into the cubic phase for Malto-C12C8 is slightly different from that reported by literature (R. Hashim et. al., 2006). The discrepancy may be due to the different measuring techniques which require different environments, e.g. various cells of different sizes and geometry. Furthermore, the existence of the cubic phase at a much lower temperature (compared to the OPM measurement) may also be affected by the applied electric field. In addition, literature reports on the phase transition temperatures involving cubic phases quite often vary significantly (same material and purity) due to the fact that the cubic phases are kinetically controlled. For Malto-C12C8, two references give different cubic phase transition temperatures, i.e. 119 °C (R. Hashim et. al., 2006) and 142 °C (G. Liao et. al., 2006).

5.1.3 Complex dielectric fitting with an empirical function

The dielectric spectra of three compounds (Malto-C8C4, Malto-C12C8 and Malto-C14C10) were analyzed quantitatively by fitting them to an empirical function (T.

Furukawa et. al., 2004) as shown in Equation 5.1.

$$\begin{aligned} \varepsilon^* = \varepsilon_{\infty} + \frac{\Delta\varepsilon}{(1+(i\omega\tau)^{\beta})^{\alpha}} \\ + \frac{\Delta\sigma_{dc}}{i\omega\varepsilon_0} \left(1 - \frac{1}{1+(i\omega\tau_{if})^{\gamma_{if}}}\right) + \frac{\sigma_{dc}}{i\omega\varepsilon_0} \left(1 - \frac{1}{1+(i\omega\tau_{el})^{\gamma_{el}}}\right) \end{aligned} \text{Equation 5.1}$$

The first and second terms represent the Havriliak-Negami (HN) function (S. Havriliak et. al., 1966; Furukawa et al., 1997), where ε_{∞} is the instantaneous permittivity, $\Delta\varepsilon$ is the dielectric relaxation strength and τ is the relaxation time. The α and β parameters describes the distribution of the relaxation times. The third and fourth term represent the conductive relaxation which are related to interfacial (*if*) and electrode polarization (*el*), where $\Delta\sigma_{dc}$ and σ_{dc} are conductive strength and dc conductivity respectively. The τ_{if} and τ_{el} are the relaxation times, and γ_{if} and γ_{el} are the exponents related to the distribution of relaxation times. The interfacial polarization is referred to the formation of heterogeneous structures in Malto-C12C8 and Malto-C14C10. For fitting dielectric spectra of Malto-C8C4, the third term in Equation 5.1 is ignored. It is because Malto-C8C4 does not form heterogeneous structures. Figure 5.5 shows an exemplary curve fitting of the dielectric spectra acquired for Malto-C12C8 at 100 °C by using Equation 5.1. The observed spectra (open mark) fitted well with Equation 5.1 (solid lines). With careful analysis in the dielectric loss ε'' spectra, where by gradually decreasing the value of $\Delta\sigma_{dc}$ (third term) and σ_{dc} (fourth term) in Equation 5.1, the corresponding loss peak can be observed by removing the contribution of dc conductivity and electrode polarization (represented by dashed line in Figure 5.5).

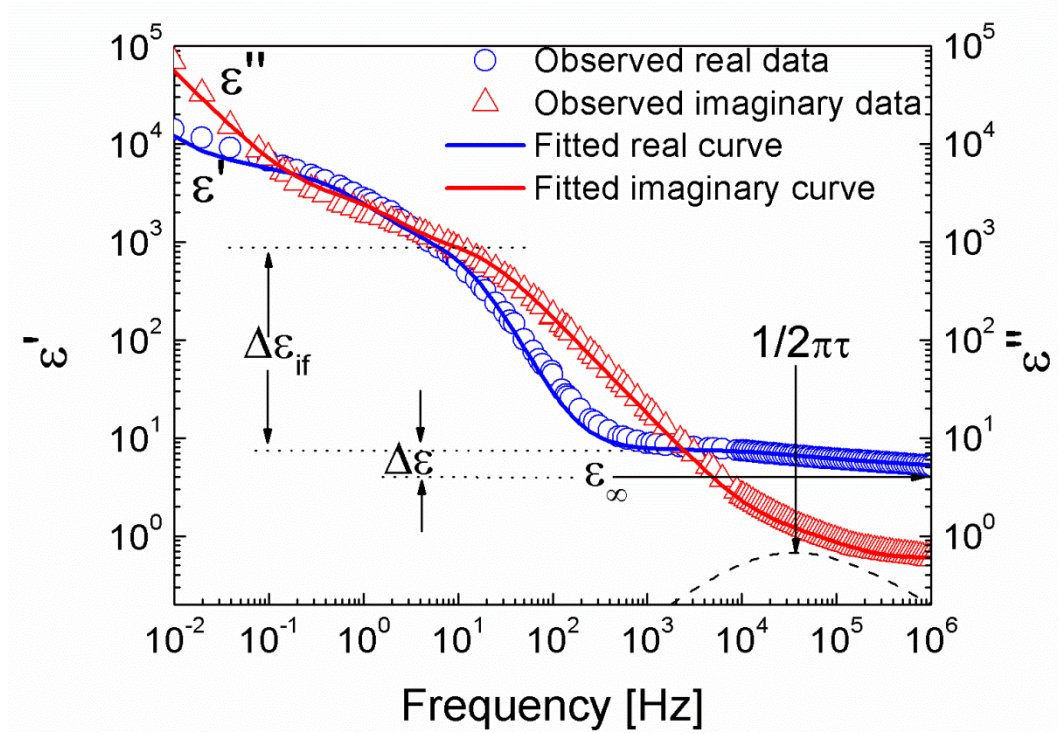


Figure 5.5: Observed and fitted of dielectric constant ϵ' and dielectric loss ϵ'' spectra of Malto-C12C8 at 100 °C during heating process.

5.2 Conductivity

5.2.1 Complex conductivity

Figure 5.6 shows the real component σ' and imaginary component σ'' of conductive spectra for Malto-C8C4 at heating process (a) & (b) and cooling process (c) & (d) from 30 °C to 150 °C with 10 °C temperature step respectively. Both heating and cooling processes exhibit similarly spectra pattern. The flat region of σ' spread within the frequency range (below 10 Hz) is known as dc conduction. The imaginary conductivity σ'' spectra exhibit a relaxation peak at low-frequency region (below 10 Hz). This relaxation peak corresponds to the electrode polarization (capacitance between electrodes). It is due to the accumulation of charges near the electrodes. When temperature increases, the spectra shifts to the high frequency side as well as

vertically due to the increase in dc conductivity. In high-frequency side, both σ' and σ'' increases when frequency increases corresponding to the dielectric contribution of molecules.

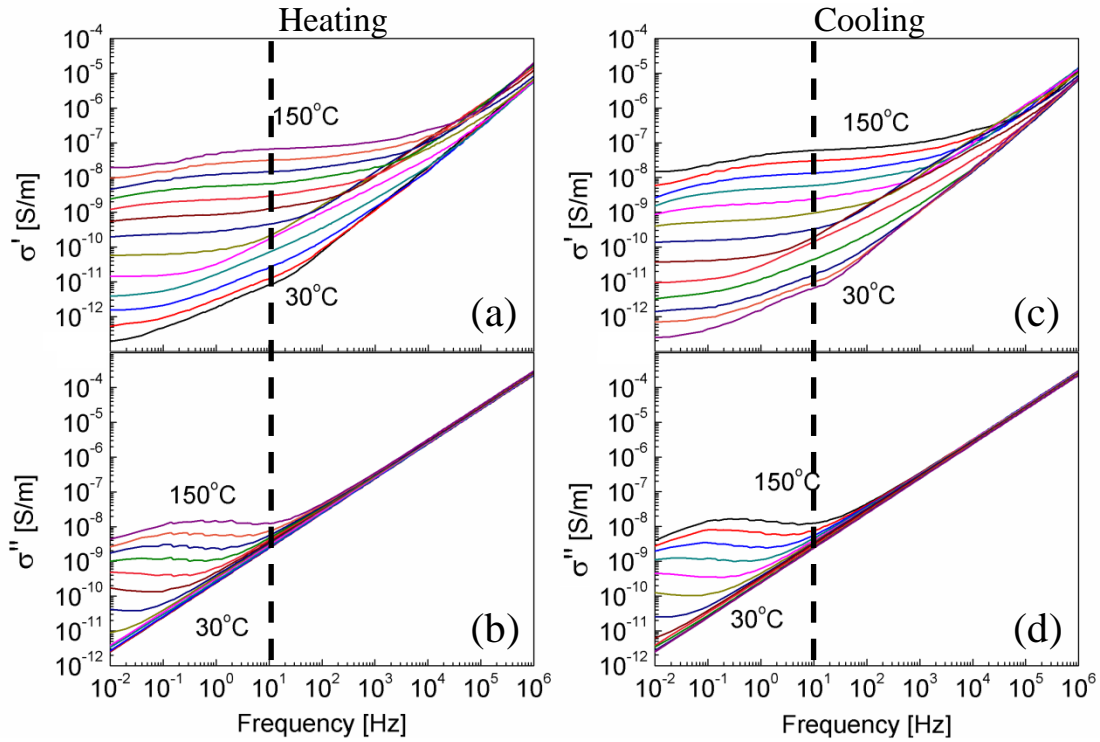


Figure 5.6: Real conductivity σ' and imaginary conductivity σ'' spectra of Malto-C8C4 at heating-mode (a) & (b) and cooling-mode (c) & (d) from 30 °C – 150 °C with 10 °C temperature step.

Figure 5.7 exhibits the real σ' and imaginary σ'' components of the conductive spectra for Malto-C12C8 during heating process (a) & (b) and cooling process (c) & (d) from 30 °C to 160 °C with a 10 °C temperature step respectively. Both heating and cooling processes show similar spectra pattern. From the plot of σ' , we observed a relatively flat region occurring within the frequency range (10 Hz – 10⁴ Hz), which usually represents a dc conduction. On the other hand, the imaginary conductivity, σ'' spectra exhibits two relaxation peaks at an intermediate- and a low-frequency regions. The relaxation peak at the frequency region of 10 Hz – 10⁴ Hz is presumably the interfacial polarization due to the formation of heterogeneous structures during phase

transition between smectic and bicontinuous cubic phases. The relaxation was attributed to the local fluctuation of charges confined temporarily in a certain domain. Subsequently, the structural reorganization at the phase transformation allows the charges to escape from previous confinement and provides diffusional characteristic. Another relaxation peak at low-frequency region (below 10 Hz) is corresponding to the electrode polarization which is due to the accumulation of charges near to the electrodes. At the higher frequency, both σ' and σ'' increased with frequency due to the dielectric relaxation of the molecules. Furthermore, as the temperature increases, the conductive spectra shift horizontally to the higher frequency as well as vertically because of the increase in the dc conductivity.

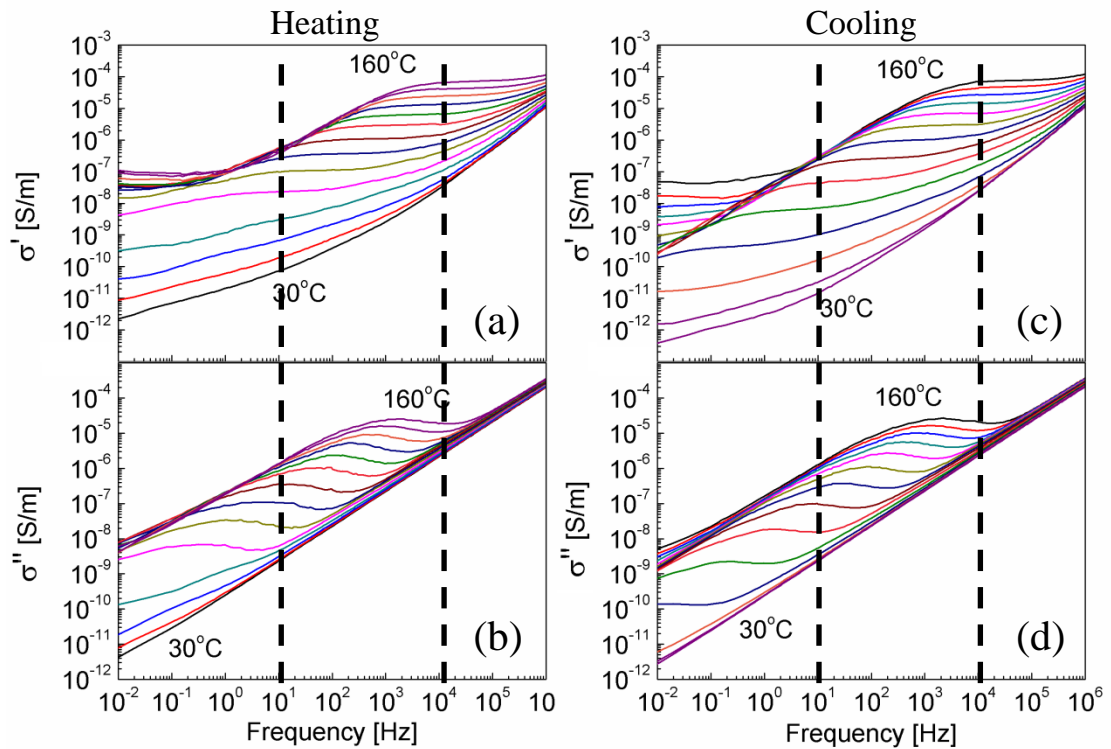


Figure 5.7: Real conductivity σ' and imaginary conductivity σ'' spectra of Malto-C12C8 at heating-mode (a) & (b) and cooling-mode (c) & (d) from 30 °C – 160 °C with 10 °C temperature step.

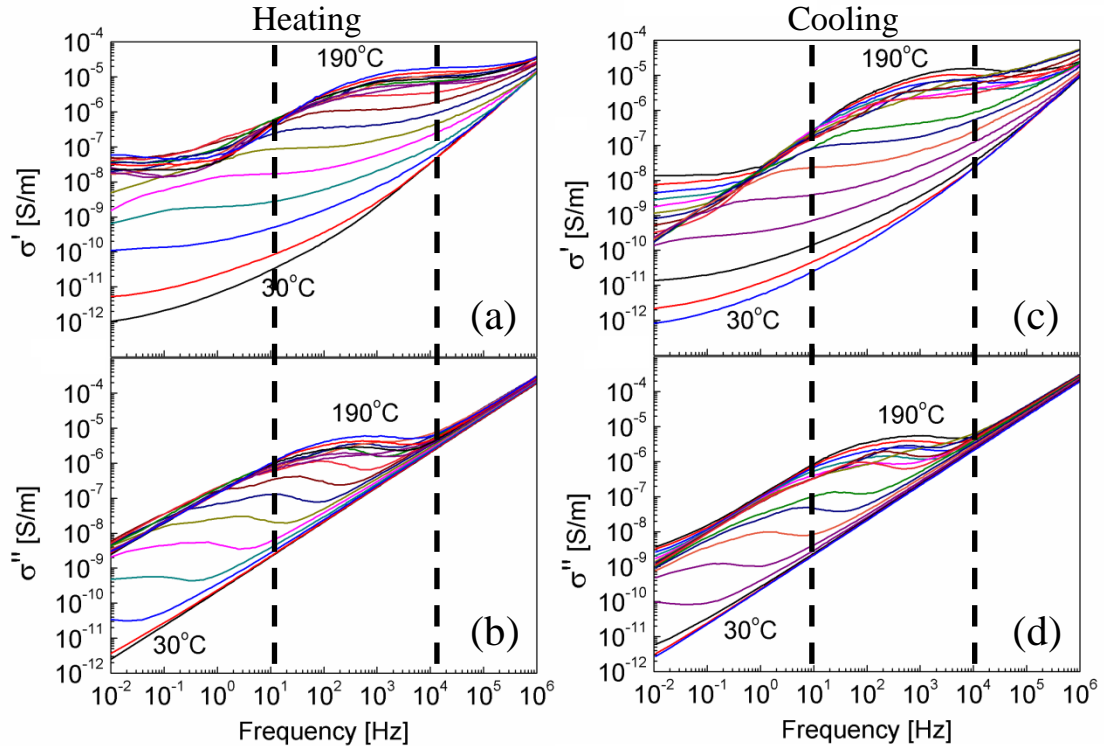


Figure 5.8: Real conductivity σ' and imaginary conductivity σ'' spectra of Malto-C14C10 at heating-mode (a) & (b) and cooling-mode (c) & (d) from 30 °C – 190 °C with 10 °C temperature step.

Figure 5.8 shows the real conductivity σ' and imaginary conductivity σ'' spectra for Malto-C14C10 at heating process (a) & (b) and cooling process (a) & (b) from 30 °C to 190 °C with 10 °C temperature step respectively. Both heating and cooling processes show approximately similar spectra pattern. The flat region of σ' spread at the intermediate-frequency range (10 Hz – 10⁴ Hz) is known as dc conduction. The imaginary conductivity σ'' spectra exhibits two relaxation peaks at intermediate-frequency and low-frequency region. The relaxation peak at intermediate-frequency region (10 Hz – 10⁴ Hz) is corresponding to the interfacial polarization. It is due to formation of heterogeneous structure (cubic phase and columnar phase) and movements of charges are restricted at certain domain when temperature increases. Another relaxation peak at low-frequency region (below 10 Hz) is corresponding to the electrode polarization (capacitance between electrodes). It is due to the

accumulation of charges near to the electrodes. When temperature increases, the spectra shift to high frequency side as well as vertically due to the increase in dc conductivity. In high-frequency side, both σ' and σ'' increase when frequency increase. It is corresponding to the dielectric contribution of molecules.

5.2.2 Complex conductivity fitting with an empirical function

The conductive spectra of three compounds (Malto-C8C4, Malto-C12C8 and Malto-C14C10) were analyzed quantitatively by fitting them to an empirical function (T. Furukawa et. al., 2004) which is shown in Equation 5.2.

$$\sigma^* = i\omega\varepsilon_o\varepsilon_\infty + \frac{i\omega\varepsilon_o\Delta\varepsilon}{(1+(i\omega\tau)^\beta)^\alpha} + \Delta\sigma_{dc} \left(1 - \frac{1}{1+(i\omega\tau_{if})^{\gamma_{if}}}\right) + \sigma_{dc} \left(1 - \frac{1}{1+(i\omega\tau_{el})^{\gamma_{el}}}\right) \quad \text{Equation 5.2}$$

The first and second terms are representing the Havriliak-Negami (HN) function (S. Havriliak et. al., 1966; Furukawa et al., 1997), where ε_∞ is the instantaneous permittivity, $\Delta\varepsilon$ is the dielectric relaxation strength and τ is the relaxation time. The α and β parameters describes the distribution of the relaxation times. The third and fourth terms are representing the conductive relaxation which are related to interfacial (*if*) and electrode polarization (*el*), where $\Delta\sigma_{dc}$ and σ_{dc} are conductive strength and dc conductivity, respectively. The τ_{if} and τ_{el} are the relaxation times, and γ_{if} and γ_{el} are the exponents related to the distribution of the relaxation times. The interfacial polarization in Equation 5.2 is referring to the formation of heterogeneous structures in Malto-C12C8 and Malto-C14C10. But, Malto-C8C4 does not form heterogeneous structure. Thus, the third term in Equation 5.2 is ignored when fitting the dielectric spectra of Malto-C8C4. Figure 5.9 shows the exemplary curve fitting of the

conductive spectra acquired for Malto-C12C8 at 100 °C by using Equation 5.2. The observed spectra (open mark) fitted well with Equation 5.2 (solid lines). In the imaginary component σ'' spectra, two obvious conductive relaxations were fitted by a symmetrical loss peak at $1/2\pi\tau_{el}$ and $1/2\pi\tau_{if}$ which are known as interfacial and electrode polarization respectively (represented by dashed line in Figure 5.9).

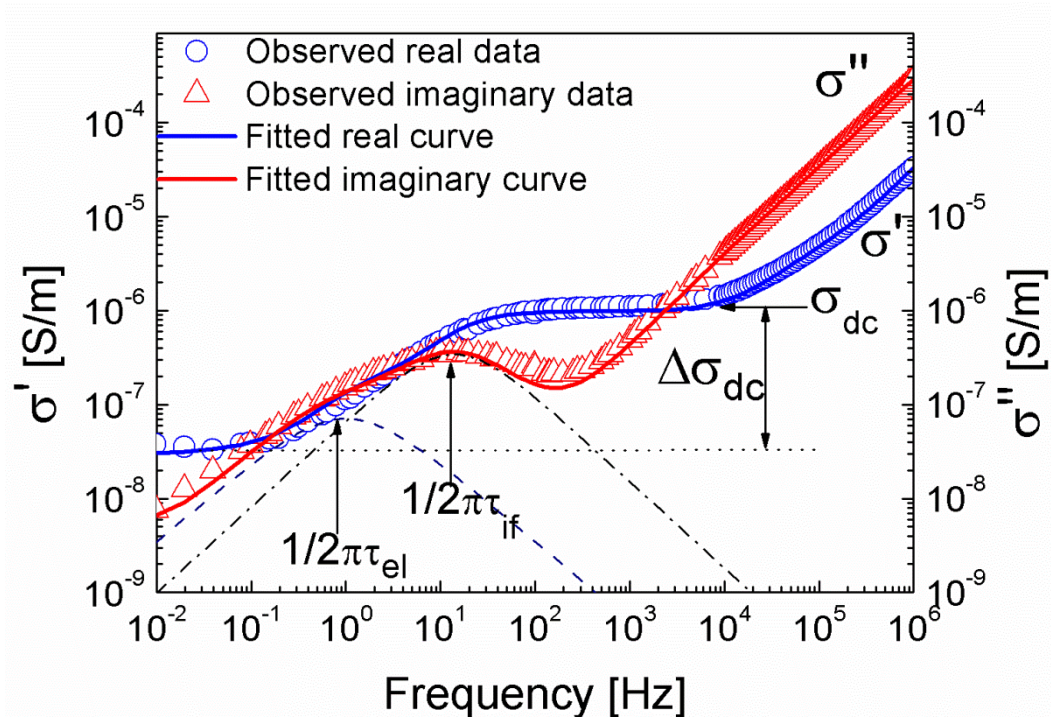


Figure 5.9: Observed and fitted of real conductivity σ' and imaginary conductivity σ'' spectra of Malto-C12C8 at 100 °C during heating process.

5.2.3 Activation energy

The relaxation frequency was extracted from fitting the experimental results by using Equation 5.2. The temperature dependent relaxation times for the compounds are shown in Figure 5.10 which follows the Arrhenius behaviour. The activation energies were obtained from the Arrhenius expression which is $\tau_{if} \propto \exp\left(\frac{E_a}{RT}\right)$ where E_a is

the activation energy, R is the molar constant and T is the absolute temperature. During heating process, it was observed that the smectic phase exhibits the highest activation energy compared to the other phases, especially for Malto-C8C4 which was exhibits 252 kJ/mol in activation energy.

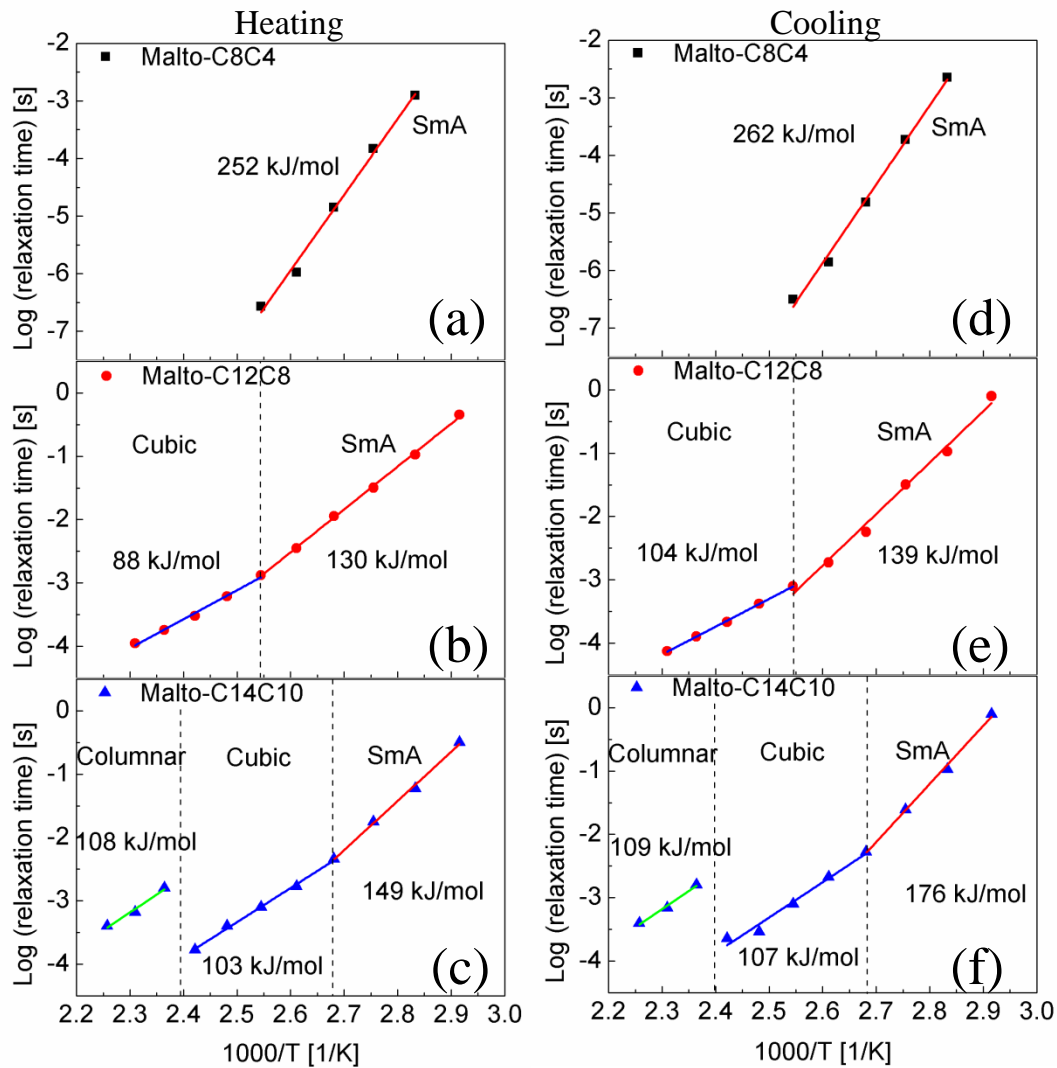


Figure 5.10: The Arrhenius plot shows the corresponding activation energy of Malto-C8C4, Malto-C12C8 and Malto-C14C10 in heating- (a, b & c) and cooling-mode (d, e & f).

From literature, it was found that the smectic phase is more ordered than the columnar phase in sugar lipids (G. Liao et. al., 2006). In addition, when transition occurs from the isotropic \rightarrow columnar \rightarrow smectic phase, the activation energy will increase (G.

Liao et. al., 2006). Therefore, the smectic A phase for Malto-C8C4 which has the shortest chain is more ordered compared to the other two compounds. In the cubic phase for the longer branched alkyl-chain glycolipids, the activation energy is reduced indicating a reduced overall ordering in the hydrophobic region (R. Hashim et. al., 2012). The activation energy E_a of the cubic phase is the smallest although cubic phase is a highly ordered phase and mechanically stiff, but the overall order is zero as it is show optically isotropic texture under OPM. Therefore, the relationship of relaxation behaviour to microscopic ordering and molecular interaction is not so clear especially for the cubic phase. In the cooling process, similar Arrhenius behaviour was exhibited when compared to heating process. Subsequently, overall E_a of the cooling process was slightly higher than the heating process. It is due to the inclusion of some annealing effect, which increases the hardness of the thin films.

5.3 Pyroelectric effect

In this section, the pyroelectric properties and figure-of-merit of the glycolipids (Malto-C8C4, Malto-C12C8 and Malto-C14C10) are discussed. The pyroelectric properties of the three compounds were measured at several temperature ranges (25-26 °C, 30-31 °C, 40-41 °C and 50-51 °C). Pyroelectric current waveforms were observed, when a triangular waveform temperature was applied to the glycolipid thin film as shown in Figure 5.11. When the triangular waveform temperature was varied between 25 °C and 26 °C, the pyroelectric current exhibits square waveform as shown in Figure 5.11 (a). This is known as real pyroelectric current which is induced by the change of electric dipole moment. Subsequently, the same square waveform of pyroelectric current was observed in temperature range of 30-31 °C and 40-41 °C. When the temperature was varied between 50 °C and 51 °C, the pyroelectric current

exhibits a triangular waveform as shown in Figure 5.11 (b). It is a false pyroelectric current and is known as conductive current. This conductive current is induced by water molecules (impurities) which come from moisture during preparation of the devices which has been trapped between molecules of the sample. Furthermore, these water molecules contribute significantly and the contribution is greater than that which comes from the change in electric dipole moment. Thus, it shows the conducting behaviour and with the pyroelectric behaviour as shown by the non-square waveform of the current.

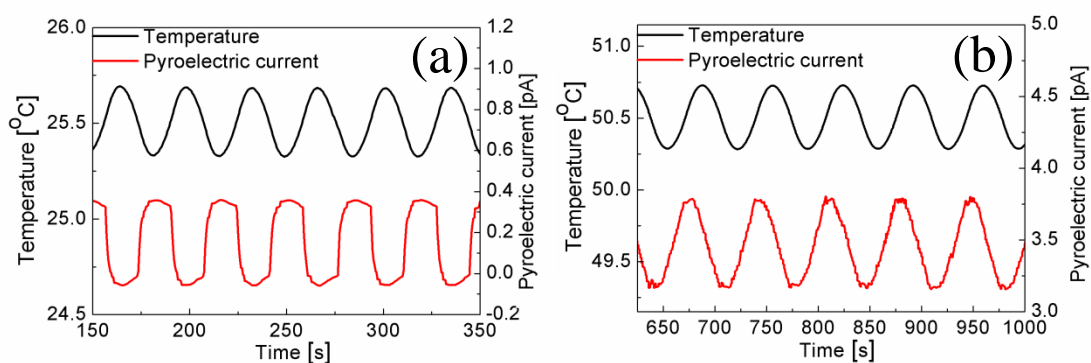


Figure 5.11: Pyroelectric current waveform at the rate of $0.03\text{ }^{\circ}\text{C s}^{-1}$ with respect to temperature variation of (a) 25-26 $^{\circ}\text{C}$ and (b) 50-51 $^{\circ}\text{C}$ for Malto-C12C8.

Figure 5.12 (a) shows that the pyroelectric coefficient, p of the Malto-C8C4, Malto-C12C8 and Malto-C14C10 at several temperature ranges. The pyroelectric coefficient of glycolipid compounds is about 1 to 3 $\mu\text{C m}^{-2} \text{K}^{-1}$ since they have the same number of sugar head group (refer to Table 5.1). Subsequently, among the glycolipid compounds, the pyroelectric coefficient of Malto-C8C4 is the lowest. It is due to the molecular arrangement in Malto-C8C4 being more ordered, which induce the decreasing of the net electric dipole moment (will be discussed later in this section). Whereas in Figure 5.12 (b), exhibits the calculated figure-of-merit (FOM) of the three glycolipid compounds at each temperature variation via Equation 5.3 is shown,

$$FOM = \frac{P}{\sqrt{\varepsilon' \tan \delta}} = \frac{P}{\sqrt{\varepsilon''}} \quad \text{Equation 5.3}$$

The pyroelectric FOM reflects the voltage responsivity of a pyroelectric material and its high value is desirable for the detection of pyroelectricity. Among these glycolipid compounds, Malto-C8C4 show the highest FOM due to its low dielectric loss compared to Malto-C12C8 and Malto-C14C10 even though its pyroelectric coefficient is the lowest (refer to Tables 5.2 and 5.3). It is due to the lower dissipation of power release from Malto-C8C4 when an alternating electric field is applied (will be discussed later in this section).

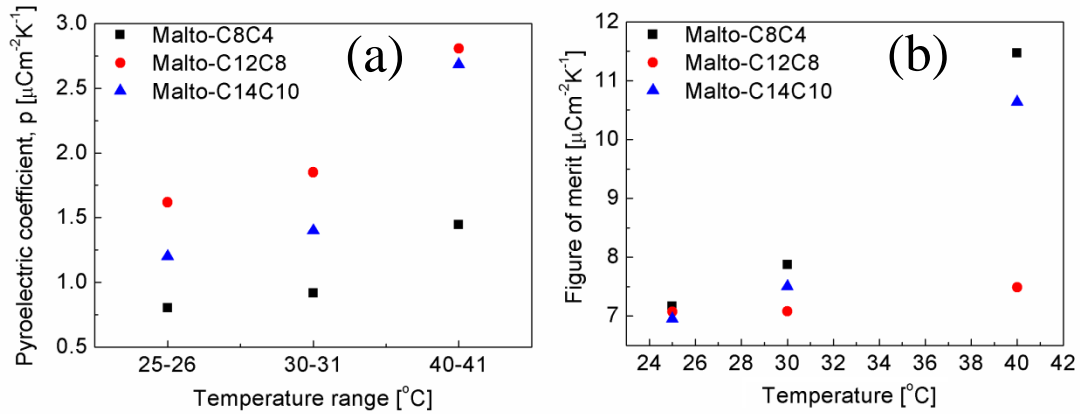


Figure 5.12: (a) Pyroelectric coefficient and (b) figure-of-merit of three glycolipid compounds at various temperatures.

Table 5.1: Summary of the pyroelectric coefficient, p (with unit $\mu\text{C m}^{-2} \text{K}^{-1}$) for the glycolipid compounds.

Temperature ($^{\circ}\text{C}$)	Malto-C8C4	Malto-C12C8	Malto-C14C10
25	0.80 \pm 0.01	1.62 \pm 0.01	1.20 \pm 0.02
30	0.91 \pm 0.02	1.85 \pm 0.01	1.40 \pm 0.01
40	1.45 \pm 0.01	2.81 \pm 0.02	2.70 \pm 0.01

Table 5.2: Summary of the figure-of-merit (with unit $\mu\text{C m}^{-2} \text{K}^{-1}$) for the glycolipid compounds.

Temperature ($^{\circ}\text{C}$)	Malto-C8C4	Malto-C12C8	Malto-C14C10
25	7.17 ± 0.03	7.07 ± 0.02	6.95 ± 0.03
30	7.87 ± 0.05	7.08 ± 0.05	7.50 ± 0.03
40	11.47 ± 0.04	7.49 ± 0.03	10.63 ± 0.05

Table 5.3: Summary of the dielectric loss, ε'' at 100 Hz for the glycolipid compounds.

Temperature ($^{\circ}\text{C}$)	Malto-C8C4	Malto-C12C8	Malto-C14C10
25	0.013 ± 0.001	0.052 ± 0.001	0.030 ± 0.001
30	0.014 ± 0.002	0.068 ± 0.002	0.035 ± 0.001
40	0.016 ± 0.001	0.140 ± 0.001	0.064 ± 0.002

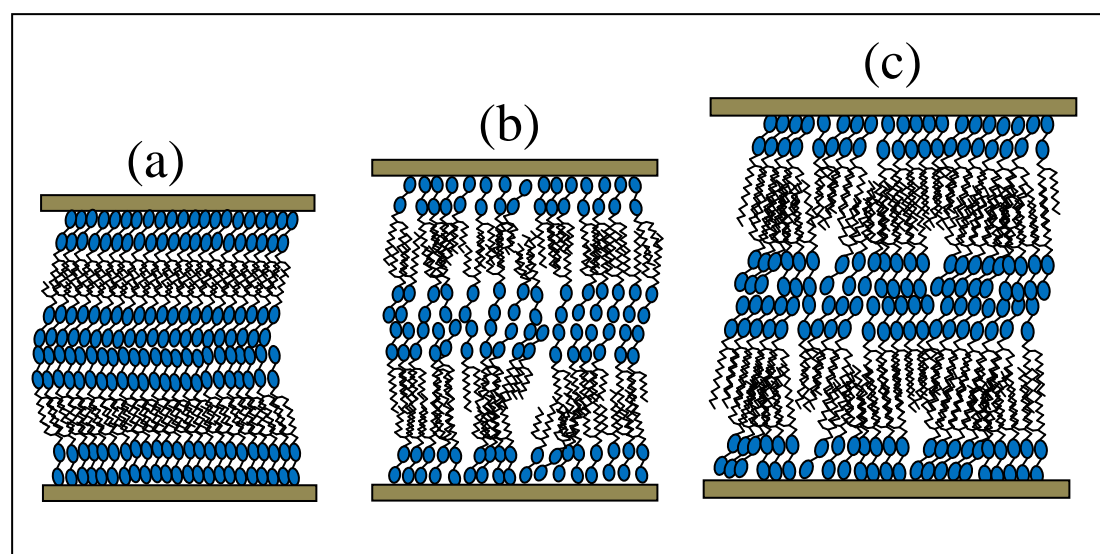


Figure 5.13: Proposed molecular arrangements of (a) Malto-C8C4, (b) Malto-C12C8, and (c) Malto-C14C10 in the formation of thin film between top and bottom electrodes.

When the solution of glycolipid is spin casted onto the glass substrate, the sugar heads (hydroxyl groups) of the glycolipid presumably tend to attach on the surface of the glass substrate and develop hydrogen bonds between adjacent sugar heads. Thus, the sugar heads form a hydrogen bonded network within the same layer, thus limiting the

headgroup motion. It is suggested that the apolar flexible of the alkyl chains form a homeotropic alignment as shown in Figure 5.13 as a result of repulsion from the polar headgroup region.

Figure 5.13 shows the proposed molecular arrangements of Malto-C8C4, Malto-C12C8 and Malto-C14C10 in the formation of thin film between the top and bottom electrodes. The molecules of Malto-C8C4 have the shortest branched alkyl chain. Therefore, the arrangement of the molecules will be more ordered and compacted as shown in Figure 5.13 (a). Subsequently, the ordered arrangement causes the net dipole moment of the thin films to decrease due to cancellation of the dipole moment among the layers of molecules. Thus, the pyroelectric coefficient of Malto-C8C4 is the lowest. In addition, the movement of molecules is limited when an alternating electric field is applied. Thus, less power is dissipated since less friction is produced by the molecular motion. As a result, the dielectric loss ϵ'' of Malto-C8C4 is the lowest. The lowest dielectric loss ϵ'' gives the highest value of FOM in Malto-C8C4. In Figure 5.13 (b), the molecular arrangement of Malto-C12C8 is comparatively partial disordered among these glycolipid compounds. This partial disorder arrangement of molecules increases the net dipole moment in the thin films due to less cancellation of the dipole moment among the layer of molecules. Therefore, the pyroelectric coefficient of Malto-C12C8 is the highest. Meanwhile, the apolar branched alkyl chain of Malto-C12C8 is more flexible, i.e. it has a higher degree of freedom to move randomly since the glycolipid molecules has less rotational freedom due to the hydrogen bonding network of the headgroup. When an alternating electric field is applied, the friction between molecules increases since the collisions between molecules occur more frequently. Therefore, more power is dissipated and the dielectric loss ϵ'' of Malto-C12C8 is the highest. As a result, the FOM of Malto-

C12C8 is the lowest. In Figure 5.13 (c), the molecular arrangement of Malto-C14C10 is comparatively moderate in order among these three glycolipid compounds. Thus, the value of pyroelectric coefficient of Malto-C14C10 is in the middle of the other two glycolipid compounds. In addition, the apolar branched alkyl chain of Malto-C14C10 is the longest and it will induce interdigitated effect. Some of the branched alkyl chains have been ensnared which restrict the movement of the molecules. The power dissipated is moderate since less collision or friction occurs between the molecules when compared to Malto-C12C8. As a result, the dielectric loss ϵ'' and FOM of Malto-C14C10 is in the moderate range.

5.4 Diffusion process

5.4.1 Conductive strength, relaxation frequency and dielectric strength

Generally, bicontinuous cubic phase Q is found to be in between smectic and columnar phase in the phase diagram. In addition, it can also be induced by mixing these two phases (von Minden et. al., 2002). It is quite rare to observe this phase in thermotropic systems from amphiphilic materials and much less has been studied about them. Thus, in this work, more focus has been given on this phase for Malto-C12C8 and Malto-C14C10 where cubic phase is prominently observed in the temperature range of 120-160 °C and 100-130 °C, respectively. Among the quantities determined as the best-fit parameters from Equation 5.2 are the conductive strength $\Delta\sigma_{dc}$, relaxation frequency f_m , and the dielectric strength $\Delta\epsilon$ in interfacial- and dielectric-mode (Figure 5.14). For Malto-C12C8 in heating and cooling processes, as the temperature increases, its conductive strength $\Delta\sigma_{dc}$ (Figure 5.14 a & d) and relaxation frequency f_m (Figure 5.14 b & e) in both modes (interfacial and dielectric)

increase. In the dielectric-mode, the conductivity strengths $\Delta\sigma_{dc}$ exhibit greater values than those in the interfacial-mode. This is because the diffusion process of charge carriers is the fastest in the dielectric mode which occurs at higher relaxation frequency, f_m . Thus, the greater conductivity strength in the dielectric mode is explained. Similarly, the same trends was observed for Malto-C14C10 in heating and cooling processes.

Figure 5.14 (c) & (f) show the plots of dielectric strength versus temperature for Malto-C12C8 and Malto-C14C10 in the cubic phase (heating and cooling process). These plots are rather flat and almost unvarying with temperature unlike those for the conductive strength $\Delta\sigma_{dc}$ and the relaxation frequency f_m . The seemingly unchanging behaviour can be explained by analyzing the complex functions, $\Delta\varepsilon_{if}^* = \Delta\varepsilon_{if}(i\omega)^{\gamma-1}$ given by Furukawa et al. and Johnson et al. (T. Furukawa et. al., 1997; J. F. Johnson et. al., 1951):

$$\frac{1}{2\pi f_m} = \tau_{if} = \left(\frac{\Delta\varepsilon_{if}}{\Delta\sigma_{dc}} \right)^{\frac{1}{\gamma_{if}}} \quad \text{Equation 5.4}$$

Several points can be noted. Firstly, both the conductive strength $\Delta\sigma_{dc}$ and the interfacial relaxation time (τ_{if}) which is inversed to the relaxation frequency (f_m) were found roughly to the same extent (see Figure 5.14 a & b, d & e). Secondly, if the exponent fitting parameter $\gamma_{if} = 1$, then the dielectric strength related to the interfacial polarization $\Delta\varepsilon_{if}$ calculated for the domains in the cubic phase for Malto-C12C8 and Malto-C14C10 can be proven from Equation 5.4 to be independent of temperature as found from the plot of Figure 5.14 (c) and (f). The calculated fitted parameter of γ_{if} (in heating and cooling process) were found to be about 0.85-0.95.

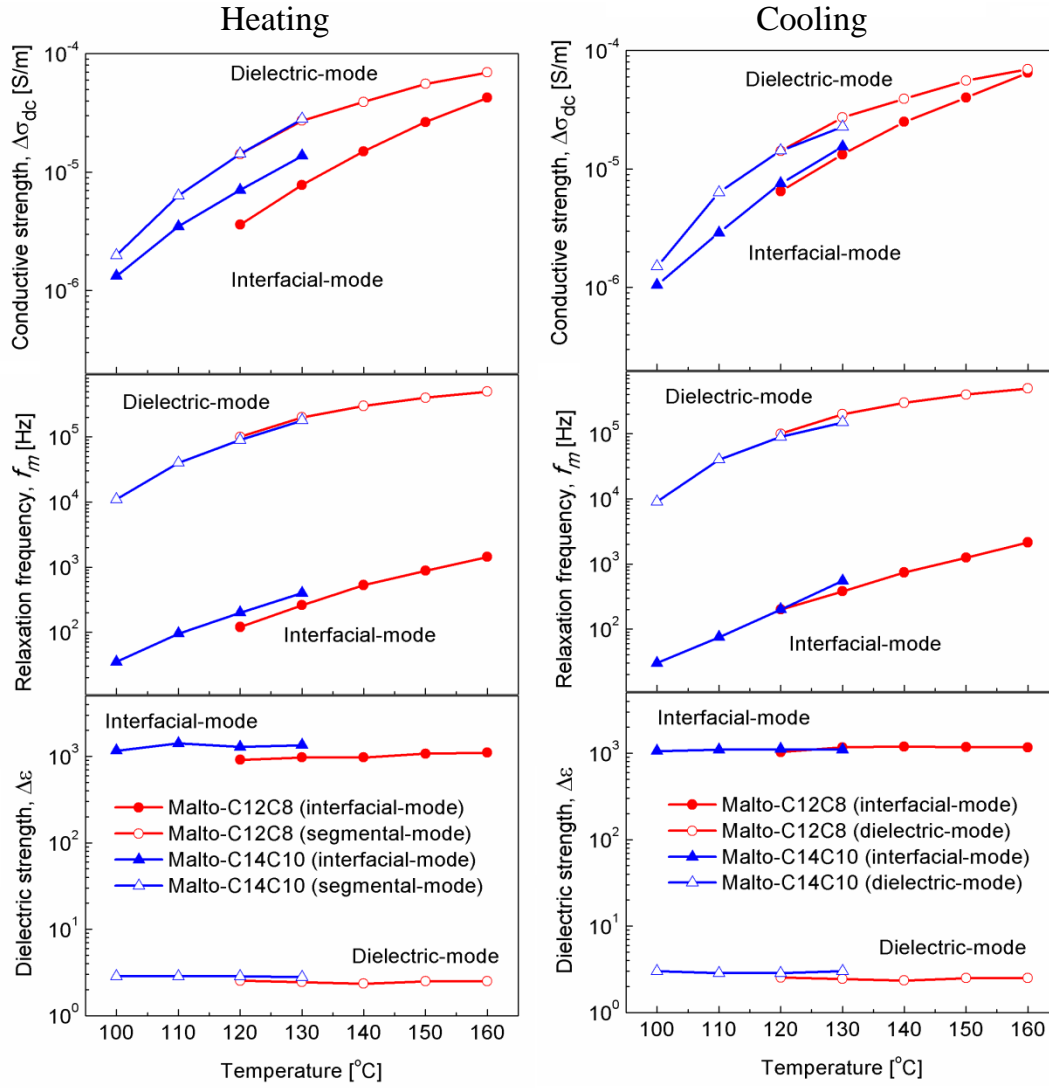


Figure 5.14: The cubic phase properties (conductive strength $\Delta\sigma_{dc}$, relaxation frequency f_m , and dielectric strength $\Delta\epsilon$) of Malto-C12C8 and Malto-C14C10 in interfacial-mode and dielectric-mode during heating (a, b, & c) and cooling process (d, e, & f).

Moreover, the value of dielectric strength, $\Delta\epsilon_{if}$ in the interfacial mode (heating and cooling processes) for Malto-C12C8 and Malto-C14C10 is very large ($\Delta\epsilon_{if}$ approximately 1000) and independent of temperature (refer to Figure 5.14 c & f). Similarly, in the dielectric-mode (heating and cooling processes), the $\Delta\epsilon$ value of Malto-C12C8 and Malto-C14C10 exhibits independence to temperature and their values are about 3.

5.4.2 Diffusion coefficient

In the cubic phase of the glycolipids (in heating and cooling process), during interfacial relaxation, the charge carriers trapped in the domains manage to hop from one domain to another whereas in the dielectric mode the molecular motion occurs within the domains. Domains as mentioned here are referred to the plane of micro phase separation bent in both directions forming bicontinuous network. The interior of the domain is filled by the polar head-group of the lipid with tunnels filled with apolar chains and the polar region is draped. In this phase, the charge carriers tend to trap at domains and hop around harmoniously with the Brownian motion in the polar sugar-head group. The sugar head has a mutual interaction with the charge carriers to regulate a smoother motion and with a sufficient time, the charges hop between the domains. The microscopic features of charge hopping can be modeled by a random walk scheme with a step length, λ and step time, τ_o respectively. The Einstein-Smoluchowski equation relates these quantities with the diffusion coefficient, D as shown in the Equation 5.5 below, where λ and τ_o are hopping length and time respectively in a microscopic features of charge hopping.

$$D = \frac{\lambda^2}{6\tau_o} \quad \text{Equation 5.5}$$

For a system containing N (assuming that $N = cN_A$, where c is the molarity of the glycolipids and N_A is Avogadro's number) molecules with charge q , the diffusion coefficient D relates to conductivity strength $\Delta\sigma_{dc}$ and can be calculated by Equation 5.6.

$$\Delta\sigma_{dc} = \frac{Nq^2}{k_B T} D \quad \text{Equation 5.6}$$

where k_B is the Boltzmann constant and T is the absolute temperature. The trapped charge carriers within the domain and hopping mechanism from one domain to another contribute to the dc conductivity and diffusion coefficient. The diffusion coefficients, D are calculated from Equation 5.6 and plotted in Figure 5.15 (a & b) as double logarithmic plot versus relaxation frequency, f_m for the interfacial-mode and dielectric-mode respectively (in the heating and cooling process). It can be noted that the diffusion process exhibit linear relationship with the slopes, approximate to 1 in both interfacial and dielectric mode (in the heating and cooling process). Since the dielectric strengths ($\Delta\epsilon_{if}$ and $\Delta\epsilon$) of both compounds were almost constant when the temperature was increased (as shown in Figure 5.14 c & f), the charges were hopping at approximately constant distances between domains in the cubic structure and between the sugar head groups.

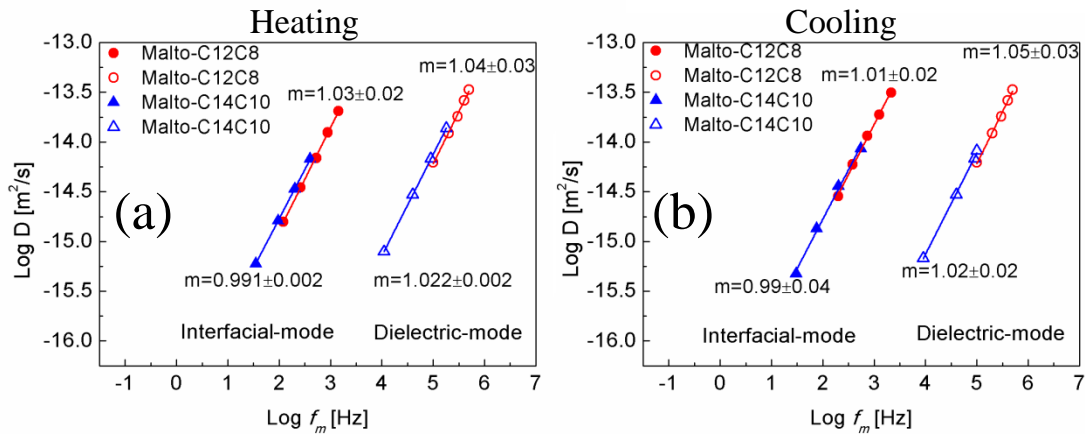


Figure 5.15: The double logarithmic plot of diffusion coefficients D of Malto-C12C8 and Malto-C14C10 as a function of relaxation frequency in interfacial-mode and dielectric-mode during heating (a) and cooling process (b).

The aforementioned conduction mechanism is demonstrated in the cubic phase of the glycolipid in a schematic diagram in Figure 5.16. A few assumptions were made to obtain the hopping length of the glycolipids in cubic phase. First, it is assumed that τ_{if}

and τ is proportional to the relaxation time in the interfacial polarization, $\frac{1}{2\pi f_{m(if)}}$ and dielectric polarization, $\frac{1}{2\pi f_m}$ respectively. Secondly, it is assumed that the hopping distance λ_{if} and λ are independent of temperature and the charge hopping occurs at relaxation frequency, which is $f_{m(if)}$ for interfacial relaxation frequency and f_m for the dielectric relaxation frequency. In the interfacial-mode of cubic phase, the charges have sufficient time to hop between the domains since the relaxation frequency occurs at lower frequency. Using Equations 5.5 and 5.6, the hopping lengths λ_{if} of charge carriers between domains were calculated and the values tabulated in Table 5.4.

Table 5.4: Hopping lengths of the interfacial polarization calculated from the theoretical model (dielectric measurement) for Malto-C12C8 and Malto-C14C10 in the heating and cooling process.

Glycolipid Compounds	hopping length λ_{if} (nm) in heating process	hopping length λ_{if} (nm) in cooling process
Malto-C12C8	3.61 ± 0.01	3.78 ± 0.01
Malto-C14C10	4.02 ± 0.01	4.01 ± 0.01

In dielectric-mode, the charges are trapped in domains and only hop between the sugar head of molecules. Thus, the hopping length λ between the sugar head groups for Malto-C12C8 and Malto-C14C10 in heating and cooling process were calculated via the Equations 5.5 and 5.6 and the values are shown in Table 5.5. These hopping lengths λ are approximately equivalent to the hydrogen bond distance which is ~ 2 to 3.5 \AA (G. A. Jeffrey et. al., 1977; G. R. Desiraju, 1991). It is understood that the hydrogen bond distance determines the strength of the hydrogen bond where the shortest hydrogen bond has the highest hydrogen bond strength. The calculated values

of hydrogen bond distance indicate that the domains in the cubic phase are bonded by hydrogen bonding and the charges tend to hop between the OH-group in the sugar head of the glycolipids. This is demonstrated in the schematic diagram in Figure 5.16.

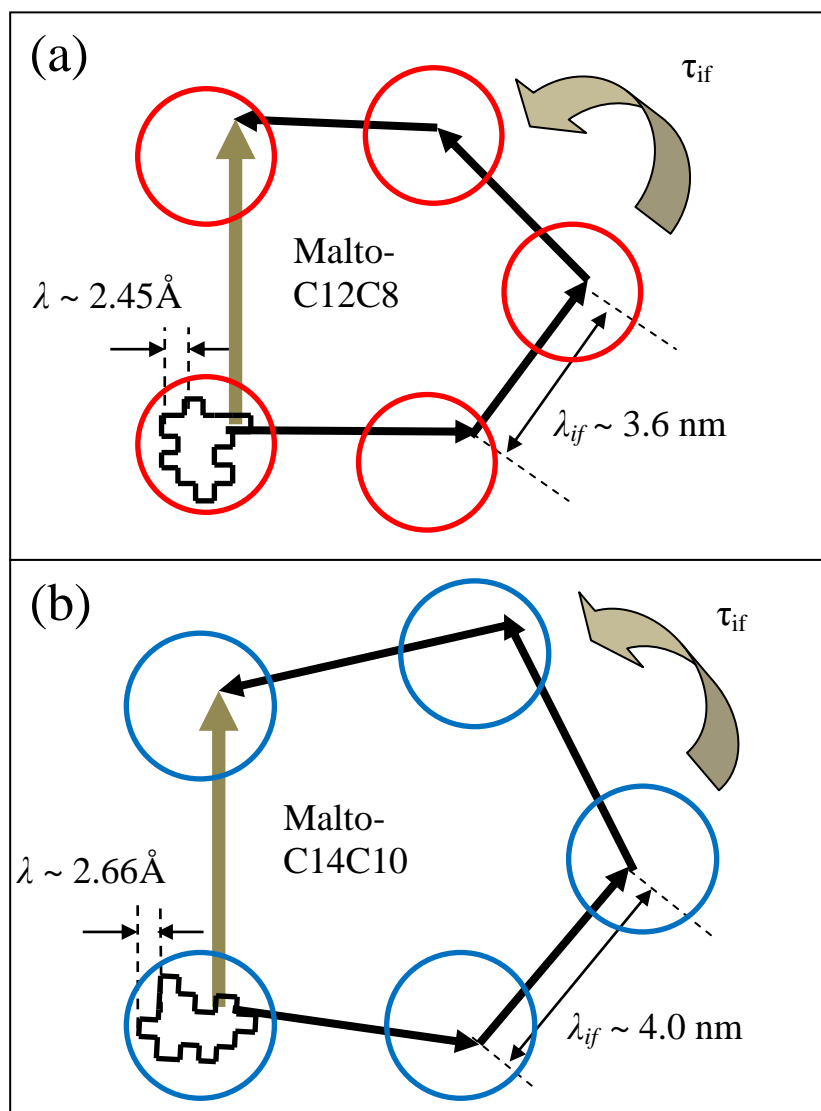


Figure 5.16: Schematic diagram of charge hopping process with their hopping length for glycolipids in (a) Malto-C12C8 and (b) Malto-C14C10 for both interfacial and dielectric modes in heating process (circle represent domain which contain disaccharide polar head group only).

Table 5.5: Hopping lengths of the dielectric polarization calculated from the theoretical model (dielectric measurement) for Malto-C12C8 and Malto-C14C10 in the heating and cooling process.

Glycolipid Compounds	hopping length λ (Å) in heating process	hopping length λ (Å) in cooling process
Malto-C12C8	2.45 ± 0.05	2.48 ± 0.05
Malto-C14C10	2.66 ± 0.03	2.70 ± 0.05

5.5 Summary

In the complex dielectric, the Malto-C8C4 did not exhibit interfacial polarization since it does not form any heterogeneous structure. The complex dielectric spectra of Malto-C12C8 and Malto-C14C10 show huge dielectric constants (~ 1000) which occur due to the formation of heterogeneous structures (e.g. cubic and columnar phase). This heterogeneous structure can be obviously observed when the results are presented in complex conductivity. The interfacial polarization in complex conductivity can be used to determine the formation of cubic phase. The phase transitions of glycolipid compounds can be observed with the dielectric constant (at 100 Hz) and activation energy. Furthermore, the pyroelectric coefficient of Malto-C8C4 is the lowest due to the ordered arrangement of the molecules. It also gives the lowest dielectric loss, as a result the FOM of Malto-C8C4 is the highest. Thus, it has high potential for the applications in infra-red sensors. In addition, using the diffusion process (random walk scheme model) in the cubic phase of Malto-C12C8 and Malto-C14C10, the hydrogen bond length (2.45~2.70 Å) and the bilayer molecular thickness (3.61~4.02 nm) were calculated and determined.

References

- Jeffrey, G. A., Takagi, S. (1977). Hydrogen-Bond Structure in Carbohydrate Crystals. *Accounts of Chemical Research*, **11**, 264-270.
- Liao, G., Zewe, S. K., Hagerty, J., Hashim, R., Abeygunaratne, S., Vill, V., Jákli, A. (2006). Thermotropic liquid crystalline properties of amphiphilic branched chain glycolipids. *Liquid Crystals*, **33**, 361-366.
- Desiraju, G. R. (1991). The C-H \cdots O Hydrogen Bond in Crystals: What Is It?. *Accounts of Chemical Research*, **24**, 290-296.
- von Minden, H. M., Milkereit, G., Vill, V. (2002). Effects of carbohydrate headgroups on the stability of induced cubic phases in binary mixtures of glycolipids. *Chemistry and Physics Lipids*, **120**, 45-56.
- Johnson, J. F., Cole, R. H. (1951). Dielectric Polarization of Liquid and Solid Formic Acid1. *Journal of the American Chemical Society*, **73**, 4536-4540.
- Hashim, R., Sugimura, A., Minamikawa, H., Heidelberg, T. (2012). Nature-like synthetic alkyl branched-chain glycolipids: a review on chemical structure and self-assembly properties. *Liquid Crystals*, **39**, 1-17.
- Hashim, R., Hashim, H. H. A., Rodzi, N. Z. M., Hussen, R. S. D., Heidelberg, T. (2006). Branched chain glycosides: Enhanced diversity for phase behavior of easily accessible synthetic glycolipids. *Thin Solid Films*, **509**, 27-35.
- Havriliak S., Negami, S. (1966). A complex plane analysis of α -dispersions in some polymer systems, *Journal of Polymer Science Part C: Polymer Symposia*, **14**, 99-103.
- Furukawa, T., Yasuda, K., Takahashi, Y. (2004). Dielectric and Conductive Spectra of the Composite of Barium Titanate and LiClO₄ -Doped Polyethylene Oxide, *IEEE Transaction on Dielectric and Electrical Insulation*, **11**, 65-70.
- Furukawa, T., Imura, M., Yuruzume, H. (1997). Broad-Band Conductive Spectra of Polypropylene Oxide Complexed with LiClO₄. *Japanese Journal of Applied Physics*, **36**, 1119-1125.

CHAPTER 6: CONCLUSIONS AND SUGGESTIONS FOR FUTURE WORKS

6.0 Conclusions

The research work presented in this thesis focused on the effect of the branched alkyl chain length of the maltoside glycolipids to the pyroelectric and their potential applications. This research work mainly studied the structural and electrical properties of the maltoside glycolipids. Subsequently, a theoretical model has also been applied to the system to determine the bilayer molecular length of molecules from the hopping mechanism.

6.0.1 Structural properties of maltoside glycolipids

The phase transition temperature showed that the longer the branched alkyl chain length of maltoside glycolipids, the more liquid crystal phases were present, i.e. cubic and columnar phase. It was due to the effect of interdigitating which occurred between apolar parts of two glycolipid molecules. When temperature increases, the molecules will self-assemble to form several liquid crystal phases. The phases are also confirmed from the existence of the endothermic peak in DSC measurement except for the cubic phase of Malto-C12C8 and Malto-C14C10. From the DSC measurements, the formations of cubic phase from smectic A phase cannot be detected probably due to a very small change in the enthalpy change. From the TGA measurements, the maltoside glycolipids are stable upon heating up to temperature of about 275 – 300 °C. It can be observed that the longer the branched alkyl chain length, the higher the thermal stability of the glycolipids. Subsequently, the presence of hydroxyl (O-H) groups in the maltoside glycolipids are confirmed by the FTIR

analysis where the transmittance are observed was at around $3400 - 3200 \text{ cm}^{-1}$. The existence of O-H group in the molecule of glycolipids is important as it is used to induce the dipole moment. The XRD spectra exhibit peaks in Malto-C8C4 only. The XRD analysis of Malto-C8C4 thin films indicates that the molecules were self-assembled in three ordered structures. Some of the molecules are declined at a certain angle with respect to the normal direction due to the less support obtained from the shortest branched alkyl chain length.

6.0.2 Electrical properties of maltoside glycolipids

The challenge of this work is humidity effect which will induce the lyotropic properties of the glycolipid compounds. It has been solved by enriching the inert gas in the sealed chamber during the experiment. In the complex dielectric, Malto-C8C4 shows the dielectric constant to be less than 10 at 100 Hz. It is because the Malto-C8C4 only exists in smectic A phase without the formation of heterogeneous structures (i.e. cubic or columnar). The finding is also confirmed from the complex conductivity analysis which does not show the occurrence of interfacial polarization. However, Malto-C12C8 and Malto-C14C10 show the formation of heterogeneous structures (i.e. cubic and columnar). It was observed from the complex dielectric analysis, which a huge dielectric constant (~ 1000) was obtained from the two glycolipids (Malto-C12C8 and Malto-C14C10). Furthermore, a prominent peak can be observed in the imaginary conductivity which can be related to the interfacial polarization and also the formation of heterogeneous structures. It reveals that the longer the branched alkyl chain length of glycolipids, the higher the number of phases that existed (e.g. cubic or columnar). The Arrhenius behaviour analyzed to calculate the activation energy of Malto-C12C8 and Malto-C14C10 is shown to be lower

compared to that of Malto-C8C4. Thus, Malto-C12C8 and Malto-C14C10 can exist in more than one liquid crystalline phases when the temperature changes. In addition, among the maltoside glycolipids investigated, Malto-C8C4 has the higher potential for application in infra-red sensor. It is due to its lowest dielectric loss, even though the pyroelectric coefficient exhibited by Malto-C8C4 is the lowest. The figure-of-merit of Malto-C8C4 is the highest. The diffusion process in the cubic phase of Malto-C12C8 and Malto-C14C10 is also modeled by using random walk scheme. From the random walk scheme, the diffusion process of charge carriers has been utilized to probe the hopping distance and also to identify the hydrogen bond length and the bilayer molecular thickness. The hydrogen bond lengths of Malto-C12C8 and Malto-C14C10 were found to be within 2.45~2.70 Å. The bilayer molecular thickness of Malto-C12C8 and Malto-C14C10 meanwhile was calculated to be ~3.61nm and ~4.02 nm respectively.

6.1 Future works

The research work presented in this thesis can be considered as the groundwork of the structural and electrical properties of maltoside glycolipids. There are many more works that is needed to be carried out to accomplish and improve the research results. Some of the suggestions are considered and discussed in the section below:

1. Small angle x-ray scattering (SAXs) experiment needs to be carried out instead of XRD measurement to identify the structural arrangement of Malto-C12C8 and Malto-C14C10.

2. A chamber which can control the humidity of the experiment environment and carry out a low resistivity electrical measurement (dielectric and conductivity) such that a study on lyotropic properties of the glycolipid compounds can be performed effectively, is required in this work.
3. The bias voltage can be applied several times to remove the charge carriers which have been trapped in the polar sugar head domain (e.g. cubic). It can be observed the dielectric constant rapidly decreased from ~1000 to about 20 – 40 after the application of the bias voltage. The residue dielectric constant may be due to the cooperative motion of molecules which is an interesting research work. This cooperative motion could contribute to the spontaneous polarization which can be used to enhance the pyroelectric properties of glycolipids.
4. Malto-C6C2 and Malto-C10C6 can be studied to accomplish the structural and electrical properties of the maltoside glycolipids. Thus, a complete study of the maltoside group's glycolipids can be fully achieved.
5. The nuclear magnetic resonance (NMR) can be use to study dielectric relaxation of materials. It describe the motion of nuclei under magnetic field. There are two major relaxation processes in NMR, i.e. spin – lattice (longitudinal) and spin – spin (transverse) relaxations.